BRNO UNIVERSITY OF TECHNOLOGY
VYSOKÉ UČENÍ TECHNICKÉ V BRNĚ

FACULTY OF MECHANICAL ENGINEERING
FAKULTA STROJNÍHO INŽENÝRSTVÍ

INSTITUTE OF MATERIALS SCIENCE AND ENGINEERING
ÚSTAV MATERIÁLOVÝCH VĚD A INŽENÝRSTVÍ

STUDY OF INTER-ATOMIC INTERACTIONS IN ADVANCED MATERIALS WITH HELP OF AB INITIO CALCULATIONS

STUDIUM MEZIATOMOVÝCH INTERAKCÍ V POKROČILÝCH MATERIÁLECH S POMOCÍ AB INITIO VÝPOČTŮ

MASTER'S THESIS
DIPLOMOVÁ PRÁCE

AUTHOR — **Bc. Jozef Janovec**
AUTOR PRÁCE

SUPERVISOR — **Ing. Martin Zelený, Ph.D.**
VEDOUCÍ PRÁCE

BRNO 2021

BRNO UNIVERSITY OF TECHNOLOGY
FACULTY OF MECHANICAL ENGINEERING

Assignment Master's Thesis

Institut:	Institute of Materials Science and Engineering
Student:	**Bc. Jozef Janovec**
Degree programm:	Applied Sciences in Engineering
Branch:	Materials Engineering
Supervisor:	**Ing. Martin Zelený, Ph.D.**
Academic year:	2020/21

As provided for by the Act No. 111/98 Coll. on higher education institutions and the BUT Study and Examination Regulations, the director of the Institute hereby assigns the following topic of Master's Thesis:

Study of inter–atomic interactions in advanced materials with help of ab initio calculations

Brief Description:

Macroscopic properties of solids as their stability or mechanical properties are determined by type of chemical interaction between atoms. These interactions can be studied theoretically with help of quantum–mechanical calculations. In particular, the curves of Density of States (DOS) and Crystal Orbital Hamilton Population (COHP) are useful for evaluation and comparison of interatomic interactions because they are able to describe bonding, non–bonding and anti–boding contributions to chemical bonds. Understanding of these interactions is especially important for compounds which exhibit combination of covalent and metallic bonds. For example, diborides of transition metals or shape memory alloys belong to this class of materials.

Master's Thesis goals:

The goal of this work is to calculate the DOS and COHP curves with help of ab initio method and analyze them. The population analysis of charge distribution is also a part of this work. The analysis will results in revealing of such chemical interactions, which are responsible for instability of particular materials or can have essential influence on its mechanical properties. The analysis will be made for diborides TmB2 (Tm = Ti, V, Nb, Mo, Ta, W, Re) and magnetic shape memory alloy Ni2MnGa.

Recommended bibliography:

KITTEL, C. Úvod do fyziky pevných látek, Academia, Praha, 1985.

MARTIN, R. P. Electronic Structure: Basic theory and practical methods, Cambridge University Press, Cambridge, 2004.

DRONSKOWSKI, R. Computational Chemistry of Solid State Materials, WILEY-VCH Verlag GmbH & Co. KGaA, Weinheim, 2005.

Deadline for submission Master's Thesis is given by the Schedule of the Academic year 2020/21

In Brno,

L. S.

prof. Ing. Ivo Dlouhý, CSc. Director of the Institute	doc. Ing. Jaroslav Katolický, Ph.D. FME dean

Abstract

Chemical bonding in transition metal diborides and Ni_2MnGa alloy was studied in terms of energy resolved COHP visualization tool. The electronic structure of studied systems was calculated using the first principles calculations with the help of projector augmented-wave method. Concerning transition metal diborides, we found dependence of the strongest boron-boron bond on the charge transfer from metal to boron atoms. The stability of diborides with the α structure decreases with higher number of metal valence electrons due to on-site contribution to the band energy near the Fermi level.

Ni_2MnGa shape memory alloy was treated by DFT+ U corrective method in order to describe localized electrons more accurately. The effect of U on Ni resides in destabilization of the cubic austenite and stabilization of the tetragonal NM martensite. On the contrary, U on Mn destabilizes martensite. The bond analysis shows that the strongest bond in the alloy is Ni-Ga with covalnet character. Increased localization of Mn valence electrons makes Mn-Ni bond more covalent and Ni-Ni bond more metallic. The localization of Ni electrons results in more metallic Mn-Ni bond.

Abstrakt

Pomocou COHP analýzy sme študovali chemickú väzbu v diboridoch prechodných kovov ako aj v zliatine Ni_2MnGa. Elektrónová štruktúra študovaných materiálov bola vypočítaná použitím výpočtov z prvých princípov pomocou metódy PAW. V prípade diboridov tranzitných kovov z výsledkov vyplýva, že sila väzby bór-bór je silne závislá od transferu elektrónov na atómy bóru. Zvyšujúci sa počet valenčných elektrónov v kove spôsobuje destabilizáciu α štruktúry kvôli vzájomnej interakcii elektrónov prislúchajúcich jednému atómu (on-site interakcie) v blízkosti Fermiho hladiny.

Pre zliatinu s tvarovou pamäťou Ni_2MnGa bola použitá metóda DFT+ U upravujúca popis lokalizácie elektrónov. V prípade použitia parametra U na Ni dochádza k destabilizácii kubického austenitu a k stabilizácii tetragonálneho nemodulovaného martenzitu. Naopak, zvýšenie lokalizácie elektrónov mangánu martenzit destabilizuje. Analýza väzieb ukázala, že najsilnejšou väzbou je Ni-Ga s kovalentným charakterom. Zvýšená lokalizácia valenčných elektrónov Mn zvyšuje podiel kovalentnosti Mn-Ni väzby a kovový charakter Ni-Ni väzby. Vplyvom zvýšenej lokalizácie Ni elektrónov sa Mn-Ni väzba stáva viac kovovou.

Key words

Transition metal diborides, COHP, DFT+ U, bonding analysis, Ni_2MnGa

Kúčové slová

Diboridy prechodných kovov, COHP, DFT+ U, analýza chemických väzieb, Ni_2MnGa

Bibliographic citation

JANOVEC, Jozef. Study of inter-atomic interactions in advanced materials with help of ab initio calculations [online]. Brno, 2021. Master's thesis. Brno University of Technology, Faculty of Mechanical Engineering, Institute of Materials Science and Engineering. Supervised by Martin Zelený.
Available at: https://www.vutbr.cz/studenti/zav-prace/detail/132354.

JANOVEC, Jozef. Studium meziatomových interakcí v pokročilých materiálech s pomocí ab initio výpočtů [online]. Brno, 2021. Diplomová práce. Vysoké učení technické v Brně, Fakulta strojního inženýrství, Ústav materiálových věd a inženýrství. Vedoucí práce Martin Zelený.
Dostupné z: https://www.vutbr.cz/studenti/zav-prace/detail/132354.

Declaration

I declare that my master's thesis entitled "Study of inter-atomic interactions in advanced materials with help of ab initio calculations" has not been previously submitted in any university or institution for an award of a degree. All results reported in this thesis are my own except as cited in the bibliography and the work was in its entirety written by me.

In Brno, May 24, 2021 .....

Jozef Janovec

Acknowledgement

Thank you Dr. Zelený for your invaluable advises and guidance throughout my master's degree studies. I'm very thankful for your huge help with fulfilment of my academic goals home and abroad. I would also like to thank Dr. Helmut Riedl-Tragenreif, Dipl. Ing. Christoph Fuger, Dr. Rainer Hahn and Dr. David Holec from the Institute of Materials Science and Technology, TU Wien for helping me with protective coating related topics and for creating a friendly and productive environment during my lockdown stay in Vienna. Last but definitely not least, I would like to express my gratitude to Prof. Andrés Ayuela for great ideas and interesting discussions.

This thesis was elaborated thanks to the Aktion Österreich-Tschechien, AÖCZ-Semesterstipendien scholarship financed by the Austrian Federal Ministry of Education, Science and Research. I acknowledge Vienna Scientific Cluster, joint cluster Mark of CEITEC Brno and Institute of Materials Science and Technology, BUT as well as Donostia International Physics Center's Supercomputing Center for available computational time. This work was supported by the Czech Science Foundation [grant number 21-06613S].

I would also like to give a special thanks to my family for their unceasing support.

Contents

Introduction

Before the invention of quantum mechanics, prediction of material's properties was solely dependent on results of experiments. Nowadays electronic structure calculations are possible from the first principles that means without any need for empirical input. Besides many other applications, first principles calculations can be used for chemical bonding analysis. In this thesis we investigate inter-atomic interactions and chemical bonding in terms of Density of states (DOS), Crystal Orbital Hamiltonian Population (COHP) and Crystal Orbital Overlap Population (COOP). The later two functions separate DOS into pair interactions with distinguished bonding, non-bonding and antibonding interactions. Mentioned analytic tools are incorporated in the LOBSTER software package that was used here. The work aims to understand inter-atomic interactions in transition metal diborides as well as in Ni_2MnGa ferromagnetic Heusler alloy.

Transition metal diborides (TMD) are non-oxide ceramics that are used mainly for their high toughness as cutting tools or armor and shielding as well as refractory materials. Transition metal diborides serve as hard protective coating for highly loaded tools to increase performance, endurance and corrosion resistance. These materials compete in tools coating application with nitrides and carbides successfully reaching comparable or better hardness and fracture toughness. TMDs exhibit complex interatomic interactions with three types of chemical bonding - covalently bonded boron layers, ionic and covalent mixed transition metal (TM) - boron bonds and metallic bonding between metal atoms. Besides bonding analysis in relaxed structures we study shear deformation along the boron layer and resulting changes in bond strength of all group 4 to group 7 TMDs.

In the second part our goal is to study implementation of the corrective DFT+ U approach on Ni_2MnGa alloy exhibiting large magnetic field-induced strain (MFIS) and magnetic shape memory effect (MSM). The accuracy of DFT calculations is dependent on the level of approximation of the exchange-correlation electron interaction. Good precision is achieved by the local density approximation (LDA) or generalized gradient approximation (GGA), however these functionals tend to over-delocalize mainly d and f electrons. This drawback is within Hubbard corrective approach, denoted as DFT+ U method, surpassed by an additive term in the Hamiltonian acting only on mentioned orbitals. Here we investigate the effect of the corrective approach on stability of cubic austenite and non-modulated martensite. Furthermore we study the effect of electron localization on bonds in correlation with various implementation of U parameter.

The thesis is organized in the following manner - the first chapter briefly summarizes theory behind first principles calculations, in the second chapter we review transition metal diborides and Ni_2MnGa alloy. Results in the third chapter are summarized in two sections, first of which presents study of inter-atomic interactions within TMDs and in second we show DFT+ U study of Ni_2MnGa alloy.

1. Theoretical background

This chapter briefly describes the theory behind the *ab initio* approach used in the computational materials science that is essential for purposes of this thesis. Modern computational software packages allow up to predict material properties from the first principles i.e. without the necessity of any empirical input. Revealing of the knowledge of the electronic structure, particle interactions and energetics requires a solution of the Schrödinger equation that, unfortunately, has to be approximated. Probably the most important concept that makes demanding calculations possible even for extended systems is the Density Functional theory [1], famously introduced by Hohenberg and Kohn in 1964 that will be briefly discussed in section 1.3.

1.1. Quantum mechanical approach

One of the key changes quantum mechanics introduced, as opposed to the classical theory, is the wave character of elementary particles with the corresponding wave function that fully describes any state of a particle - in the case of computational solid-state physics of an electron. In general, the wave function is a complex function of position and time. Time evolution of a wave function is given by the fundamental Schrödinger equation [2], [3] that is a quantum mechanical analogy to the classical equation of motion. The time dependent one-particle Schrödinger equation has the form

$$i\hbar\frac{\partial\Psi(\boldsymbol{x},t)}{\partial t}=\left[-\frac{\hbar^2}{2m}\frac{\partial^2}{\partial x^2}+V(\boldsymbol{x},t)\right]\Psi(\boldsymbol{x},t)\equiv\hat{H}\Psi(\boldsymbol{x},t), \tag{1.1}$$

where i is the imaginary unit, $\hbar$ is the Planck's constant, $\Psi(\boldsymbol{x},t)$ is the wave function, m is mass of a particle and $V(\boldsymbol{x},t)$ stands for a potential felt by the particle. Two terms in the square brackets are the kinetic and potential energy which together form the Hamiltonian operator $\hat{H}$ (the hat symbol denotes an operator). In order to solve this partial differential equation we search for the solution of the wave function that is a product of one variable functions (function of spatial coordinate $\psi(\boldsymbol{x})$ and function of time $\psi(t)$). Separation of variables leads to the form

$$\hat{H}\psi(\boldsymbol{x})\psi(t)=E\psi(\boldsymbol{x})e^{-i\frac{E}{\hbar}t}. \tag{1.2}$$

where time dependence is comprised within the phase factor $e^{-i\frac{E}{\hbar}t}$. The time-dependent Schrödinger equation describes electron excitation events, interaction with light, quantum tunneling and more. The time-independent Schrödinger equation obtained after the separation of variables represents the most fundamental problem in computational materials science. By neglecting the time-dependence we simplify the problem to a static calculation of the ground state properties. The time-independent eigenvalue problem is formulated as

$$\hat{H}\psi(\boldsymbol{x}) = E\psi(\boldsymbol{x}), \tag{1.3}$$

where E is the total energy of a system and the Hamiltonian is the energy operator.

The Born probabilistic interpretation of the wave function implies that its square is proportional to the probability density of finding a particle in a specified space [3], [4]. Integration of the wave function over all space equals one, meaning that the particle indeed exists somewhere in the space. This property is called normality. Other properties of a wave function are that it has to be continuous, single-valued and finite. For fermions a wave function must satisfy the antisymmetry with respect to particle interchange, that is its sign changes upon the interchange of particle coordinates. Fermions are particles that are govern by the Fermi-Dirac statistics and they posses half-integer spin. Electrons, protons, neutrons or neutrinos are examples of fermions [5].

Systems studied by first principles are arrangements of billions of interacting electrons and nuclei. The Hamiltonian for such a many-body problem has to include numerous interactions. Its general form expressed in the Gaussian units is

$$\hat{H} = -\frac{\hbar^2}{2m_e}\sum_{i}^{N}\nabla_i^2 - \frac{\hbar^2}{2M_I}\sum_{I}^{L}\nabla_I^2 + \frac{e^2}{4\pi\varepsilon_0}\left[\sum_{i,I}^{N,L}\frac{Z_I}{|\boldsymbol{r_i}-\boldsymbol{R_I}|} + \frac{1}{2}\sum_{i\neq j}^{N}\frac{1}{|\boldsymbol{r_i}-\boldsymbol{r_j}|} + \frac{1}{2}\sum_{I\neq J}^{L}\frac{Z_I Z_J}{|\boldsymbol{R_I}-\boldsymbol{R_J}|}\right], \tag{1.4}$$

where electrons are denoted by the lower case subscript and nuclei by the upper case subscript. Here, m_e and M_I are the masses of an electron and of a nucleus, ∇^2 is the Laplace operator, e is the elementary charge, ε_0 is the dielectric constant of vacuum, Z is the atomic number, $\boldsymbol{r}$ and $\boldsymbol{R}$ are positions of electrons and nuclei, N and L denote number of electrons and nuclei in the system. Terms within the Hamiltonian are from left to right the kinetic energy of electrons and the kinetic energy of nuclei, electron-nucleus interaction, electron-electron interaction and nucleus-nucleus interaction [6]. The interparticle interactions, namely electron-electron ones, become impossible to be solved exactly already for relatively small systems, due to tremendous number of particles in consideration. Therefore, in order to perform quantum mechanical calculations of real systems, numerous approximations to the treatment of interactions have to be made.

If we consider that protons and neutrons are both more than 1800 times heavier than electrons [7], it is clear that the nuclear kinetic energy term in Equation 1.4 is neglectable compared to the electronic kinetic energy. Hence for electrons, nuclei are static and play the role of a constant external potential. This approach is known as the Born-Oppenheimer (B-O) or adiabatic approximation [6], [8]. Consequently we can spit the many-body wave function of a system into the nuclear and the antisymmetric electronic part where the latter depends on nuclear coordinates only parametrically. The Schrödinger equation can be then solved for electrons and nuclei separately, the first is a standard problem in calculation of electronic structure and the second is used for lattice dynamics and electron-phonon interaction calculations.

The Hamiltonian within the Born-Oppenheimer approximation is expressed similarly as in Equation 1.4 only that the nuclear kinetic energy term is neglected in B-O approximation. This practice can be abbreviated as

$$\hat{H} = \hat{T}_e + \hat{V}_{ext} + \hat{V}_{int} + E_{II}, \tag{1.5}$$

here $\hat{T}_e$ is the kinetic energy operator for the electrons, $\hat{V}_{ext}$ is the operator for electron-nucleus interactions (interactions with an external field due to nuclei), $\hat{V}_{int}$ accounts for the electron-electron interaction (internal interactions) and E_{II} is the interaction between nuclei that is an additive term. The Hamiltonian depends only on nuclear coordinates, that produce an external field for electrons, atomic numbers of nuclei and on the number of electrons. Different compounds are defined by Hamiltonian in Equation 1.5 where only these three parameters change.

In quantum mechanics, any observable (any measurable physical quantity) can be evaluated as an expectation value of a corresponding operator. The operator for energy is the Hamiltonian and its expectation value can be expressed, in Dirac bra-ket notation, as

$$\langle \hat{H} \rangle = \frac{\langle \psi | \hat{H} | \psi \rangle}{\langle \psi | \psi \rangle} = \frac{\int \psi^* \hat{H} \psi d\boldsymbol{r}}{\int \psi^* \psi d\boldsymbol{r}} = E \geq E_0, \tag{1.6}$$

where $\langle \psi |$ and $| \psi \rangle$ are called bra and ket, the asterisk denotes a complex conjugate and the integration goes over all space and coordinates. The purpose of *ab initio* calculations is in the first place to find the ground state with a corresponding ground state wave function and energy. The search of a proper wave function is governed by the variational principle, which says that the ground state is characterised by the lowest possible energy, as expressed in Equation 1.6, where E_0 is the ground state energy [6], [9].

Calculations of electronic structure of extended structures in materials science, that is pretty much all the solid-state systems, are practically impossible to perform even after the B-O approximation. Solution to this problem for periodic structures is given by the Bloch's theorem [10], [11] that takes advantage of the translational symmetry of a lattice. The potential that electrons feel in a periodic crystal is translationally invariant with the period od the crystal and the Hamiltonian therefore doesn't change for coordinates separated by a lattice vector. We can also deduce that the crystal wave function is periodic accordingly to the crystal

$$\psi(\boldsymbol{r} + \boldsymbol{T}) = e^{i\boldsymbol{k}\boldsymbol{T}} \psi(\boldsymbol{r}), \tag{1.7}$$

$$\psi(\boldsymbol{r}) = e^{i\boldsymbol{k}\boldsymbol{T}} u_k(\boldsymbol{r}), \tag{1.8}$$

where $\boldsymbol{T}$ is a lattice vector and $\boldsymbol{k}$ is a wave vector in the reciprocal space. The wave vector equals $\boldsymbol{k} = \frac{2\pi l_i}{L_i}$ in a direction i, using Born-von Kármán periodic boundary conditions

[11], with l_i equals 0, ±1, ±2, ..., $\frac{n_i}{2}$ and L_i the length of the crystal in i direction in real coordinates ($L_i = n_i a$, n_i = number of unit cells, a = lattice vector in i direction). Wave function in the periodic potential of a crystal can be treated as a modulated plane wave composed of a function with the periodicity of the lattice $u_k(\boldsymbol{r})$ and a phase factor $e^{i\boldsymbol{kT}}$. Translation by a lattice constant changes a crystal wave function by a fixed phase, expressed by a quantum number k. The consequence of the Bloch theorem is that we can restrict calculations of periodic systems to a infinitely repeated unit cell. In the reciprocal space (k-space) the smallest repeating unit cell is called the first Brillouin zone (1.BZ), partitioned into k points that are identical upon the translation by the reciprocal lattice vector. With increasing crystal size, the spacing between the k points become negligible because the number of k points within the first Brillouin zone equals to the number of unit cells in the crystal. The Schrödinger equation solved for every k point within the 1.BZ results into a set of eigenvalues giving rise to the band structure of the crystal [10], [11].

1.2. Methods to solve electronic structure problem

The most problematic term in the Hamiltonian is the non-classical electron-electron interaction. This term has to account for the electronic exchange and correlation, both difficult to solve exactly. The correlation term is a Coulombic repulsion that affects all pairs of electrons regardless of their spins and treats the correlated motion of electrons. The exchange is a consequence of the Pauli exclusion principle that restricts two electrons (or fermions) of the same spin to occupy the same orbital. This interaction is also responsible for the orbital filling summarized in the Hund's rules, which state that orbitals are first half filled by electrons with parallel spins. This is caused by the exchange hole around each electron, the region where no other electron of the same spin can be found. Electrons with the same spin produce less shielding from the nucleus than electrons with antiparallel spin what results in lower energy of the system due to increased electron-nucleus attraction [12]–[14].

The simplest computational approach is to neglect both exchange and correlation. This is the choice in the Hückel theory used by the molecular computational chemistry, using the Linear combination of atomic orbitals method (LCAO) to construct the many-body wave function [9], [15]. Within the semi-empirical Hückel theory, the diagonal Hamiltonian matrix elements that are results of the secular equation are set equal to the experimental negative ionization energies and the off-diagonal terms are also derived from experimental data or equal zero. Hamiltonian matrix elements are products of variational minimization of energy, more detailed discussion is in the section 1.4. The overlap of neighbouring orbitals is neglected within the simplest Hückel theory. The feature that is common with the following methods is that the many-body wave function is treated as a combination of single electron wave functions [9], [12].

The so called Hartree method [16] deals with the exchange through the average effective potential that electrons feel. Electron-electron interactions are approximated by an electron in a potential created by all the other electrons without considering the correlation. This method is known as a independent particle approach and the Hartree method is also called the non-interacting method. Since we assume non-interacting electrons, the wave function can be constructed as a combination of one-electron wave functions, so called Hartree product. Partial energies are calculated for each electron and summed up to form the total energy. The one-electron Hamiltonian has the same kinetic energy and a nuclear attraction as in Equation 1.4, inter-electron interactions are partially described by the added interaction potential V_i

$$V_i(\boldsymbol{r_i}) = \frac{e^2}{4\pi\varepsilon_0} \sum_{i \neq j} \int \frac{\rho_j(\boldsymbol{r}_j)}{\boldsymbol{r}_{ij}} d\boldsymbol{r_j}, \tag{1.9}$$

where an electron i interacts with all the other electrons j, ρ_j is the charge density of an electron j defined as a square magnitude of its orbital wave function. The position of two electrons is defined by the vector $\boldsymbol{r}_{ij}$. Within this approximation the electron spin is not accounted for, only selection rule is that each orbital can be filled by two electrons. The solution of the Hartree method is obtained by the self-consistency cycle, starting with trial LCAO orbital wave functions for which an interaction potential is constructed. The one-electron Schrödinger equation is solved for every electron using the variational principle (Equation 1.6). Calculated Hamiltonian and overlap matrix elements are used to determine basis function coefficients, from which new improved orbitals are constructed and the cycle continues until the old and the new wave function do not differ (differ less than by a convergence criterion) [6], [9], [12], [17]. A major drawback of this approximation is that it fails to fulfill one of the defining characteristics of electron wave function - antisymmetry.

Better description of the electronic interaction is obtained by the Hartree-Fock (HF) method that works with the exact exchange integrals and properly antisymmetrized wave function, written as a Slater determinant. The Slater determinant consists of single spin-orbitals that are functions of a position and a spin. The Slater determinant is organized in the way that each row belongs to one-electron and each column represent one orbital. An interchange of two electrons is the same as a swap of two rows what leads to a sign change of the determinant what satisfies the antisymmetry rule. Also having two electrons with the same spin in the same orbital is the same as having two equal columns in the determinant which means the determinant is zero, satisfying the Pauli principle. The Hartree-Fock approximation is, as well, an independent particle method where electrons interact through an average potential. Electron-electron interactions are divided into a spin independent direct interaction and a spin mediated or exchange interaction. The eigenvalue problem in the Hartree-Fock approximation for a single Slater determinant wave function is of the form

$$\hat{F}(i)\psi_i^{\sigma}(\boldsymbol{r}_i) = \varepsilon_i \psi_i^{\sigma}(\boldsymbol{r}_i), \tag{1.10}$$

where $\hat{F}(i)$ is the Fock operator, $\phi^{\sigma}(x_i)$ is a one-electron i-th spin-orbital and ε_i is the eigenvalue (energy level) of the i-th spin-orbital (electron). The Fock operator is written as

$$\hat{F}(i) = \hat{T} + \hat{V}_{ext} + \hat{V}_{HF}^{\sigma}(i), \tag{1.11}$$

where the first two terms are defined in Equation 1.4 and the last term is the Hartree-Fock potential, defied as

$$\hat{V}_{HF}^{\sigma}(i) = \frac{e^2}{4\pi\varepsilon_0}\left[\sum_{j,\sigma_j}\int \frac{\rho_j^{\sigma_j}(\boldsymbol{r_j})}{\boldsymbol{r}_{ij}} d\boldsymbol{r_j} - \left(\sum_j \int \frac{\psi_j^{\sigma *}(\boldsymbol{r}_j)\psi_i^{\sigma}(\boldsymbol{r}_j)}{\boldsymbol{r}_{ij}} d\boldsymbol{r_j}\right)\frac{\psi_j^{\sigma}(\boldsymbol{r}_i)}{\psi_i^{\sigma}(\boldsymbol{r}_i)}\right]. \tag{1.12}$$

The positive term is a direct coulomb interaction (also called the Hartree term) between electrons of any spin σ and the negative term is the exchange interaction between electrons of the same spin. Solution of the Hartree-Fock approximation contains the exact exchange energy, however the correlation is completely left out. Another difficulty is that the variation leads to the Roothan equations that contain double integrals and the number of integrals for calculation scales with the fourth power of the number of basis functions [6], [9], [15], [17].

All methods mentioned in this section are used mainly for molecular computational chemistry. A notable step towards quantum mechanical calculations applicable to solid state materials is the density functional theory (DFT).

1.3. Density Functional Theory

As its name suggests, within the DFT we abandon the many-body wave function that is dependent on 3N spatial variables (N = number of electrons) and use electronic density instead, which depends only on three spacial variables. Hohenberg and Kohn shown in 1964 that the electronic density can be used as an functional argument in calculation of any property of a system [1], [18]. The electron density is calculated from single electron wave functions

$$n(\boldsymbol{r}) = \sum_i^N |\psi_i(\boldsymbol{r})|^2, \tag{1.13}$$

where $\psi_i(\boldsymbol{r})$ are the one-electron orbitals. The total number of electrons N is obtained by integration of density over all space

$$N = \int n(\boldsymbol{r}) dr. \tag{1.14}$$

The main idea of the DFT is that we don't need the full many-body wave function to obtain the total energy and to reproduce vast number of system's properties. Instead, we can obtain the same results from the knowledge of the electron density. However, the exact functional dependence of the energy on the density is unknown and we still need to make approximation of electron-electron interactions.

1.3.1. The Hohenberg-Kohn theorems

The applicability of the electron density as a fundamental parameter within first principles calculation is reasoned in two theorems [1] that are at the foundation of DFT. The first Hohenberg-Kohn theorem says that for any system of interacting particles, the external potential, up to an additive constant, can be determined uniquely by the ground state particle density $n_0(\boldsymbol{r})$. This means that there is a one to one correspondence between the ground state density and the external potential. Since the Hamiltonian is defined by the external potential, we can state that given the ground state electron density, all ground state properties of the system can be determined. A simple proof for degenerate ground state energy as well as more general proof given by Levy and Lieb can be found in ref. [6].

The second theorem proposed by Hohenberg and Kohn says that for energy, an universal functional of the electron density can be defined, valid for any external potential. The exact ground state is then the global minimum value of this functional and the density that minimizes the energy functional most is the ground state density. The second theorem basically establishes the variational principle in DFT. This means that we only need an exact energy functional to determine both the ground state energy and electron density by a self-consistent cycle.

The Hohenberg-Kohn theorems can be summarised into a statement that a mapping from a ground state density to an external potential exists (that is felt by electrons due to nuclei, basically defines a crystal), the existence of a universal energy functional of electron density and the variational principle with respect to the density.

1.3.2. The Kohn-Sham equations

The ansatz proposed by Kohn and Sham replaces the original many-body problem with an auxiliary independent particle problem [6], [19] that is easier to solve. The ansatz assumes that the ground state density of the original real system of interacting particles is the same as the one of a chosen non-interacting particles. These independent particle equations - the Kohn-Sham (KS) equations - are exactly solvable and all many-body terms are contained within the new exchange-correlation functional. The Hamiltonian can be written as a sum of one-particle operators, the many-body wave function is a Slater determinant of single-electron eigenfunctions (orbitals) and the total energy is a sum of partial one-electron eigenvalues. Single electron eigenfunctions have no

particular physical meaning, they just serve as a mathematical tool for construction of the charge density and for solving the Schrödinger equation to obtain single-electron energies.

The total energy within DFT is defined as a functional of the electron density with components

$$E[n] = T_S[n] + E_{ext}[n] + E_H[n] + E_{II} + E_{xc}[n], \tag{1.15}$$

the n in the square brackets denotes functional of the electron density. The first term is the kinetic energy of a system of non-interacting particles given by the expectation value of the kinetic energy operator

$$T_S[n] = \langle \psi_i[n] | \hat{T}_s | \psi_i[n] \rangle = -\frac{\hbar^2}{2m} \sum_i^N \int \psi_i^*(\boldsymbol{r}) \nabla^2 \psi_i(\boldsymbol{r}) d\boldsymbol{r}. \tag{1.16}$$

Due to the independent nature of particles, the total kinetic energy is a simple sum of single particle kinetic energies. The subscript S reminds us that this kinetic energy is not an exact one but of a system of non-interacting particles that reproduce the true ground state density. The kinetic energy is a implicit density functional (the density is not a variable of the kinetic energy functional) but it is an explicit orbital functional and orbitals depend on density.

The second term in Equation 1.15 is the energy of interaction of electrons with the external potential of nuclei, which has the form

$$E_{ext}[n] = \int \hat{V}_{ext} n(\boldsymbol{r}) dr = -e^2 \sum_R Z_R \int \frac{n(\boldsymbol{r})}{|\boldsymbol{r} - \boldsymbol{R}|} d\boldsymbol{r}, \tag{1.17}$$

what is the external potential operator is defined in Equation 1.4 expressed using the density.

The third term in Equation 1.15 is the Hartree energy of classical electron-electron interactions. It's formulation in terms of density is

$$E_H[n] = \frac{e^2}{2} \iint \frac{n(\boldsymbol{r}) n(\boldsymbol{r'})}{|\boldsymbol{r} - \boldsymbol{r'}|} d\boldsymbol{r} d\boldsymbol{r'}. \tag{1.18}$$

The nuclear interaction E_{II} has an additive character and the last term $E_{xc}[n]$ is the exchange-correlation energy. This energy term comprises the difference between a real system and a system of non-interacting particles and incorporates errors made by using the kinetic energy of non-interacting electrons and by treating the inter-electron interaction classically. Operator for this energy is the only one that is not explicitly known and the precision of calculations depends on the level of approximation of this term.

The solution for the Kohn-Sham system can be looked at as a minimization of the energy functional with respect one-electron orbitals. The minimization of energy can be expressed as

$$\frac{\delta E[n]}{\delta \psi_i^*(\boldsymbol{r})} = \frac{\delta T_S[n]}{\delta \psi_i^*(\boldsymbol{r})} + \left[\frac{\delta E_{ext}[n]}{\delta n(\boldsymbol{r})} + \frac{\delta E_H[n]}{\delta n(\boldsymbol{r})} + \frac{\delta E_{xc}[n]}{\delta n(\boldsymbol{r})}\right] \frac{\delta n(r)}{\delta \psi_i^*(\boldsymbol{r})} = 0, \tag{1.19}$$

$$\frac{\delta T_S[n]}{\delta \psi_i^*(\boldsymbol{r})} = -\frac{\hbar}{2m}\nabla^2 \psi_i(\boldsymbol{r}); \frac{\delta n(\boldsymbol{r})}{\delta \psi_i^*(\boldsymbol{r})} = \psi_i(\boldsymbol{r}). \tag{1.20}$$

Here the minimization is done with respect to $\psi_i^*(\boldsymbol{r})$ but $\psi_i(\boldsymbol{r})$ gives the same result. Now we can define the energy functional variation through potentials

$$\frac{\delta E[n]}{\delta \psi_i^*(\boldsymbol{r})} = \frac{\delta T_S[n]}{\delta \psi_i^*(\boldsymbol{r})} + [v(\boldsymbol{r}) + v_H(\boldsymbol{r}) + v_{xc}(\boldsymbol{r})] \frac{\delta n(\boldsymbol{r})}{\delta \psi_i^*(\boldsymbol{r})} = 0, \tag{1.21}$$

where $v(\boldsymbol{r})$ is the external potential, $v_H(\boldsymbol{r})$ is the Hartree potential and $v_{xc}(\boldsymbol{r})$ is the exchange-correlation potential. The sum of these potentials is an effective potential $v_s(\boldsymbol{r})$, so that

$$\frac{\delta E[n]}{\delta \psi_i^*(\boldsymbol{r})} = -\frac{\hbar}{2m}\nabla^2 \psi_i(\boldsymbol{r}) + v_s(\boldsymbol{r})\psi_i(\boldsymbol{r}) = 0. \tag{1.22}$$

The one-electron Kohn-Sham equation then has the form

$$\left[-\frac{\hbar}{2m}\nabla^2 + v_s(\boldsymbol{r})\right] \psi_i(\boldsymbol{r}) = \varepsilon_i \psi_i(\boldsymbol{r}). \tag{1.23}$$

A set of Kohn-Sham equations for non-interacting electrons within an effective potential is solved in a self consistent cycle resulting in the ground state density $n_0(\boldsymbol{r})$ and the ground state energy E_{KS}. This solution is exact as soon as we use exact exchange-correlation potential.

The necessity for the self consistency is given by the fact that the output of the Kohn-Sham equations (wave function) defines its input (electron density). The starting point of the self consistent cycle resides in guessing an initial density to form all the functionals for which the KS equations are solved. By solving them (diagonalization of the the Hamiltonian matrix) we obtain a new set of occupied orbitals (corresponding to the N lowest eigenvalues) which then form a new density that is more or less different from the initial one. This procedure continues iteratively until the accuracy condition is satisfied. The work diagram of a self consistent cycle is sketched in Figure 1.1.

1.3.3. Exchange and correlation

The exchange-correlation functional incorporates the difference between an approximation and the exact solution and is the factor defining the accuracy of a calculation. Both

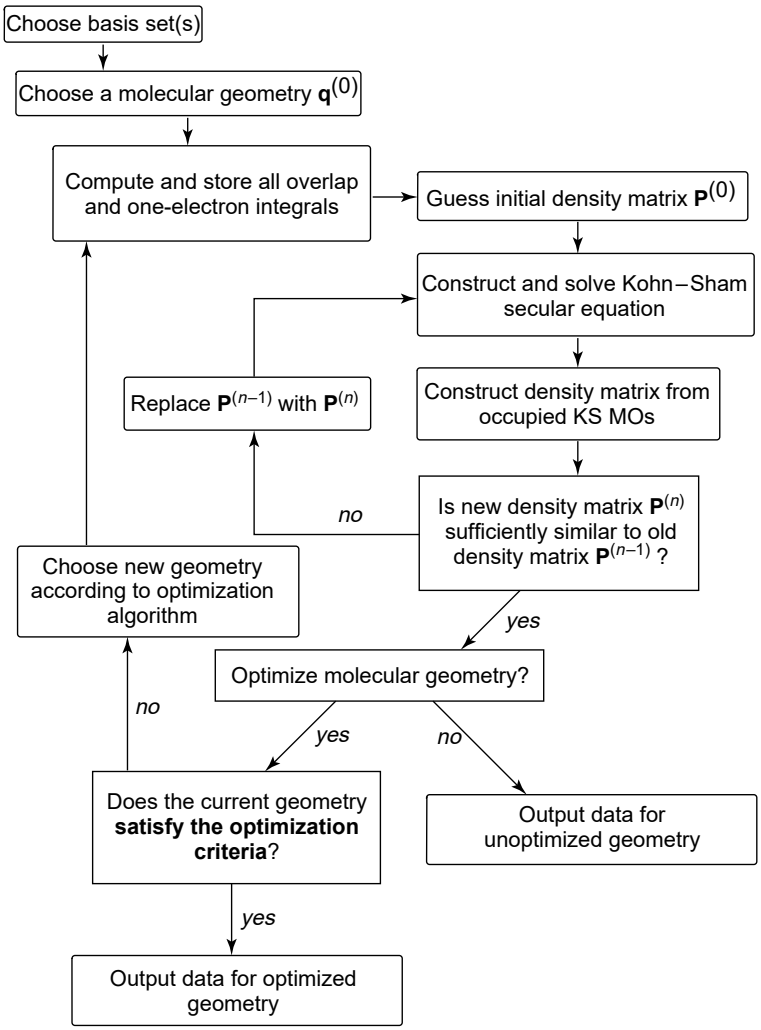

Figure 1.1: Graphical interpretation of the self consistent cycle solution for stable electronic structure and geometry. Considering electronic structure calculation, we first have to choose a basis set (mathematical formulation used for construction of orbitals), the cycle starts with a guessed initial density for which KS equations are constructed and solved. New density is built and the cycle continues until the convergence. Diagram taken from [9].

exchange and correlation describe mutual electron repulsion hence we can assign them the role of a region around each electron where other electrons (or part of electrons) have zero probability density. This region is called the exchange hole (Fermi hole) and the correlation hole (Coulomb hole) [20], [21]. To describe such behavior of electrons we introduce the pair density, that is obtained by integration of the full N-electron wave function over the spatial and spin coordinates of electrons 3 to N

$$n(\boldsymbol{r}_1,\boldsymbol{r}_2) = \frac{N(N-1)}{2}\int ... \int \Psi^*[n](\boldsymbol{r}_1,\boldsymbol{r}_2,...,\boldsymbol{r}_N)\Psi[n](\boldsymbol{r}_1,\boldsymbol{r}_2,...,\boldsymbol{r}_N)d\sigma_1 d\sigma_2 d\boldsymbol{r}_3...\boldsymbol{r}_N. \tag{1.24}$$

Its interpretation is the probability density of finding one-electron at $\boldsymbol{r}_1$ and simultaneously a second electron at $\boldsymbol{r}_2$ [20], [22], [23]. The pair density can be rewritten in terms of exchange-correlation hole as follows

$$n(\boldsymbol{r}_1,\boldsymbol{r}_2) = n(\boldsymbol{r}_1)[n(\boldsymbol{r}_2) + n_{xc}(\boldsymbol{r}_1,\boldsymbol{r}_2)], \tag{1.25}$$

where $n(\boldsymbol{r}_1,\boldsymbol{r}_2)$ is the pair density, $n(\boldsymbol{r}_1)$ and $n(\boldsymbol{r}_2)$ are one-electron densities and $n_{xc}(\boldsymbol{r}_1,\boldsymbol{r}_2)$ is the exchange-correlation hole density. If we expand terms in brackets in Equation 1.25, we get the multiplication of one particle densities what represents independent particle interaction, as in the Hartree term 1.18, plus the exchange-correlation pair density $n(\boldsymbol{r}_1)n_{xc}(\boldsymbol{r}_1,\boldsymbol{r}_2)$ [22], [23].

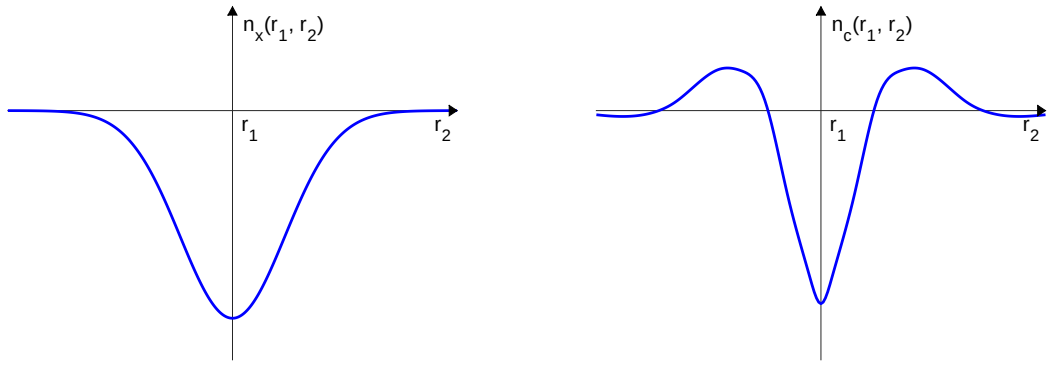

(a) (b)

Figure 1.2: Schematic interpretation of a) exchange hole where the pair density of electrons with the same spin is lowered around electron at $\boldsymbol{r}_1$ and b) correlation hole around an electron.

The exchange-correlation energy functional can be expressed in the form

$$E_{xc}[n] = -\frac{e^2}{2}\iint \frac{n(\boldsymbol{r}_1)n_{xc}(\boldsymbol{r}_1,\boldsymbol{r}_2)}{|\boldsymbol{r}_1-\boldsymbol{r}_2|} = \int n(\boldsymbol{r}_1)\varepsilon_{xc}[n](\boldsymbol{r}_1)d\boldsymbol{r}_1, \tag{1.26}$$

where $\varepsilon_{xc}[n]$ is an energy per electron at point $\boldsymbol{r}$ that depends only on the density in the vicinity of $\boldsymbol{r}$. The exchange-correlation energy is the energy of the electrostatic interaction between an electron and its exchange-correlation hole.

We can treat $E_{xc}[n]$ as the sum of exchange $E_x[n]$ (repulsion of the same spin electrons due to the Pauli principle) and correlation $E_c[n]$ (more complex term, defined as a difference between HF and exact energy, instantaneous electron-electron interactions) terms which both lower the total energy. The exchange-correlation hole as well can be separated into exchange and correlation holes $n_{xc}(\boldsymbol{r}_1,\boldsymbol{r}_2) = n_x(\boldsymbol{r}_1,\boldsymbol{r}_2) + n_c(\boldsymbol{r}_1,\boldsymbol{r}_2)$. The exchange hole around an electron, Figure 1.2a, is always negative, it integrates to -1

(it excludes one-electron) and relation $n_x(\boldsymbol{r}_1, \boldsymbol{r}_2) \geq -n(\boldsymbol{r}_2)$ applies. The correlation hole (Figure 1.2b) density integrates to zero.

A crucial part of any *ab initio* method for solving the electronic structure of matter is an accurate approximation to the exchange-correlation functional. One of the simplest approaches used within DFT is the local density approximation (LDA) introduced by Kohn and Sham [19] used when electron density varies slowly with position. Being local means that it in principle can be calculated at some position $\boldsymbol{r}$ exclusively from the value of $n(\boldsymbol{r})$ at that position. It is expressed as

$$E_{xc}^{LDA}[n] = \int n(\boldsymbol{r}) \varepsilon_{xc}^{unif}[n] d\boldsymbol{r}, \tag{1.27}$$

where $\varepsilon_{xc}^{unif}[n]$ is the exchange-correlation energy per electron of the infinite uniform electron gas with the density n. This is a system of interacting electrons with spatially constant density. Within the LDA, the exchange-correlation of an inhomogeneous system of electrons is approximated for each space point by the exchange-correlation of the uniform electron gas of the same density. The exchange part can be calculated analytically

$$\varepsilon_x^{unif}[n] = -\frac{3}{4}\left(\frac{3}{\pi}\right)^{\frac{1}{3}} n(\boldsymbol{r})^{\frac{1}{3}}. \tag{1.28}$$

The correlation part has to be obtained numerically for a number of densities using quantum Monte Carlo simulations [22], [24]. LDA works surprisingly well also for systems with strongly varying electron density (highly inhomogeneous) even though it poorly describes the electron pair density and the exchange hole. The electron interaction is however dependent only on the spherical average of the pair density and LDA predicts reasonable spherical average pair density and exchange hole [12], [23].

The electron density in real systems is in general dissimilar to spatially uniform density of an homogeneous electron gas. An improvement of E_{xc} is gained by using the generalized gradient approximation (GGA) [25] that improves the exchange-correlation by making it depend not only on density at each point but also on the magnitude of the gradient of the density, that is how does the density change locally. Therefore GGA is dubbed a semi-local approximation. Most of GGA approximations use a correction additive term to the LDA. In comparison with LDA, GGA improves total energies, atomization energies, energy barriers and structural energy differences. Some of widespread GGA parametrizations are B88 (Becke) [26], LYP (Lee-Yang-Parr) [27], PW91 [28] or PBE [6], [9], [12], [29].

Even though LDA and GGA provide impressive and accurate results in most cases, they tend to incorrectly describe ground state properties of some materials. Such examples are underestimated band gap width of semiconductors, prediction of metallic character of Mott insulators and overdelocalization of valence electrons. This tendency to delocalize electrons results in promotion of metallic character what is problematic

for highly correlated systems. Such systems contain localized electrons including d and f orbital electrons. Another intrinsic error within the DFT is the self-interaction error contained in Coulombic density (electron-electron) interaction that is not cancelled exactly by the exchange-correlation term. There are some methods that are trying to address these drawbacks like hybrid functionals or corrective Hubbard model, latter of which is discussed in the next section.

1.3.4. DFT+U

One of the corrective approaches is the implementation of Hubbard-like U parameters which account for the underestimated Coulomb interactions between electrons. The DFT+U method should better describe the electronic structure of strongly correlated electrons, involving d or f orbitals, by implementation of an additional Coulomb repulsion acting on electrons on the same atom that leads to enhanced localization of electrons [30]–[32]. Within this method, less correlated valence electrons are treated by standard LDA or GGA approximation and more localized orbitals are treated by additional on-site Coulomb interaction that hinders the hopping of electrons between neighbouring sites and therefore localizes them[33]. The total energy is corrected by an additive term containing the Hubbard energy functional E_{Hub}

$$E^{DFT+U}[n] = E^{DFT}[n] + E_{Hub}[n^{I\sigma}_{mm'}] - E_{dc}[n^{I\sigma}], \tag{1.29}$$

where E^{DFT} is the energy from the standard DFT calculation and E_{dc} is a double-counting term that has to be subtracted because of the additive nature of the correction term. The Hubbard energy functional depends on the occupational number $n^{I\sigma}_{mm'}$ usually defined as

$$n^{I\sigma}_{mm'} = \sum_{k,j} f^{\sigma}_{kj} \langle \psi^{\sigma}_{kj} | \phi^{I}_{m'} \rangle \langle \phi^{I}_{m} | \psi^{\sigma}_{kj} \rangle, \tag{1.30}$$

here ψ^{σ}_{kv} are occupied Kohn-Sham orbitals where k represent k-points (sampling of 1.BZ) and j band indexes, ϕ^{I}_{m} are states of a localized basis set. Index m labels the localized states (magnetic quantum number) on the atomic site I, σ is the spin and f^{σ}_{kj} are given by the Fermi-Dirac occupation distribution of the Kohn-Sham orbitals. In Equation 1.29 $n^{I\sigma} = \sum_m n^{I\sigma}_{mm'}$. The occupation number is calculated as the projection of occupied Kohn-Sham orbitals on the states of a localized basis set that is then treated separately by the corrective term. The simplest DFT+U energy functional has the form

$$E_{DFT+U} = E_{DFT} + \sum_{I} \left[\frac{U^I}{2} \sum_{m,\sigma \neq m',\sigma'} n^{I\sigma}_{m} n^{I\sigma'}_{m'} - \frac{U^I}{2} n^I (n^I - 1) \right], \tag{1.31}$$

where Hubbard U^I is the effective electronic interaction on atom I, $n^{I\sigma}_{m}$ are the localized orbitals occupation numbers. Terms in the square brackets are the Hubbard and the

double-counting terms. The Hubbard potential is repulsive for less than half filled orbitals and attractive for more than half filled. This decreases the tendency to partially fill orbitals which lowers the tendency of orbital hybridization with neighboring atoms. Another consequence of this is a favored electron localization and energy gap opening when the on-site repulsion exceeds the kinetic energy minimization due to delocalization [34], [35]. The formulation in Equation 1.31 is not invariant under the rotation of atomic orbital basis set used to determine the occupation numbers what causes a dependence of results on the choice of the localized basis set. In a rotationally invariant formulation the orbital dependence of E_{Hub} is inspired by the HF method [36] and its simplified application was introduced by Dudarev et al. [37].

The values of U parameter can be obtained in a semiempirical way by fitting calculated results to experimental data or from *ab initio* calculations using the linear-response theory [38], [39]. The advantage of DFT+U approach over other correction methods, like hybrid functionals, is the low computational cost, just slightly more expensive than the standard LDA or GGA method.

1.3.5. Plane wave basis set

In order to solve the KS equations and determine the electron density we need to assign a functional form to one particle orbitals. Mathematical functions that construct wavefuctions are called basis functions. Two types of basis functions widely used are localized atomic basis sets (Gaussian, Slater type, Muffin-Tin orbitals) centered around a nucleus or delocalized plane wave basis sets. The use of the plane wave basis set is very convenient especially for periodic lattices, their advantages are efficiency (fast Fouruer transform is easy to perform), they are not centered on an atom and can be used for any atomic type. However, we need a large number or plane waves to approximate orbitals and representation of chemical (bonding) information is not straightforward.

The KS orbitals expanded in the plane wave basis are written as

$$\psi_i(\boldsymbol{r}) = \frac{1}{\sqrt{\Omega}} \sum_{\boldsymbol{G}} c_i(\boldsymbol{G}) e^{i\boldsymbol{G}\cdot\boldsymbol{r}}, \tag{1.32}$$

here $\boldsymbol{G}$ is a reciprocal lattice vector, $c_i(\boldsymbol{G})$ are expansion coefficients, $\boldsymbol{r}$ and Ω are real space coordinates and volume of the primitive cell. The number of plane waves used for the expansion is defined by the cutoff energy

$$\frac{\hbar^2}{2m_e}|\boldsymbol{G}|^2 \leq E_{cut}. \tag{1.33}$$

Since we need plenty of plane waves to approximate even relatively smooth functions, the real potential close to the nucleus where wave function is defined by rapid oscillations is replaced by a pseudopotential in which no original features the wave function are kept. Wave function in the valence region is unchanged. The necessary size of the

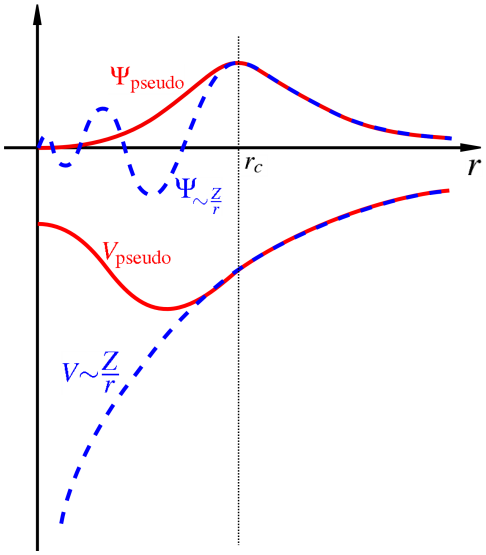

Figure 1.3: Sketch of a pseudopotential and a corresponding pseudo-wave function. Pseudopotentials substitute region around nuclei in order to smoothen the wave function in the core region, from [40].

plane wave basis set is remarkably lowered, another advantage of this approximation is the fact that we get rid of the singularity in potential at position of nucleus, which is captured in Figure 1.3. Pseudoatoms formed this way must preserve the same scattering behavior as original atoms. Pseudopotentials reduce number of electrons for which KS equations have to be evaluated to valence electrons solely, this however results in a loss of information. [41], [42].

A more precise description of wave function in the core region can be obtained by the projector augmented wave method (PAW) [43]. This method transforms the full wave function onto an auxiliary smooth wave function that can be represented in a plane wave expansion. Within the PAW, the wave function is divided and treated separately in core and valence region, core electrons are projected using a slowly varying local basis set, as Figure 1.4 shows. A plane wave based PAW wave function is expressed as

$$|\psi_j\rangle = |\tilde{\psi}_j\rangle + \sum_{\mu} \left(|\phi_\mu\rangle - |\tilde{\phi}_\mu\rangle\right) \left(\langle \tilde{p}_\mu | \tilde{\psi}_j\rangle\right), \tag{1.34}$$

here $|\tilde{\psi}_j(\boldsymbol{k})\rangle$ is a pseudo-space function that fits the wave function outside the core sphere and the sum represents the augmentation part that treats orbitals within the core sphere. The pseudo-space wave function has the form of Equation 1.32. The augmentation part is composed of the all-electron partial waves ϕ_μ and the pseudo waves $\tilde{\phi}_\mu$. The projector functions $\tilde{p}_\mu$ probe the character of the pseudo wave function and its nodeless character is replaced by the correct function. Projector functions are localized within their own core region and their functional form depend on orbital type.

The advantage of the PAW is that it keeps the full wave function with all electrons only that the integrals are evaluated as a combination of integrals of smooth functions

in the interstitial region and radial integration of localized functions of core electrons [6], [41]–[44].

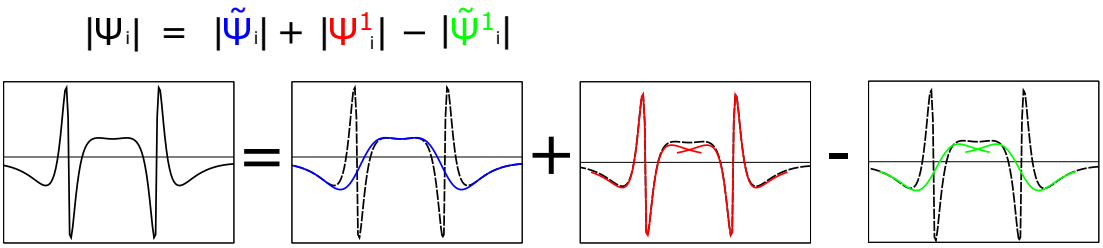

Figure 1.4: Scheme of the PAW wave function, the black curve is the real wave function, the blue curve represents the pseudo wave function that behaves well in the interstitial region, red and green wave functions are defined only within the augmentation region, from [45], modified.

The core electrons are usually pre-calculated in an atomic environment and kept unchanged throughout the calculation, this is called the frozen core method. The density and the energy of the core electrons are calculated and imported from the corresponding isolated atoms. The frozen core approximation is justified by the fact that core electrons do not directly contribute to bonding between atoms [41].

1.4. Chemical bonding analysis

Plane wave basis sets are very convenient choice for electronic structure calculations of periodic structures where Bloch's theorem is valid. However, plane waves do not posses intuitive bonding information due to their delocalized character. To obtain chemical information we have to transform the wave function into a local basis set centered around every atom. A quite obvious approach used to describe a wave function with a local basis set is the linear combination of atomic orbitals (LCAO) [46].

1.4.1. LCAO

Within the LCAO a wavefuntion is expanded in terms of local basis functions with character of isolated atom orbitals as

$$\psi_i(\boldsymbol{r}) = \sum_A \sum_{\substack{\mu=1 \\ \mu \in A}}^{n} c_{\mu i} \varphi_\mu(\boldsymbol{r}), \tag{1.35}$$

where atomic orbitals $\varphi_\mu(\boldsymbol{r})$ are multiplied by expansion coefficients $c_{\mu i}$ and summed (n is a number of basis functions used) to produce i-th molecular (crystal) orbital located on atom A. The subscript μ denotes a basis function. In order to construct LCAO wave function, we need to find coefficients $c_{\mu i}$ such that the wave function corresponds

to the lowest energy of a system. Energy is evaluated as an expectation value of the Hamiltonian as

$$E_i = \frac{\sum_A \sum_B \sum_\mu \sum_\nu \langle c_{\mu i}\varphi_\mu|\hat{H}|c_{\nu i}\varphi_\nu\rangle}{\sum_A \sum_B \sum_\mu \sum_\nu \langle c_{\mu i}\varphi_\mu|c_{\nu i}\varphi_\nu i\rangle} = \frac{\sum_A \sum_B \sum_\mu \sum_\nu c^*_{\mu i}c_{\nu i}H_{\mu\nu}}{\sum_A \sum_B \sum_\mu \sum_\nu c^*_{\mu i}c_{\nu i}S_{\mu\nu}}. \tag{1.36}$$

Integrals in 1.36 result in Hamiltonian matrix elements $H_{\mu\nu}$ (result of resonance integrals in the numerator) and overlap matrix elements $S_{\mu\nu}$ (result of overlap integrals in the denominator). In order to determine the coefficients, energy minimization is performed by differentiation of Equation 1.36 with respect to all coefficients $\frac{\partial E_i}{\partial c_{ki}} = 0$ (k runs through all n coefficients), what gives a set of equations

$$\sum_\mu^n \boldsymbol{c}_{\mu i}(\mathrm{H}_{\mu k} - E_i \mathrm{S}_{\mu k}) = 0, \tag{1.37}$$

where n is a number of basis functions used to approximate the wave function, $\boldsymbol{c}_{\mu i}$ is the vector of the expansion coefficients, $\mathrm{H}_{\mu k}$ and $\mathrm{S}_{\mu k}$ are matrix elements defined in 1.36. The variation (minimization) process leaves us with the set of n equations for every orbital energy E_i. In order to find roots of Equation 1.37, we have to solve a set of n equations in n unknowns. In matrix notation, a non-trivial solution can be obtained if the determinant of the matrix containing Hamiltonian and overlap elements equals zero. This determinant is the so called secular determinant and its solution gives us a set of n coefficients for every energy E_i. Consequently the LCAO wave function is defined by the lowest $\frac{n}{2}$ energies (degenerate states) [9], [47].

1.4.2. Electron population analysis

Chemical bonding as we characterize it depends on spatial distribution of electron density in material. One of the partitioning schemes is the Mulliken analysis that divides overall electron density into atomic contributions and bonding electrons. Using the LCAO approach, the total number of electrons in a system is given by the expression

$$N = \sum_i^m \int \psi_i^*(\boldsymbol{r})\psi_i(\boldsymbol{r})d\boldsymbol{r} = \sum_i^m \int \sum_A \sum_{\substack{\mu \\ \mu\in A}} c_{\mu i}\varphi_\mu^*(\boldsymbol{r}) \sum_B \sum_{\substack{\nu \\ \mu\in B}} c_{\nu i}\varphi_\nu(\boldsymbol{r})d\boldsymbol{r}, \tag{1.38}$$

where we sum through all occupied orbitals m. Since we use normalized atomic orbitals basis set $\int|\varphi_\mu|^2 = 1$ (probability density of finding an electron somewhere in space is 1) and for $\mu \neq \nu$ the integral $\int \varphi_\mu\varphi_\nu = S_{\mu\nu}$ equals off-diagonal overlap matrix elements, we can write

$$N = \sum_A \sum_{\substack{\mu \\ \mu\in A}} \sum_i^m f_i \left(c^2_{\mu i} + \sum_{A\neq B} \sum_{\substack{\nu \\ \nu\in B}} f_i c_{\mu i}c_{\nu i}S_{\mu\nu} \right), \tag{1.39}$$

where the last term is the Mullikken overlap population [47]–[49]. In 1.39 f_i is the occupation number of i-th orbital with possible values 0, 1 or 2 in the spin-restricted approach that is spin up and down electrons occupy the same orbitals. Mulliken analysis fraction electrons to those including only squares of single atomic orbital (they belong to single atom) and electrons including product of different atomic orbitals (shared electrons) that are responsible for bonding if those orbitals are centered on different atoms. In Equation 1.39 the first term describe atom-centered electrons and is called the net population, the second term is the overlap population. We can further assign shared electrons to atoms by simply adding exactly half of the overlap population to on-site electrons, what is then called the gross population [9], [47].

The use of non-orthogonal basis set in the Mulliken analysis can lead to unphysical results like negative population of orbitals. Also, within the Mulliken analysis, we divide the overlap population equally between atoms which is usually a bad assumption namely for compounds that consist of different elements where electron distribution can significantly vary from an even distribution. Another population analysis proposed by Löwdin works with atomic orbitals first transformed into an orthonormal set of basis functions using symmetric orthogonalization scheme

$$\chi_\mu = \sum_\nu S_{\mu\nu}^{-\frac{1}{2}} \varphi_\nu, \tag{1.40}$$

where μ and ν run over all basis functions and $S_{\mu\nu}^{-\frac{1}{2}}$ is the inverse of the square root of the overlap matrix [50], [51]. New wave function is formulated as LCAO of the new basis functions χ_μ and new coefficients are determined from original coefficients $c_{\mu i}$. After orthogonalization, the overlap matrix becomes the unit matrix, meaning that diagonal terms equal one and off-diagonal terms are zero. Therefore, we don't have to split shared electrons but we already obtain population for individual atoms [9].

1.4.3. Bonding indicator functions

To analyze orbital overlap in crystals, we have to consider consequences of the Bloch's theorem, that is a dependence on new quantum mechanical variable k represented by a vector residing within the first Brillouin zone. Crystal orbitals are built as a linear combination of Bloch functions (defined as atomic orbitals multiplied by the periodic phace factor) using k-dependent coefficients $c_{\mu i}(k)$ [52]. We can define a k-dependent electron density matrix as

$$P_{\mu\nu}(\boldsymbol{k}) = \sum_i^m f_i c_{\mu i}^*(\boldsymbol{k}) c_{\nu i}(\boldsymbol{k}), \tag{1.41}$$

and the k-averaged density matrix $P_{\mu\nu}$ as an integration of k-dependent density matrix $P_{\mu\nu}(\boldsymbol{k})$ over all k vectors [47].

The band structure of crystals is usually too complex for a simple interpretation and analytic tool for more intuitive interpretation is necessary. Density of states (DOS) function provides directionless averaged information about the electronic structure of materials as it assigns the number of one-electron states to an infinitely small energy interval. An useful remark is that DOS is given as a inverse slope of a given energy band. By differentiation of the density matrix

$$P_{\mu\nu} = \int^{\varepsilon_F} P_{\mu\nu}(E)dE, \tag{1.42}$$

we obtain the density of states matrix $P_{\mu\nu}(E)$ that expands the electronic structure and the electron distribution in terms of energy. Equation 1.39 can be written in terms of $P_{\mu\nu}(E)$ as

$$N = \int^{\varepsilon_F} \sum_A \sum_{\substack{\mu \\ \mu\in A}} \left(P_{\mu\mu}(E) + \sum_{A\neq B} \sum_{\substack{\nu \\ \nu\in B}} \mathrm{Re}[P_{\mu\nu}(E)S_{\mu\nu}] \right) dE, \tag{1.43}$$

where Re is the real part of the off-diagonal terms. The second term in brackets in 1.43 is the overlap population weighted density of states that provides information about electrons that participate on the bond formation. Technique based on this information is so called crystal orbital overlap population (COOP)

$$COOP_{\mu\nu}(E,\boldsymbol{k}) = \sum_i \mathrm{Re}[P_{\mu\nu}(\boldsymbol{k})S_{\mu\nu}(\boldsymbol{k})]\delta(\varepsilon - \varepsilon_i(\boldsymbol{k}));[\mu\in A, \nu\in B, A\neq B]\,. \tag{1.44}$$

COOP function for a specified pair interaction is defined basically by multiplication of the DOS function by the electron overlap of chosen orbitals positioned on different atoms, summed over all energy bands i. In order to get COOP of the inter-atomic interaction we have to sum COOP over all pairs of orbitals centered on interacting pair of atoms. This method partitions interactions into bonding for which COOP is positive, antibonding for which COOP is negative and nonbonding for which COOP function is zero [47], [53].

Another approach to obtain information about bonds is to determine energies of interaction instead of the overlap of orbitals. If, in contrast with COOP, we examine Hamilton matrix elements weighted density of states, we get the crystal orbital Hamilton population (COHP) function [54]

$$COHP_{\mu\nu}(E,\boldsymbol{k}) = \sum_i \mathrm{Re}[P_{\mu\nu}(\boldsymbol{k})H_{\mu\nu}(\boldsymbol{k})]\delta(\varepsilon - \varepsilon_i(\boldsymbol{k}));[\mu\in A, \nu\in B, A\neq B]\,. \tag{1.45}$$

Off-diagonal Hamilton matrix elements provide analysis of pair interactions in terms of energy contribution. As in the case of COOP, the bond analysis is based on COHP

summed over all off-site Hamilton matrix elements calculated for orbitals centered on interacting atoms. We define stabilizing (bonding) interactions as negative COHP and destabilizing (antibonding) as positive COHP. The strength of a bond is given by the value of integrated COHP (ICOHP) up to the Fermi level. [47], [53].

Generalized COHP function called density of energy (DOE) sums up all off-site (inter-atomic) as well as on-site (atomic) contributions into one function. The integration of DOE up to the Fermi level yields the band structure energy

$$E_{band} = \int^{\varepsilon_F} DOE(E)dE = \sum_A \sum_{\substack{\mu \\ \mu \in A}} \sum_{\substack{\nu \\ \nu \in B}} ICOHP_{\mu\nu} = \sum_i \varepsilon_i, \tag{1.46}$$

$$E_{tot} = E_{band} - E_{Hartree} + E_{xc} - \int v_{xc}(\boldsymbol{r})\rho(\boldsymbol{r})d\boldsymbol{r}. \tag{1.47}$$

The sum of all on-site and off-site ICOHPs gives the band structure energy or the sum of the Kohn-Shan eigenvalues ε_i, this, however, is not equal to the total energy of the system as 1.47 shows. Negative values of DOE are stabilizing and positive values indicate destabilizing states. This function allows us to analyze the effect of on-site interactions of electrons and the role of electrons that do not form bonds. The contribution of on-site interactions might be obtained by subtracting COHP summed over all interactions from the DOE function. This way we obtain a more comprehensive picture of electronic interaction on the stability of studied system [47], [53], [55], [56].

1.4.4. The LOBSTER package

The LOBSTER package (Local-Orbital Basis Suite Towards Electronic-Structure Reconstruction) was designed to calculate the COHP and other analytic tools mentioned in the previous section as an extension compatible with DFT and PAW codes [57]. However, these methods by definition require a local basis functions, therefore are not applicable for delocalized plane wave basis sets. The COHP is defined through the expansion coefficients of local atomic orbitals that form density matrix elements, hence the plane waves have to be projected on a local basis set [58], [59]. Projected density matrix element for band i must be obtained at every k-point as

$$P^{proj}_{\mu\nu i}(\boldsymbol{k}) = T^*_{i\mu}(\boldsymbol{k})T_{i\nu}(\boldsymbol{k}), \tag{1.48}$$

where $T_{i\mu}(\boldsymbol{k})$ and $T_{i\nu}(\boldsymbol{k})$ are elements of the transfer matrix that are defined as overlap between the i-th plane wave crystal band $\varphi_i(\boldsymbol{k})$ and the local orbitals $\psi_\mu(\boldsymbol{r})$ F

$$T_{i\mu}(\boldsymbol{k}) = \langle \varphi_i(\boldsymbol{k}) | \psi_\mu(\boldsymbol{r}) \rangle. \tag{1.49}$$

The choice of the local basis set is arbitrary. Expansion coefficients of the local basis set that we needed in the first place can be derived from the transfer matrix. More detailed procedure of the projection from PAW wave functions can be found in ref. [58].

2. Review of studied materials

A high demand for faster production and lower maintenance costs are driving forces in the material research oriented towards the engineering industry. From the materials point of view, the performance of highly loaded tools can be besides other enhanced by an application of protective surface layers. Nowadays, all extremely loaded tools regardless of used material are produced with a protective surface layer that increases their lifespan, enables higher work rates and temperatures, provides a better corrosion resistance and better friction properties. Some of the most important mechanical properties required form milling, drilling, cutting and other highly loaded tools are the toughness and the hardness. These tools are manufactured from materials like sintered carbides or tool steels and shielded with protective layers deposited on their surface. In this section the most widely used refractory coating materials are presented as well as promising boron based materials that are central to this thesis.

2.1. Conventional protective coatings

Research of the wear resistant coatings started in 1950s with titanium carbide TiC and titanium nitride TiN deposition on steel substrates [60] however TiN coating were first studied as protective layers in the 70s [61]. This material, with some composition changes or in combination with other coating materials, is still widely used today. Titanium nitride crystallizes in the B1 structure (NaCl lattice type) with density 5.22 g/cm^3 and a high temperature of melting around 2930 °C [62]. Advantageous properties of TiN are excellent adhesion, chemical inertness, resistance to higher temperatures, high hardness at least 2000 HV (Vickers hardness) [62], [63], low coefficient of friction and decorative gold color.

Development of hard protective coatings advaned with an introduction of multilayered films based on TiN and TiC or the carbonitride TiCN. Multilayered or gradient coatings combine qualities of different coating materials in order to increase the performance of the final film, for example a combination of high hardness lower layer and low friction upper layer. Another option for an increase of mechanical properties are smaller crystal size controlled by deposition conditions and the alternation in composition by doping that offers numerous possibilities [64].

Widely used modification of TiN with an addition of aluminium is TiAlN protective coating. Comparing to TiN, TiAlN has both better high temperature stability and oxidation resistance [65], higher hardness [66] and better abrasive wear resistance [67]. The structure of $Ti_{1-x}Al_xN$ is the cubic B1 up to 60 at.% of Al (x = 0.6) and hexagonal B4 (wurtzite) above 70 at.% of Al which is the structure of AlN. The hardness continually increases with addition of Al up to 60 at.% of Al due to the solid solution hardening and starts to decrease with higher fraction of B4 structure [63], [64], [68]. Annealing at temperatures higher than 900 °C supports a spinodal decomposition of the solid solu-

tion into coherent TiN and AlN phases that together form a nanocomposite structure. The hardness of the film depends on the grain size and its orientation, in the ideal case the microhardness can reach up to 47 GPa [68] (if the microhardness exceeds 40 GPa the coating can be called superhard). The spinodal decomposition is a consequence of thermodynamically metastable FCC TiAlN solid solution. The oxidation resistance at work temperatures (up to 1000 °C) is enhanced due to a formation of Al_2O_3 on the surface of the coating.

Research in the field of hard protective coatings aims to produce films with improved performance of various characteristics like mechanical properties, wear and temperature resistance, adhesion, friction coefficient etc. This can be obtained by multi-component coatings, multi-layer structures or by adjustment of deposition parameters. The coating materials research continues also with exploration of systems other than nitrides, carbides or oxides. One of the interesting family of high-hardness materials are borides and especially diborides of transition metals that are the subject of this thesis.

2.2. Hard coatings based on borides

Boron based technical ceramics are used in polishing and lapping or as a loose abrasive in cutting applications, ballistic armor, aerospace, military application and other. Magnesium diboride, for example, is a high temperature superconductor with the critical temperature T_c = 39 K [69]. Another significant property of boron and boron based ceramics is the neutron absorption with the application for neutron sensors, shielding and nuclear reaction control. The absorption is a property of ^{10}B isotope with high absorption cross section even for higher energy neutrons. This isotope is naturally present in boron, for example in boron carbide at 19.9 at.%. Thanks to high hardness and high temperature of melting, borides are excellent option as a hard coating or refractory material. On the other hand, preparation of boron based technical ceramics is costly due to difficult densification and low diffusion coefficient, therefore high sintering temperature, pressure and long time are necessary. A drawback of this material group is a high affinity of boron to oxygen what results in oxide impurities on grain boundaries and limits high temperature use of borides in oxidizing atmospheres [70].

The structure of borides can be characterized by the arrangement of boron atoms depending on the ratio between boron and other constituents. In the case of two component borides (we will consider metal borides) with the boron-metal ratio less that one, the structure is composed of isolated boron atoms in interstitial positions that are not bonded with other boron atoms (Mn_4B, Re_3B, Fe_2B etc.) or isolated boron-boron (B-B) pairs distributed within the structure (Ni_3B, Nb_3B_2, V_3B_2 etc.). The B-B chains along one or two crystallographic axes are formed for the ratio 1.0 - 1.3 (FeB, CrB, MoB, V_2B_3 etc.). With increasing boron content, 2D nets are formed within structures with stoichiometries between M_2B_3 and MB_4 where M denotes a metal. Boron atoms form 3D

structures of different complexity within crystal structures with typical stoichiometries MB_4, MB_6, MB_{12} or MB_{66}.

2.3. Transition metal diborides

Specific type of borides are transition metal diborides (TMD) that are represented by high hardness and high melting point compounds what makes them interesting candidates for hard coating application. The diboride structure of a particular importance is the so called AlB_2 or α structure type described as a sequence of alternating metal and boron layers of hexagonal symmetry with AHAH... stacking of close packed metal (A) and boron (H) layers. The metal atoms form a hexagonal unit cell whereas boron forms 2D planar hexagonal network. The boron atoms are situated in the center of trigonal prisms of metal atoms, every metal has 12 boron neighbors, boron atoms have 6 equally distanced metal and 3 boron neighbours. The α structure belongs to the *P6/mmm* space group and is the most common for borides with stoichiometry ranging from M_2B_3 to MB_4. Other boride structures can be derived from the AlB_2 structure by introducing shifted metal layers to positions B and C (in analogy to stacking in HCP or FCC lattice) and puckered boron layers (K, K') [71] what is shown in Figure 2.1.

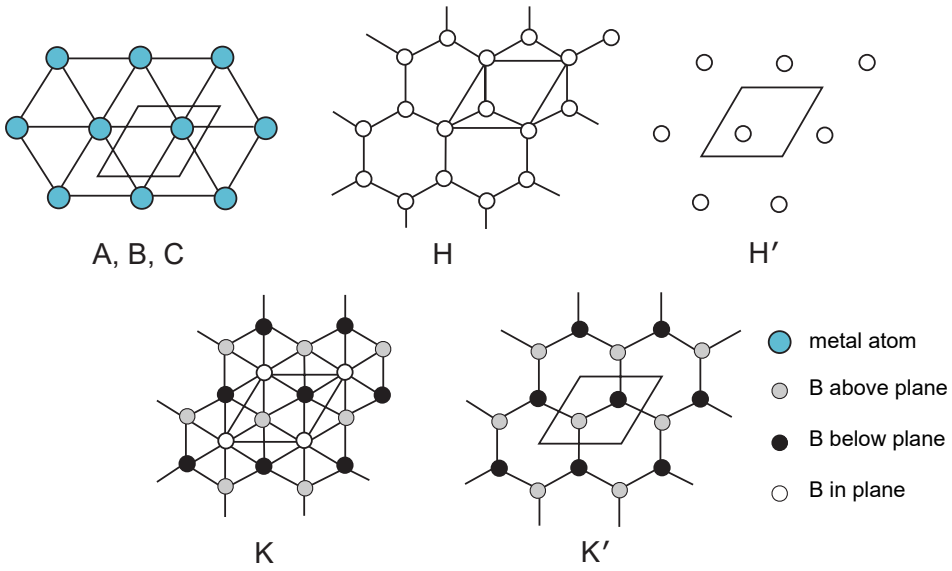

Figure 2.1: Flat planes of metal atoms (big blue circles) and flat boron planes (white small circles) are typical of the α structure. In puckered boron layers black lattice sites are below and grey sites are positioned above the flat plane. All planes that are shown are parallel (0001) type. From [72], modified.

Besides the AlB_2 structure with alternating flat metal layers and boron layers (Figure 2.2a, some TMDs crystallize in structures containing puckered boron layers K' like W_2B_5 structure sometimes denoted as ω shown in Figure 2.2c, stable for tungsten di-

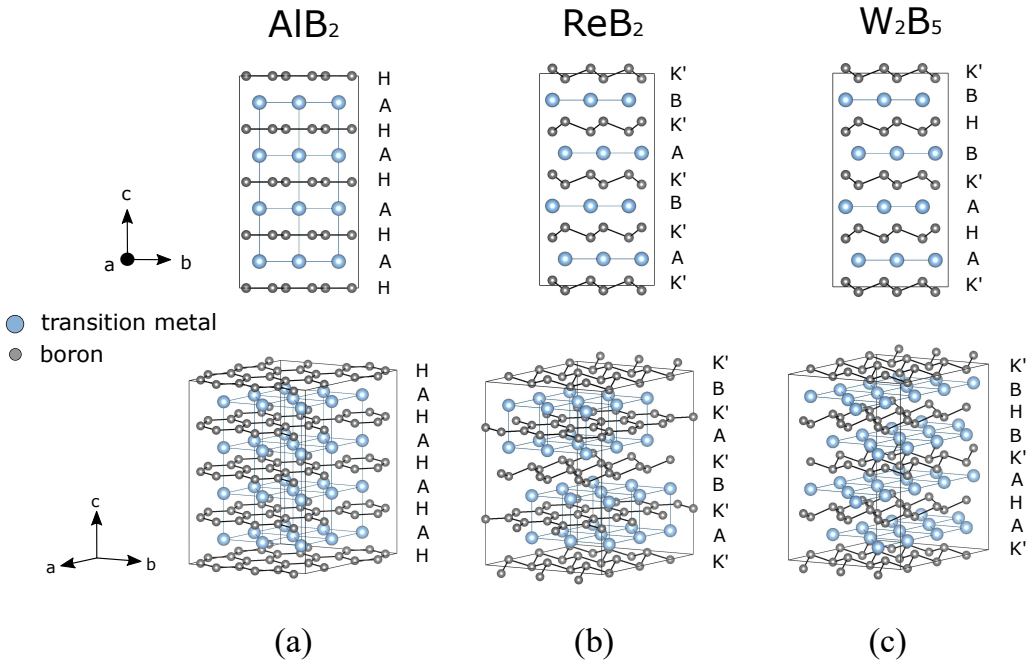

Figure 2.2: The crystal structure and plane stacking of a) AlB_2 (α) structure, b) W_2B_5 (ω) structure and c) ReB_2 structure.

boride. The stacking sequence for the ω structure is AHAK'-BHBK'... with alternation of puckered and flat boron layers belonging to the $P6_3/mmc$ space group. Diborides like ReB_2 or TcB_2 are characterized by the ReB_2 structure with AK'BK'... stacking where only puckered boron layers are present between metal layers Figure 2.2b also from the $P6_3/mmc$ space group [71].

The comparative work on transition metal diborides by Moraes et al. [73] studied the stability of α and ω structures with the use of first principles calculations. The comparison of heat of formation of both crystallographic structures for every TMD is presented in Figure 2.3. The heat of formation equals the amount of energy (enthalpy) that is obtained during the reaction of reacting constituents in the standard state. The lower the heat of formation the more stable the compound is, positive values indicate thermodynamically unstable systems. Figure 2.3 shows that the α structure tends to be more stable for early transition metal diborides whereas the ω structure is more stable for diborides of higher TMs as well as for those with higher atomic number. The stability of diborides of either structure drops linearly as we move along the long row of the periodic table. Higher transition metals crystallize in different structures or do not form diborides at all. On the other hand, older experimental findings say that the α structure is stable for group 4 and 5 TMDs as well as for CrB_2, MoB_2 and MnB_2 [71].

2.3.1. Electronic structure

Mechanical and physical properties of materials are directly dependent on the electronic structure, interactions of constituent atoms and resulting chemical bonding. Within

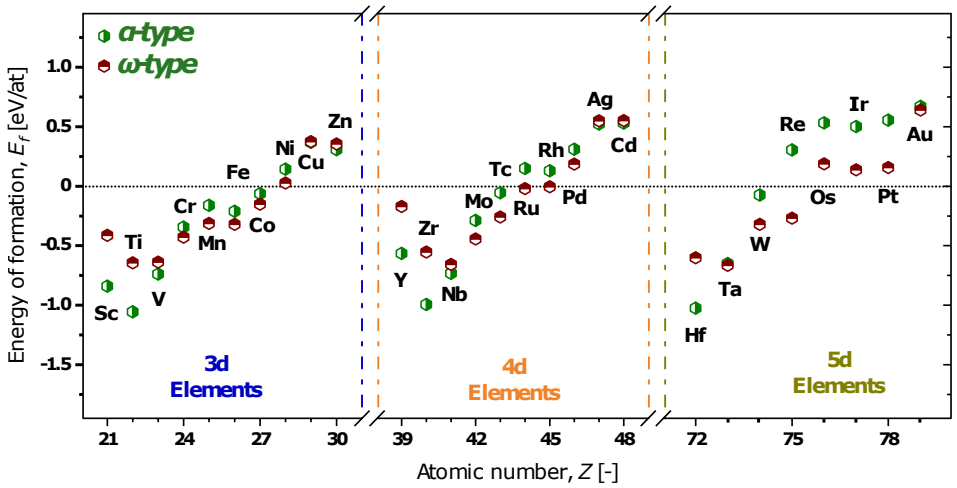

Figure 2.3: Calculated heat (energy) of formation compared between α and ω structure TMDs. Structure lower in energy is more stable. From [73].

binary TMDs three types of bonding are formed, those are boron-boron, metal-boron (TM-B) and metal-metal (TM-TM). Mechanical properties important for hard coating application result from the strong covalent bonding between boron atoms in the layer of hexagons. Thermal and electric conductivity arise mainly due to TM-TM bonding that mediate some amount of metallic bonding. The bond between metal and boron atoms is partially ionic. The combination of covalent, metallic and ionic bondings within transition metal diborides result in complex structural, physical and chemical character of this material group.

The electronic configuration of boron is $2s^2\ 2p^1$ that allows transition towards more stable sp^2 configuration (hybridization of fully occupied s orbital with a single p electron) that is responsible for the graphite like hexagonal structure where each boron atom is bonded covalently to three boron neighbors. B-B bond is the strongest single bond present in TMDs and is therefore considerably affects the hardness of TMDs. The boron sublattice is electron deficient with the $sp^2 + p^x$ electron structure. The empty p orbital has a strong tendency to be occupied by electrons donated by atoms of metal what generates additional π bonding which further increases the strength of this bond. The Hardness of TMDs is therefore to some extend dependent on the donor capability of a transition metal. This property of d metals can be explained by the configurational model of matter [74], [75] that correlates behavior or the material with its tendency to form stable electronic configurations. Stable configurations are characterized by unfilled, half-filled or fully filled orbitals, that means s^2, hybrid sp^3, s^2p^6; d^0, d^5, d^{10}; f^0, f^7, f^{14}. A measure of how close is the configuration of a compound to the nearest stable state is given by the statistical weight of atom with stable configuration (SWASC). In the case of transition metals, their properties depend on statistical weights of d^0 and d^5 states if the occupation of the outermost d orbital n_d is lower than 5 and on statistical weights of d^5 and d^{10} states if $n_d > 5$. A willingness of a metal to donate its electrons to boron sublattice is significant for high SWASC of d^0

when transition metal prefers empty d orbital and d electrons are more delocalized (in a collective state). On the contrary, the donor ability of metal decreases with higher SWASC of d^5 state what is associated with enhanced electron localization. Statistical weight of d^5 state increases with the number of electrons in d orbital i.e. for elements from higher groups and periods. Higher transition metals tend to prefer the half-filled configuration which is reflected by increasing ionization potential towards the middle of the transition metal long row in the periodic table. The strongest electron transfer from a metal to boron occurs in TiB_2 which has the highest hardness among the diborides [74]. Properties of transition metal diborides are mainly determined by hybrid states of boron that depends on the donor ability of metal atoms.

Table 2.1: Temperature of melting T_m, Vickers hardness HV, density ρ, electric resistivity ρ_e (for group 4 and 5 TMDs from [76]), Young modulus E. The last four columns represent a) $SWASC_{TM}$ for d^0, pure transition metals, b) $SWASC_{TM}$ for d^5, pure transition metals, both from [77], c) $SWASC_{TMD}$ d^5, for transition metal in diboride, d) $SWASC_{TMD}$ sp^2+p^x, for boron in diboride, both from [78]. All values without reference are from [79]. Asterisk denotes calculated values.

	T_m [°C]	HV	ρ [$kg.dm^{-3}$]	ρ_e [$\mu\Omega$.cm]	E [GPa]	a) [%]	b) [%]	c) [%]	d) [%]
TiB_2	3225	3370	4.52	9.0 - 26.0	551	57	43	21.2	98.7
ZrB_2	3245	3400	6.09	9.7 - 29.7	506	48	52	24	95
HfB_2	3380	2900	11.19	10.6 - 43.2	500	45	55	26.6	93.7
VB_2	2747	2630[80]	5.07	22.7 - 68.8	577*[80]	37	63	56	87.5
NbB_2	2900	2210[81]	6.97	25.7 - 50.8	637	24	76	64.6	86.2
TaB_2	3200	2500[82]	12.54	32.5 - 75.5	551[80]	19	81	68	83.7
CrB_2	2100	1800	5.20	21	417*[80]	27	73	72	83.7
MoB_2	2230[83]	2560[80]	7.78	45	470[84]	12	88	86	78.2
WB_2	2365[85]	2600[80]	10.77[86]	23 - 92[87]	504[80]	0	96	-	-
MnB_2	1968[88]	1240[89]	5.51[90]	40[91]	559*[90]	-	-	-	-
ReB_2	2400[72]	3070[92]	12.70	40[72]	712[80]	0	94	-	-

The delocalization of metal electrons enhances the TM-B inter-layer bond that has a covalent component due to the formation of the hybrid spd configuration between metal and excess p electrons on boron. This interaction is also partially ionic due to the electron transfer from a metal to boron and it should be stronger in the case of greater charge transfer from metal atoms. Both covalent and ionic bond components should weaken with increasing atomic number and higher SWASC for d^5 associated with smaller charge transfer and consequent localization of electrons on metal atoms.

The weakening of TM-B bond causes an isolation of metal and boron lattices what is reflected by almost five times larger lattice parameter in the c axis of WB_2 (with alternating puckered and flat boron layers) in comparison with TiB_2. On the other hand, an increase of SWASC for half filled configuration as we advance in the periodic table to the right and down supports the TM-TM bond which becomes stronger and its covalent character grows [74].

The diborides of group 4 to 6 transition metals are mostly paramagnetic, ZrB2 is diamagnetic. Diborides of Cr to Ni have complicated ferromagnetic, antiferromagnetic or more complex magnetic structures [71].

2.3.2. Mechanical properties

As mentioned previously, hardness of diborides is governed by the strongest B-B bond which strength depends on the electron transfer from a metal to boron and the extend of $sp^2 + p^x$ hybridization. The bond strength increases with the high statistical weight of $sp^2 + p^x$ configuration of boron and low SWASC for d^5 of a metal. In Table 2.1 there are SWASC values for d^0 and d^5 states calculated for pure metallic compounds. The higher the statistical weight of d^5 the higher localization and lower donor capability. It is apparent that tendency to localize electrons increases with increasing period and group number. The SWASC for d^5 state of a transition metal in diboride (column c) in Table 2.1) has lower values than in the pure metal and the SWASC for $sp^2 + p^x$ configuration has high probability. This describes a strong tendency for boron layer to accommodate larger amount of electrons. We can correlate statistical weight for $sp^2 + p^x$ configuration of boron with hardness well for the group 4 (see Figure 2.4b for hardness) where both decrease from TiB_2 to HfB_2. As we move to the fifth group, we first see decrease in the hardness from VB_2 to NbB_2, however, trend changes as we continue to TaB_2 which is caused by considerable increase of statistical weight of d^5 state of the metal accompanied with localization of d electrons and stronger Ta-Ta or Ta-B interaction overcomes the effect of B-B weakening. On the contrary groups 6 and 7 transition metal dibordes get harder with increasing principal quantum number of valence electrons as the importance of the statistical weight of d^5 states increases and the hardness is affected probably by the consequent increase in strength of TM-TM bonds.

The trend of weaker bonding in group 5 comparing to group 4 is supported by the thermal expansion coefficient that equals 4.5 - 6.3 10^{-6} K^{-1} for TiB_2 - HfB_2, its values for group 5 transition metal diborides is around 7.9 10^{-6} K^{-1} [76] and α = 10.5 10^{-6} K^{-1} for CrB_2 [93]. Larger thermal expansion coefficient reflects easier distortion and elongation of bonds due to increased temperature which can be defined as a consequence of weaker bonding.

The melting temperature T_m is on the other hand dependent on the weaker TM-B and TM-TM bonds. It follows from Figure 2.4a that the melting point of diborides

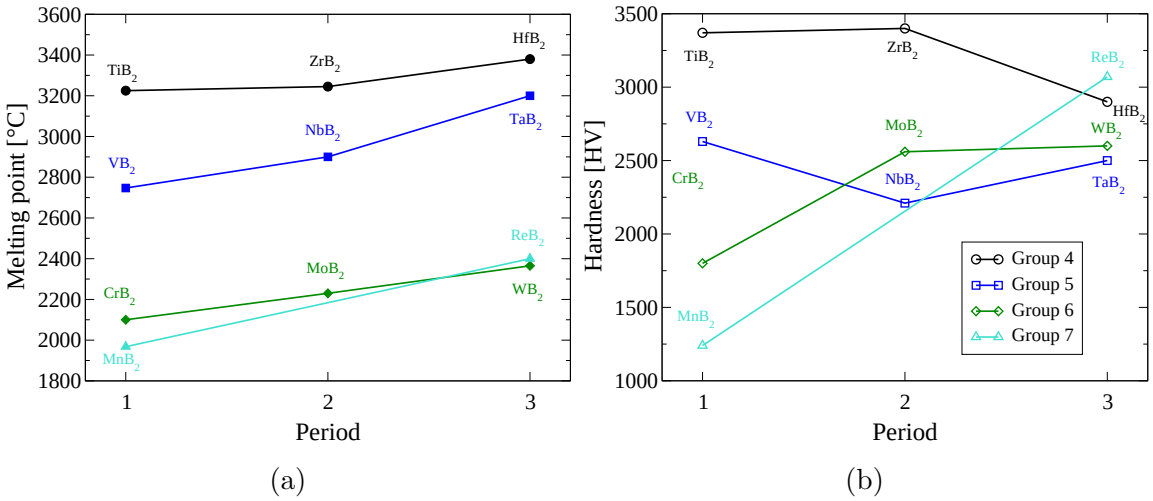

(a) (b)

Figure 2.4: Available melting point a) and the Vickers hardness b) of group 4 to 7 transition metal diborides. Experimental values are collected in Table 2.1 with corresponding sources.

within the same group increases with period. This behavior is due to increasing SWASC for d^5 configuration of a metal and consequent strengthening of metal-metal bonding. As we go from the group 4 to 7 the temperature of melting gradually decreases because of TM-B strength decrease resulting from lower charge transfer to boron.

Not only hardness but also resistance to the cracking is an important requirement for highly loaded hard coatings. In [73] the ductility of diborides was estimated based on the calculated elastic tensors and semi-empirical criteria of the Cauchy pressure (C_{12} - C_{44} elastic constants) called the Pettifor criterion, the Pugh criterion (ductile if G/B $<$ 0.57, G and B are shear and bulk moduli) and the Frantsevich criterion (Poisson ratio more than 0.26). These criteria are summarized in Figure 2.5. Ductility of the α structure diborides increases with TM from higher groups where the electron donation to boron is weaker and electrons stick to orbitals of metal. However, all α diborides in the ductile section are unstable in this structure. The situation with the ω structure is not so straightforward, for example ZrB_2 is predicted to be the most ductile and ReB_2 the most brittle even though the latter should comprise the most electrons in orbitals of metal atoms among group 4 - 7 TMDs. The stable ω structure diborides are on the boundary between ductile and brittle behavior.

An increase of hardness but also fracture toughness and thermal stability of transition metal diborides can be obtained by doping. Resulting ternary transition metal diborides like $(WTa)B_2$ [94], [95] or $(TiW)B_2$ [96] are potential materials for high performance protective coatings.

2.3.3. Transport properties

All transition metal diborides are electric conductors with excellent thermal properties thanks to the metal bonding contribution. The electrical resistivity is influenced by the

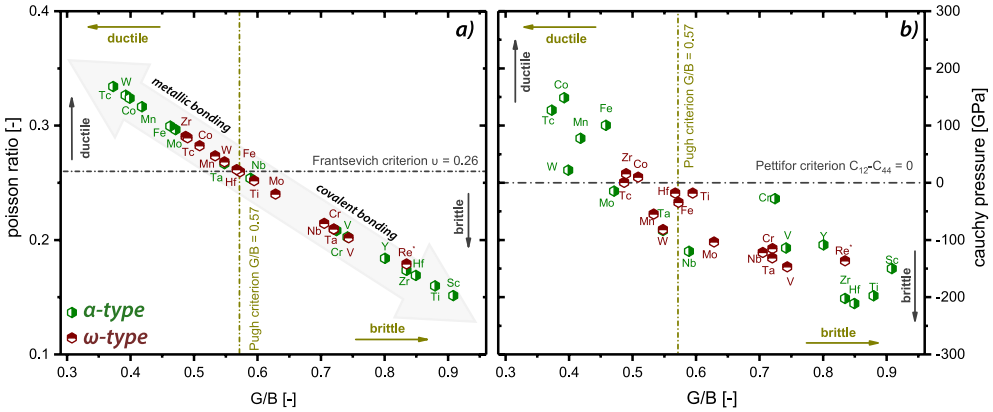

Figure 2.5: Prediction of ductility of α and ω structure TMDs. From [73].

density of carriers and their mobility. Electrons from stable configurations d^5 and d^{10} are not involved in charge transfer due to their strong localization. Electrical conduction is possible thanks to the delocalized d electrons with intermediate configurations $d^{k/5+k}$ where k = 1 to 4 or thanks to s or sp valence electrons. The density of free elctrons responsible for the conductivity is characterized by DOS near the Fermi level and influenced by the degree of localization. The charge mobility is determined by the mean free path of electrons (depends on an intensity of lattice vibrations) expressed by the scattering time and the effective mass of an electron. High mobility of carriers is characteristic for the group 4 diborides along with a low carrier density. For higher group diborides the conduction band is more filled what increases the carrier density and lowers the mobility. Lower mobility of charge carriers is a sign of lower rigidity of the lattice. The fourth group TMDs have lower resistivities (Table 2.1) and thermal expansion coefficients [76].

Group 4 transition metals have high capability of electron donation that are transferred to boron atoms which then form rigid B-B bond. A consequence of this behavior is low density of carriers with high mobility and low resistivity. Diborides formed by higher groups transition metals have weaker B-B bond because of lower donor capability of TM (SWASC for d^5 increases) which is accompanied with higher intensity of lattice vibration and consequent reduction of electron mobility due to additional scattering.

Resistivity of TMDs has a linear dependence on temperature. At higher temperatures, resistivity increases because of carrier scattering of the lattice thermal vibrations and the electron-electron scattering within the d band. As the temperature is raised, electrons are redistributed in the conduction band what results in lowered DOS at the Fermi level, an increase in the statistical weight for d^5 configuration and lesser carrier scattering in the TM-TM band. The governing factor in the temperature dependence of the resistivity is the DOS at the Fermi level rather than the scattering by thermal vibrations. The decrease of the temperature coefficient of the resistivity (resistance change factor per degree of temperature) for higher group TMDs is a result of higher DOS at the Fermi level of these compounds [76].

2.4. Ni_2MnGa

Ni_2MnGa is one of the most studied materials exhibiting magnetic field induced strain and related effects. In this section basic properties and the most important characteristics of this alloy are described.

2.4.1. Structural properties

Ni_2MnGa belongs to the group of Heusler alloys named after Friedrich Heusler, who reported the fabrication of ferromagnetic alloy by alloying constituents neither of which is ferromagnetic [97]. Alloys in this group are defined as ternary intermetallic compounds characterized by strong relationship between the chemical order, composition and magnetic properties. Typical of Heusler alloys is the cubic $L2_1$ crystal structure of $Fm\bar{3}m$ space group and the stoichiometric composition X_2YZ where X and Y are transition metals whereas Z is typically an element from group 13 to 15. The $L2_1$ structure shown in Figure 2.6 is constructed by four overlapping FCC sublattices two of which are occupied by the X element and the other two by Y and Z elements. Sublattices originate at (0, 0, 0), (1/4, 1/4, 1/4), (1/2, 1/2, 1/2) and (3/4, 3/4, 3/4) in the conventional unit cell [98]. If all four sublattices are occupied, an alloy is called the full-Heusler however, structure with one vacant sublattice is called the half-Heusler alloy with the composition XYZ and corresponding $C1_b$ lattice.

Ni_2MnGa solidifies from melt into the A2 structure at around 1100 °C. Atoms in the A2 structure are completely disordered therefore it has BCC symmetry. Upon cooling, the $L2_1$ structure is formed directly from A2 or through the partially ordered intermediate B2 structure. Within the B2 lattice, one sublattice is occupied by Ni atoms and the second one by randomly distributed Mn and Ga atoms. We can look at the B2 lattice of Ni_2MnGa as the $L2_1$ structure with two sublattices filled with Ni atoms and two other sublatties are occupied with randomly distributed Mn and Ga atoms. Below the ordering temperature of 750-800 °C the long range ordered $L2_1$ structure is stable. High cooling rates can result in quenched alloys with residual disorder of Mn and Ga atoms what has significant impact on properties especially the magnetic properties. Usually annealing is necessary to allow for diffusion of Mn and Ga atoms in order to obtain ordered structures [99]–[101].

2.4.2. Phase transformations

Of great importance for its properties and application is the ferromagnetism of Ni-Mn-Ga alloys. Usually stated net magnetic moment is 4.17 μ_B per formula unit at 4.2 K reported by Webster et al. [102] however lower [103]–[105] as well as higher values (more that 4.5 μ_B) [106], [107] have been reported. Relatively large range of measured magnetic moments is caused by the disorder between Ga and Mn sublattices,

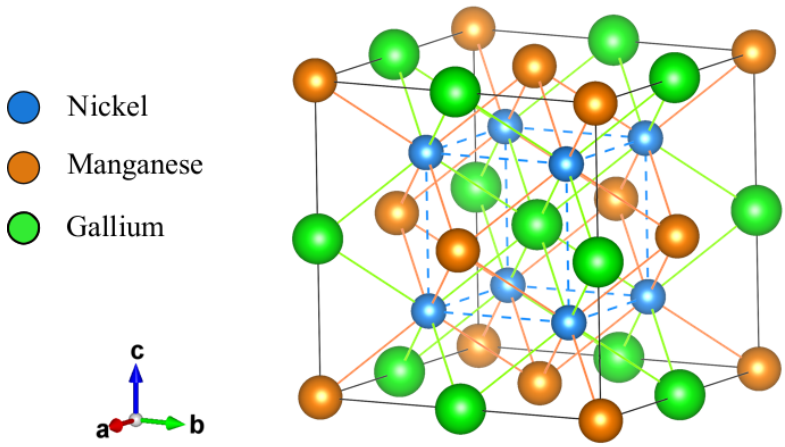

Figure 2.6: Cubic $L2_1$ structure of Ni_2MnGa austenite.

by the sample preparation or due to departure from the stoichiometric composition. Manganese is the main contributor to the net magnetic moment but Mn atoms on the Ga sublattice are ordered antiferromagnetically to those on the Mn sublattice [108] what greatly decreases the net magnetization even for low excess of Mn. The magnetic moment of Ni is less than 0.3 μ_B and Ga exhibits negligible magnetic moment [102]. The Curie temperature of the magnetic transformation for the stoichiometric Ni_2MnGa is $T_C = 376$ K [102]. The picture of the magnetic structure is a complicated one with the majority of magnetization on Mn sites due to the exclusion of minority-spin (spin down) electrons from the Mn $3d$ shell above the Fermi level. The ferromagnetic exchange responsible for the stability of the magnetic ordering between Mn atoms cannot be direct because of large distances between Mn lattice sites. Instead the exchange interaction between Mn d localized orbitals are mediated by interaction with conduction Ni d and Ga p electrons described by the Ruderman-Kittel-Kasuya-Yosida (RKKY) theory of exchange interaction mediated by free electrons [109], [110].

The high temperature cubic austenite with $L2_1$ structure undergoes a first order martensitic phase transition at temperature around $T_M = 200$ K [102]. There have been found several martensitic structures in the Ni-Mn-Ga alloys - non-modulated tetragonal martensite (NM) with tetragonality $c/a \approx 1.2$, tetragonal five-layered (10M or 5M) with $c/a \approx 0.94$ or monoclinic seven-layered (14M or 7M) with $a > b > c$ and $c/a \approx 0.89$ [112], [113]. The lattice of 10M martensite is shuffled along the (110) $[1\bar{1}0]$ system with shuffling period of five whereas the 14M martensite is shuffled along the same crystallographic system with a period of seven. The fourth theoretically predicted structure of the martensite is the orthorhombic 4O structure [111]. Martensite variants are depicted in Figure 2.7. Before the martensitic transformation Ni_2MnGa undergoes a transformation to premartensite at $T_{PM} = 261$ K [114] that keeps cubic symmetry but exhibits 3 fold modulation therefore is called 6M. Different theories have been postulated to explain martensitic transformation like the Jahn-Teller distortion [103], [115], phonon

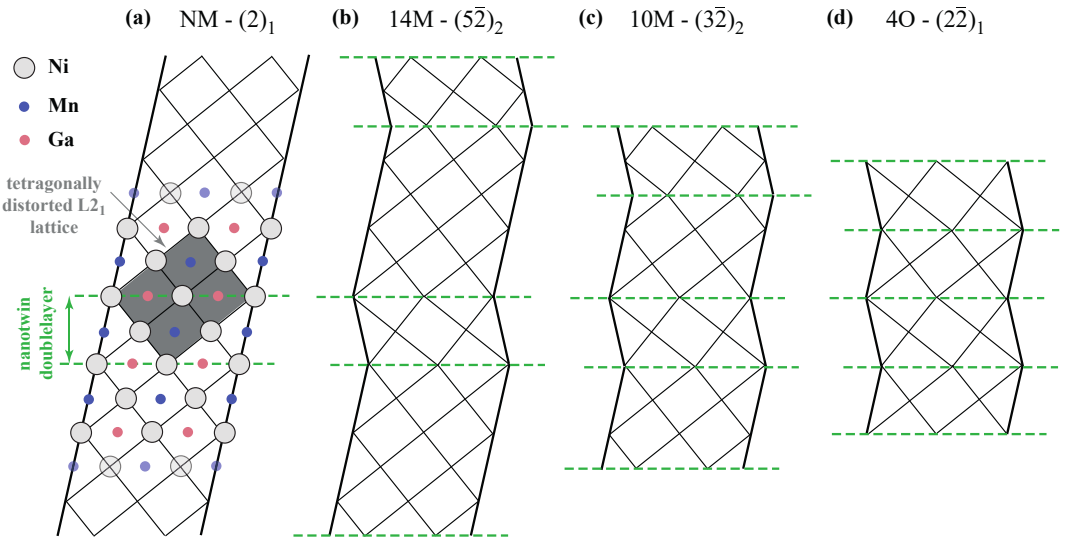

Figure 2.7: Schematic representation of martensite structures in Ni_2MnGa. From [111].

softening [116], [117], Fermi surface nesting [117]–[119] or electron-phonon coupling. The Jahn-Teller distortion in the crystal field of a lattice breaks the degeneracy of *d* orbitals near the Fermi level and the subsequent redistribution of charge lowers the total energy [103]. Phase transformations are also explained by the softening of the TA_2 phonon mode along the [110] direction that arise around T_{PM} [118] and is accompanied by softening of the shear elastic constant $c' = \frac{1}{2}(c_{11} - c_{12})$. This phonon anomaly, also known as the Kohn anomaly, is closely related to the topology of the Fermi surface through the nesting vector that is identical with the vector of the phonon softening. There is a strong coupling between electrons and phonons at the nesting vector leading to a strong screening response from electrons due to atomic displacements at this wave vector. The nesting vector matches the modulation of premartensite and martensite phases in Ni_2MnGa [119]. There however are structures where neither Jahn-Teller nor Fermi surface nesting was observed in the martensite therefore electron-phonon coupling is presumably the leading factor for austenite structure instability [119], [120].

2.4.3. Magnetic shape memory effect

The property of Ni-Mn-Ga alloys that brings them the most attention is the magnetic shape memory (MSM) effect [121]. The deformation occurs if an external field is applied, though it is not negligible only in single crystal samples. For example, there was observed a magnetic field induced strain (MFIS) in 10M and 14M single crystals up to 6% [122] and 10% [123] respectively. Characteristic of the martensite phase is a twinned structure with highly mobile twin boundaries. MSM effect can be caused by two phenomena - magnetically induced reorientation (MIR) that includes the twin boundary motion, and magnetically induced transformation between the austenite and the martensite. Ni-Mn-Ga alloys exhibit large MSM effect based on MIR for which the existence of martensitic transformation, a martensite with twinned structure and

a high magnetic anisotropy i.e. a strong connection between the magnetization vector and a preferential crystallographic direction or plane are crucial. The applied magnetic field gradually rotates the magnetization vector to the direction parallel to the external magnetic field. When the energy of the rotation surpasses the energy required for the MIR, the microstructure changes by nucleation and growth of those twin variants that posses the smallest angle between their easy magnetization axis and the direction of the applied field. In modulated martensite the easy axis is parallel with the c axis and since the unit cell of martensite is not uniform in all directions ($c/a < 1$ in modulated martensite) the growth of more favorable twin variants up to the magnetic saturation is accompanied with a macroscopic change of sample's shape. This reorientation is permanent unless a restoring force acts on the material. The magnetization process is strongly dependent on the orientation of the field and shows hysteresis. MSM materials are applicable as actuator, vibration damping, various sensors, cooling systems (application of magnetocaloric effect) or, theoretically, as a source of electricity [101].

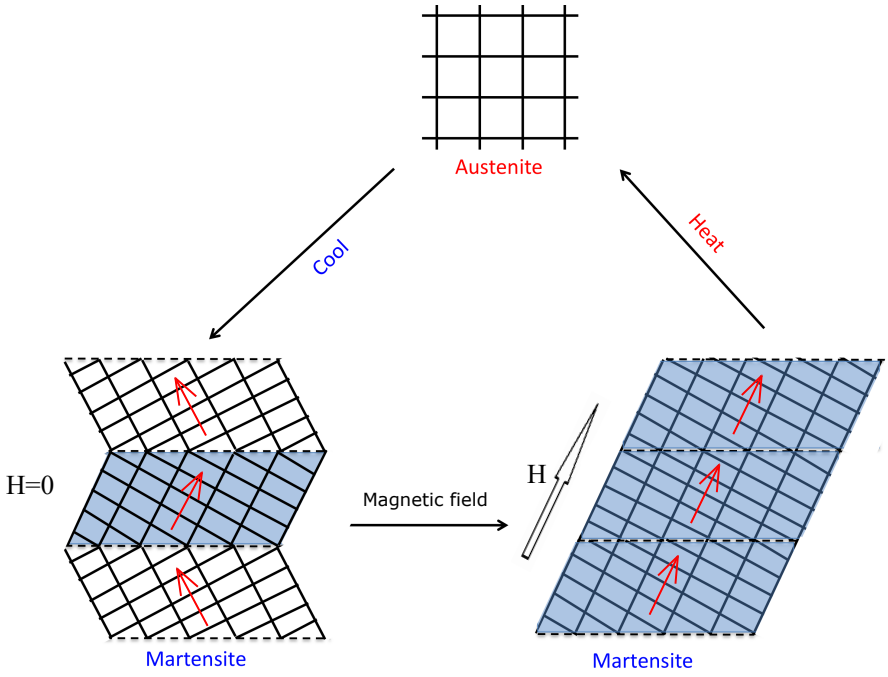

Figure 2.8: Principle of MSM effect. After martensitic transformation there are multiple twin variants, red arrows show magnetic moment direction in twin variants (lower left corner). When sufficiently large magnetic field is applied MIR occurs and magnetic moments become aligned with the magnetic field what is accompanied by distortion (lower right corner). The thermal shape memory effect occurs after heating back to austenitic structure. After [124], modified.

After the martensitic transformation the structure consists of several twin variants. A single twin variant can be forced by applied constraints during the martensitic transformation like compressive stress or magnetic field. For the 10M and NM martensite

there are three twin variants with different c-axis orientation and four different twin planes {101} in each variant, for 14M there are six twin variants. For MSM the existence of mobile twin boundaries is required. The mobility is quantified by the twinning stress parameter obtained form the stress-strain measurements. This is a stress needed for the movement or nucleation of twin boundaries and its typical value for Ni-Mn-Ga alloys is less than 3MPa [101].

The martensitic phase transformaton is thermoelastic thus Ni-Mn-Ga alloys also display the thermal shape memory effect and superelasticity. Magnetocaloric effect is a phenomenon characteristic to magnetic materials that heat up during the magnetization due to spin alignment. Ni-Mn-Ga alloys on the other hand exhibit inverse magnetocaloric effect when the temperature of material decreases in applied magnetic field. This is caused by magnetically induced transformation from martensite to austenite. Absorbed latent heat of transformation exceeds heating due to magnetic ordering. Magnetocaloric effect offers environmentally friendly refrigeration capable of cooling down to cryogenic temperatures below 1 K [125].

The work temperature of Ni-Mn-Ga based alloys is restricted by T_M and T_C. To produce a significant MIR effect, the material has to operate in temperature range of ferromagnetic martensitic structure. Especially T_M of the stoichiometric alloy is way below the room temperature. Research is therefore focused on increase of both transformation temperatures. One of the ways to improve characteristics of the Ni_2MnGa is the stoichiometry adjustment by changing the concentration ratio of the three basic constituents. For example the martensitic transformation temperature increases with increasing content of Ni up to 330 K for 55 at.% of Ni, however, T_C is not affected by this modification. Positive effect on T_M has substitution of Ga by Mn and replacement of Ni with Ga, both lower T_M. The Curie temperature increases when Ni atoms are replaced by Mn [101].

Second option how to move transformation temperatures towards higher values and possibly to enhance physical properties is doping. For example, simultaneous doping by Cu and Co results in increase in both transformation temperatures above the room temperature (T_M = 330 K, T_C = 393 K) as well as in the increase of MFIS up to 12%, caused by lowering the twinning stress [126]. Furthermore, doping on the Ga-sublattice with Cu concentration of 5 at.% increases T_M up to 500 K, but decreases T_C to around 300 K [127]. Doping with Fe increases T_C but decreases T_M [101].

As mentioned in the subsection 1.3.4 about the Hubbard +U correction, *d* or *f* electrons tend to be over-delocalized by planewave based *ab-initio* codes. Since all constituents of Ni_2MnGa contain electrons in *d* orbital and Mn atoms exhibit high magnetic moment due to localized *d* electrons, the employment of DFT+ U functional for this system seems natural. There are some reports of calculations with +U correction on Mn atoms. Value of the U parameter for Mn calculated in ref. [110] using the linear response approach is 5.97 eV what seems to be an exaggerated for partially metallic system. The use of the Hubbard correction increases magnetic moment on Mn sites

which results from more localized *d* electrons of manganese. This behavior results from stronger exchange splitting of spin up and down states which is visible in DOS plots. Importantly, large U on Mn leads to destabilization of NM martensite energy minimum on the tetragonal deformation path. This is due to weakening of exchange interaction of Mn atoms since the energy magnetic interactions in simple GGA stabilizes the NM martensite. This weakening is caused by stronger Coulomb repulsion in the case of DFT+ U.

The U parameter in ref. [128] was determined semi-emprically as a fit to experimental bulk modulus. The values obtained in this work are 3.93 eV on Mn and 0eV on Ni. This value is sufficiently low to keep the NM martensite minimum even though it is metastable. DFT+ U approach was recently applied to the prediction of elastic constants [129] and magnetocrystalline anisotropy [130] of Co and Cu doped Ni-Mn-Ga alloys using U = 1.8 eV on Mn.

3. Results

3.1. Computational details

The results were obtained using the density functional theory on the basis of the projected-augmented wave potentials (PAW) [43] and the plane wave basis set as implemented in the Vienna *Ab-initio* Simulation Package (VASP) [131], [132]. The exchange-correlation term was approximated using the Perdew-Burke-Ernzerhof (PBE) approximation [29]. The first Brillouin zone (BZ) was sampled by the gamma-centered Monkhorst-Pack grid of 968 to 1560 k-points distributed on an automatically generated mesh in the case of transition metal diborides. Unit cells of TMDs were described by supercells of 24 atoms, that is 2 x 2 x 2 primitive unit cells. An anisotropic k-mesh generated for DFT+ U calculations of Ni_2MnGa consisted of $15 \times 15 \times 11$ k-points since we used tetragonal computational cell containing eight atoms. Both k-meshes were tested for convergence. The Gaussian smearing method for integration over the BZ was used with a 0.1 eV smearing width for diborides and the terahedron method with Blöchl corrections was applied to Ni_2MnGa. The electronic orbitals were expanded in a plane wave basis set with a cut-off energy of 600 eV for diborides and 500 eV Ni_2MnGa. Valence electrons used for TMDs were $2s$ $2p$ for boron, transition metals were calculated with semi-core states (n-1)p, ns, (n-1)d with exception of Zr where only ns and (n-1)d states were used, n denotes the principal quantum number or period in which TM resides. Valence electrons for Ni_2MnGa were set to Ni $3p^6$ $3d^9$ $4s^1$, Mn $3p^6$ $3d^6$ $4s^1$ and Ga $3d^{10}$ $4s^2$ $4p^1$. The total energy convergence criterion was 10^{-5} eV per unit cell for all calculations. All computational cells were relaxed with 10^{-4} eV break condition for the ionic relaxation loop.

The DFT+ U calculations were performed within the Dudarev's approach [37] with the effective U applied on Ni and Mn since localized d electrons play an important role in the structural and magnetic properties of Ni-Mn-Ga alloys. In previous works on Ni_2MnGa, the U parameter on Mn was set to 5.97 eV and 3.93 eV, calculated with the use of linear response approach [110] and a semiempirical adjustment to elastic constants [128], respectively. In works on doped Ni-Mn-Ga alloys concerning elastic constants and magnetocrystalline anisotropy was U = 1.8 eV applied to Mn d orbitals to fit experimental c/a ratio in tetragonally distorted lattice [129], [130]. In the present work, we use U in the range of $1-5$ eV separately on Ni, Mn, and using the same value of U on both Ni and Mn simultaneously.

Bond analysis was performed with the use of LOBSTER-4.0.0 package. Wave functions expressed in terms of plane waves were projected onto localized functions using the pbeVaspFit2015 basis set. Gaussian smearing was set to 0.15 eV.

3.2. Characteristic examples of chemical bonding

Chemical bonding in molecules and solids is intuitively divided into three main categories - ionic, covalent and metallic bonding. The character of bonds in real materials is usually a combination of these bonding types. TMDs are specific structures since all three types of bonding can be found within them. As a first step, we briefly characterize three typical bonding types in terms of DOS, COHP, COOP, DOE as well as charge density distribution.

3.2.1. Ionic bonding

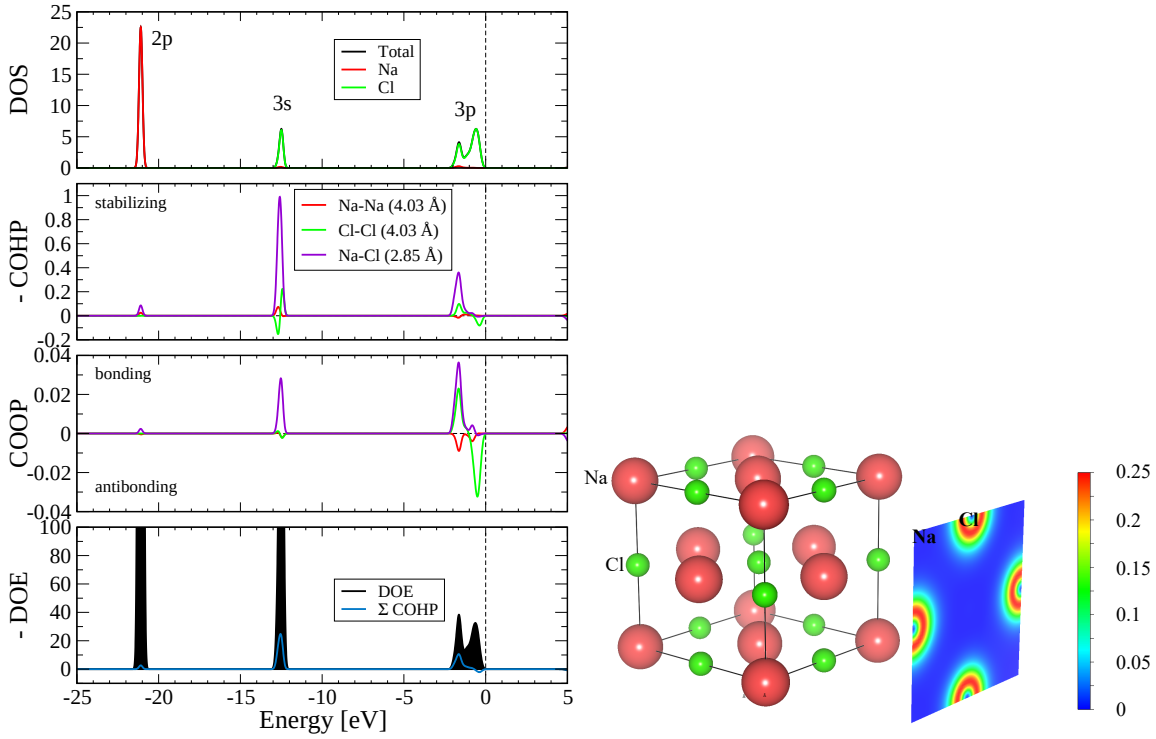

(a) (b)

Figure 3.1: a) The ionic bonding analysis, b) unit cell and charge density plot of NaCl. DOE is compared with COHP summed over all nearest and second nearest neighbours. Negative COHP and DOE curves are plotted to match COOP bonding and antibonding interactions with sign.

The ionic bonding occurs in structures where constituent atoms differ in electronegativity. The higher the electronegativity difference the stronger ionic bond is formed. Electrons of the less electronegative element are attracted by the element with high electron affinity and fill its atomic orbitals in order to obtain more stable electronic configuration. This way the structure is composed of ions of opposite charge what causes a electrostatic Coulomb attraction of the nearest neighbours. The electrostatic

attraction is the most important contribution to the binding energy of ionic compounds and is denoted as the Madelung energy that depends on the Madelung constant, which comprises the geometry of the lattice. Since the Coulomb interaction is of a long range, the Madelung constant has to consider pair interactions of all constituent ions in a crystal. Ionic bonding is typical only for solids.

A common representative example of the ionic bonding is NaCl with 0.94 fractional ionic character [10]. The charge distribution in Figure 3.1b is spherical around ions with transition of Na $3s$ electron to Cl $3p$ orbital what results in both ions having stable electronic configuration of the nearest noble gas. DOS in Figure 3.1a is composed of separate peaks what indicates localization of electrons with almost no overlap between orbitals. DOS at the Fermi level (E_{F}), marked by the dashed line, is zero and the presence of the nearest unoccupied orbital is more than 5 eV above E_{F} which confirms that NaCl is an insulator. It is difficult to study ionic bonds in terms of orbital overlap since in theory there is none between interacting atoms. The stabilizing contribution to the band energy due to Na-Cl interaction and very small portion of Na-Na stabilizing interaction at -12.5 eV can be distinguished by the negative COHP (-COHP is plotted to match COOP bonding states therefore negative COHP corresponds to plotted positive values in all grphs). Cl-Cl interactions have symmetric bonding and antibonding contribution therefore do not affect the energy of the system in the selected energy range. Analysis of the orbital overlap (COOP) indicates some localized bond formation between Na and Cl. On-site interactions of lower energy orbitals seem to have crucial effect on the stability of structures as DOE shows (generalized COHP with all off-site and on-site interactions included). The fact that DOE is negative in the whole range suggests that electrons localized on atoms do not increase the total energy of the system what agrees with the localized nature of the ionic bond.

3.2.2. Covalent bonding

Non-metallic single component materials or combination of elements with alike electronegativity typically form covalent bonds. The idea of covalent bond is based on valence electrons shared by bonded atoms forming electron pairs. As atoms approach each other and their atomic orbitals overlap, the molecular orbital is formed with equal number of electrons from each atom in the way that alignment of electrons' spins in the molecular orbital is antiparallel. Two new molecular orbitals are produced - stabilizing or bonding orbital in the case of overlap of electron wave functions with the same sign (molecular orbital energy is lower than the atomic orbital energy) and destabilizing or antibonding orbital with higher energy. In the case of solids with plenty of bonded atoms, molecular orbitals become bands that together define the band structure of a crystal. The covalent bond, opposite to ionic or metallic bonding, is strongly directional which leads to open structures like diamond.

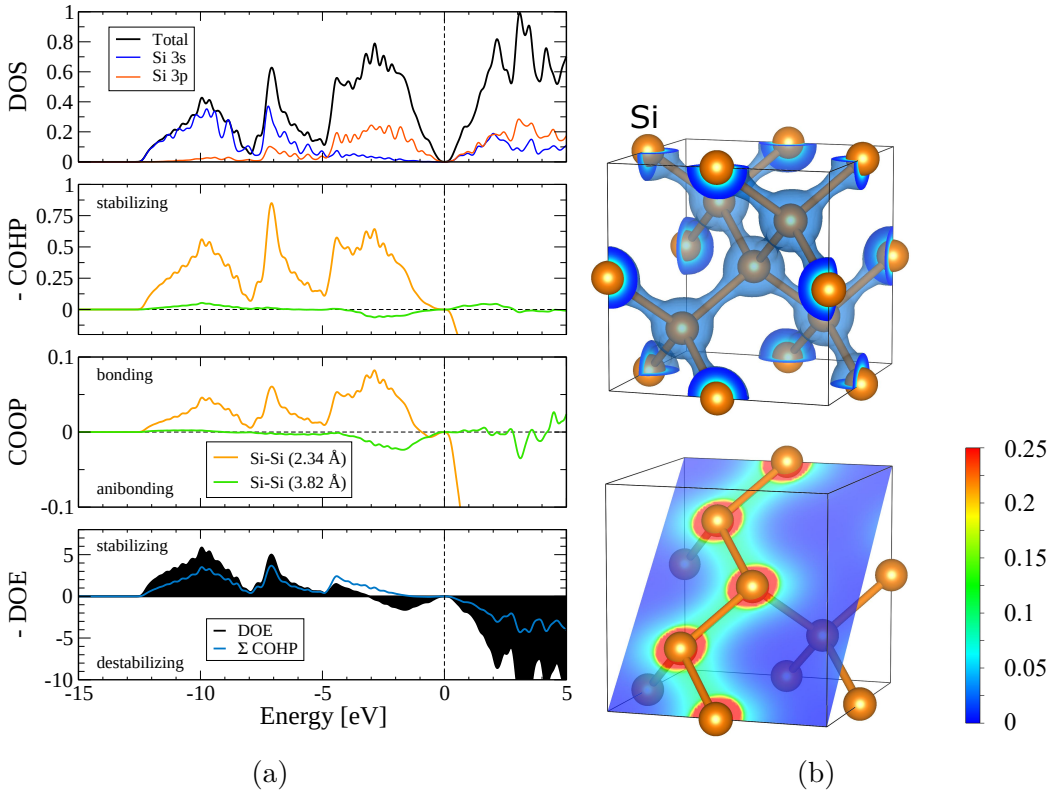

(a) (b)

Figure 3.2: a) Bond analysis of typical covalent bonding in Si and b) charge density maps in the unit cell.

In Figure 3.2 we present the bonding analysis of silicon with the diamond structure. We can see that the charge distribution is non-zero in between Si atoms what is a sign of evenly shared electrons (Figure 3.2b). In comparison to the ionic bonding DOS exhibits wider, not strictly separated orbital peaks that are, however, still well distinguishable. The overlap of 3s and 3p orbitals results in sp^3 hybridization responsible for tetrahedral configuration of Si atoms. COHP and COOP also show wide overlapping peaks of hybridized orbitals between nearest neighbours atoms bonded by the sigma bond. All interactions forming the shortest bond are bonding below the Fermi level what supports the stability of the structure. Values of COOP for Si are higher than in the case of ionic bonding what is an indication of the large orbital overlap.

3.2.3. Metallic bonding

In metallic bonding electrons participating on interactions are shared between all atoms of the crystal. These electrons are not localized between bonded atoms as in the covalent bonding but they exist in free-like collective state. Electrons that can move within the crystal are called conduction electrons and mediate attractive interaction with cations at crystal lattice sites. The delocalization of valence electrons over large space (within a crystal) leads to a lowering of their kinetic energy. Because of the non-local character of this bond, metals crystallize in close packed structures without any directionality.

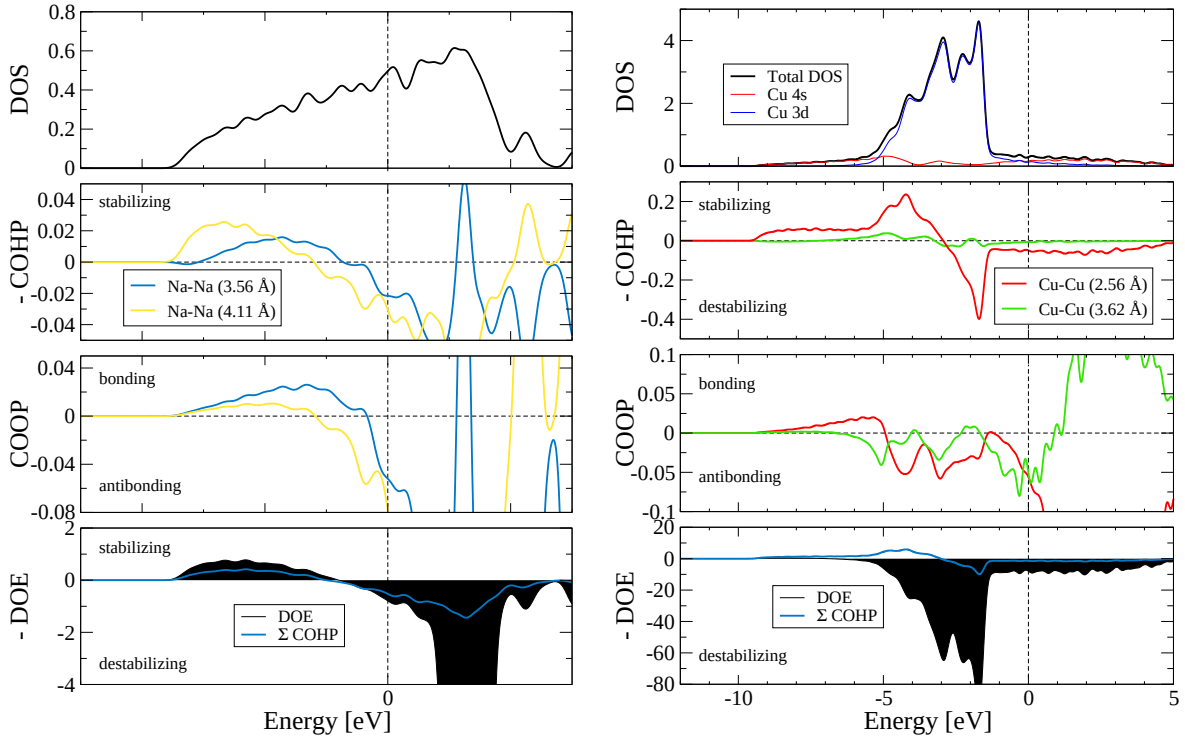

Figure 3.3: Metallic bonding in a) sodium and b) copper.

Transition metals are bonded by a combination of conduction electrons and covalently bonded inner shell electrons what makes bonds stronger what makes these metals harder [10].

Figure 3.3a shows bcc sodium with continuous exponential like growth of DOS towards E_F that is typical of the free electron gas. Finite DOS at E_F correctly identifies Na as a conductor. COHP and COOP are broad with overlapping states in the whole range of occupied energies typical for the metallic character. Interactions become antibonding close to E_F which is a sign of instability and possibly related to low temperature of melting and poor mechanical properties. DOE shows stabilizing contribution from both inter-atomic and on-site interactions since it is negative at almost all energies.

Transition metal representative Cu has broad metallic DOS though less uniform as in the case of Na. COHP contains large destabilizing peak just below E_F. The stability of this system would be higher with lower number of electrons, that is why metals with lower atomic numbers have higher temperatures of melting (with exception of Mn). Negative DOE below E_F indicates that on-site electron interactions introduce negative contributions to the band energy. On-site interactions are typically much more important to the band energy that inter atomic interactions. However, the integral of DOE up to E_F, in other words the band energy, is negative mostly thanks to on-site interactions of the lower lying core electrons.

3.3. Transition metal diborides

For the sake of comparison all TMDs studied within this thesis were assumed in the α (AlB_2) structure where all boron layers are flat (Figure 2.2a and Figure 3.4b). In Figure 3.4 is shown a part of the periodic table with transition metals whose diborides are studied in this thesis. Electron configuration of transition metals and the stable structure of their diborides calculated in ref. [73] and known from experimental data according to ref. [71] are stated as well. The α structure is preferred in diborides of early transition metals.

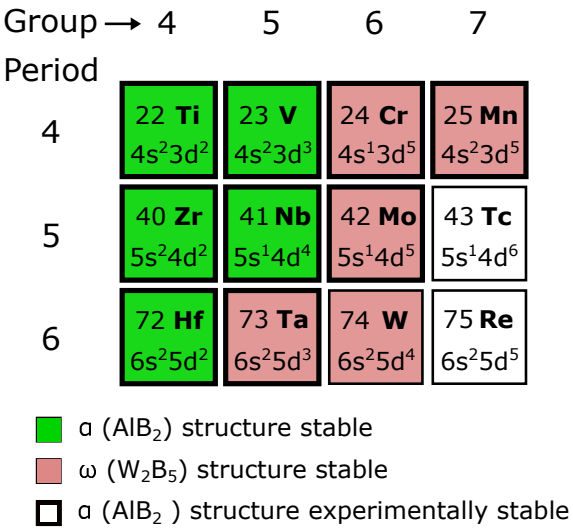

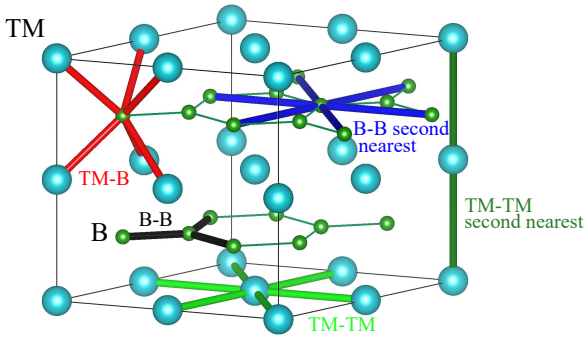

(a) (b)

Figure 3.4: a) Transition metals of groups 4 to 7 with the electron configuration. Green color is used for TMs that form diborides with stable α structure and pink color is used for ω structure according to the heat of formation calculation [73], thick line windows represent TM whose diboride has the α structure according to experimental data in [71]. Tc and Re are left blank since their diborides crystalize in ReB_2 structure, b) interactions being subject to the bond analysis marked in the α structure unit cell.

Computed lattice parameters, unit cell volumes and the fraction of ionic bonding based on the difference of Pauling electronegativity are compared in Table 3.1. The unit cell volume decreases within each period, however, its trend within groups changes. In group 4 and 5 the largest volume have period 5 TMDs (ZrB_2 and NbB_2) but within groups 6 and 7 the volume increases with increasing period of TM as expected. Very similar is the trend of c/a. The elongation of the crystal structure in the direction of c axis is present within all groups as we proceed from the top of the periodic table to the bottom with the exception of HfB_2 and TaB_2. We can assume that the strength of the TM-B inter-layer bond increases markedly in HfB_2 and TaB_2. This TM-B bond

strengthening might be caused by the increased ionic contribution or by redistribution of charge on B atoms in favor of TM-B bond. The increasing c/a in periods 5 and 6 between groups 5 to 7 TMDs points towards TM-B weakening peaking with TcB_2 and ReB_2. The lattice parameter a, affected mainly by B-B in plane bonds, increases within groups and decreases within periods as we proceed from top to bottom and left to right within the periodic table. We can assign that to B-B weakening within groups and strengthening within periods.

Table 3.1: Calculated lattice constants, unit cell volume and corresponding c/a ratio as well as fraction of ionic bond based on the difference of the Pauling electronegativity in Pauling units χ_r of 4-7 group transition metal diborides with AlB_2 structure.

Group		a [Å]	c [Å]	V [$Å^3$]	c/a [-]	Ionicity [χ_r]
	TiB_2	3.03	3.23	25.73	1.07	6.1
4	ZrB_2	3.17	3.56	31.06	1.12	11.8
	HfB_2	3.15	3.49	29.89	1.11	12.8
	VB_2	3.00	3.03	23.62	1.01	4.1
5	NbB_2	3.11	3.32	27.84	1.07	4.7
	TaB_2	3.10	3.33	27.75	1.07	7.0
	CrB_2	2.96	3.03	23.05	1.03	3.6
6	MoB_2	3.03	3.34	26.62	1.10	0.4
	WB_2	3.02	3.38	26.74	1.12	2.5
	MnB_2	2.97	2.92	22.27	0.99	5.8
7	TcB_2	2.96	3.40	25.89	1.15	0.5
	ReB_2	2.95	3.49	26.38	1.18	0.5

In Figure 3.5 are summarized DOS plots of all studied TMDs obtained thanks to LOBSTER package. This method is convenient for very precise local density of states (LDOS) plots that are in VASP evaluated only within defined Wigner-Seitz atomic radius. On the other hand, LOBSTER calculates DOS from the projected local basis set and LDOS comprises information about the interstitial space as well. DOS of different diborides in Figure 3.5 resemble each other well and the often used rigid band model, in which different materials are represented by shifted position of E_F on the same DOS plot based on the number of electrons, can be justified for TMDs. The common characteristics is the opening of the pseudogap resulting from the hybridization of B p and TM d orbitals what creates new energy states with lower energy separated from the rest of TM d states by the pseudogap [133]. This is supported by the overlaying

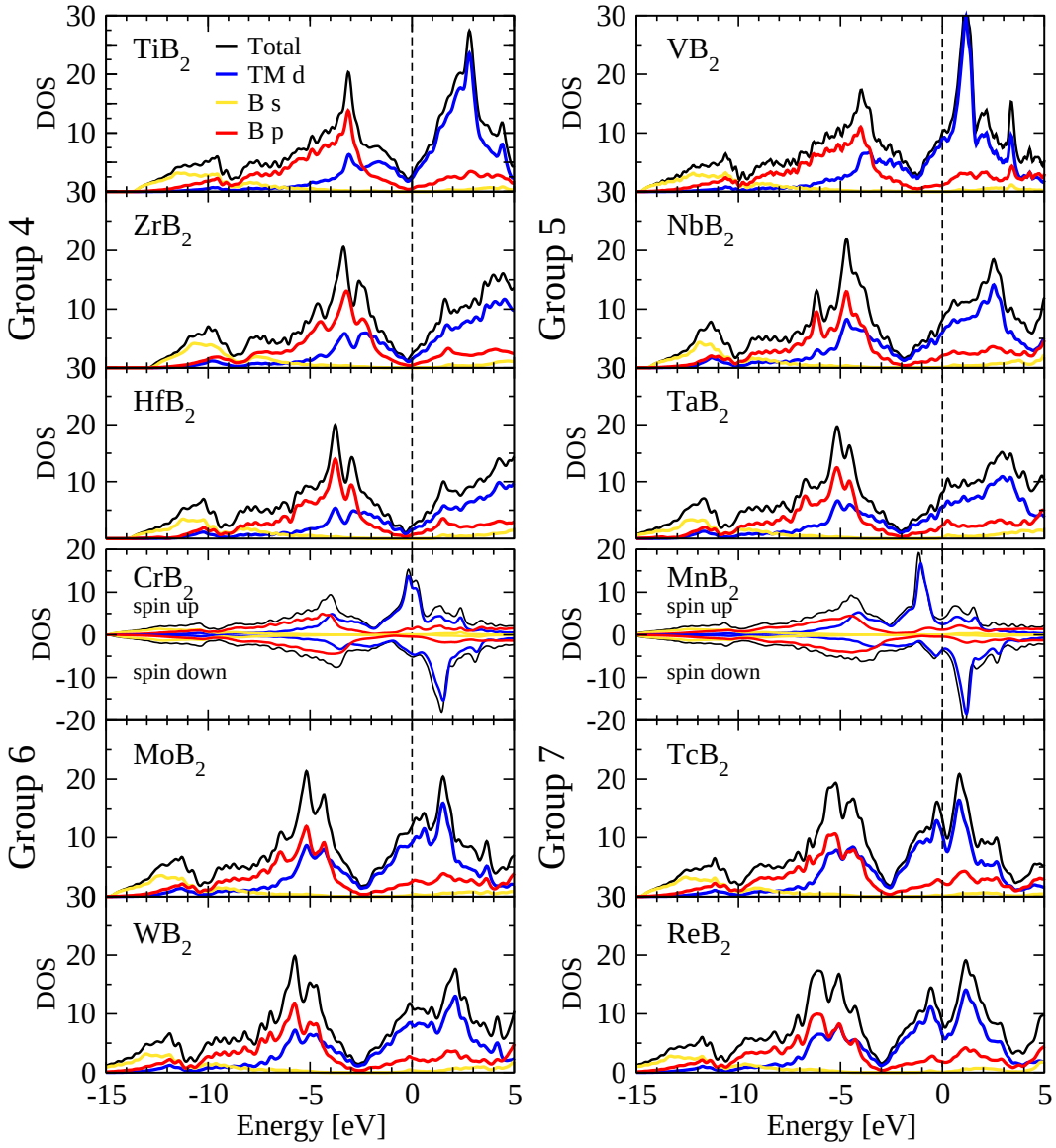

Figure 3.5: Density of states of group 4 to 7 transition metal diborides. CrB_2 and MnB_2 have magnetically ordered structures hence have different spin up and down branches. The y axis in all graphs represents DOS.

LDOS of B p and TM d what creates distinct peak below E_F. Group 4 and 5 TMDs have higher contribution of B p LDOS than of the TM d in the region of overlapping LDOS what indicates non negligible B-B interaction of B p orbitals. This difference fades as we proceed to higher group TMDs.

The position of the pseudogap with respect to E_F has significant influence on the stability of a compound. Group 4 diborides TiB_2 - HfB_2 have E_F positioned directly at the pseudogap minimum, however within higher group TMDs, the Fermi level is shifted to the region with higher DOS on the right from the pseudogap. This results in lower stability of the α structure whereas other structures like ω, ReB_2 structure or other are energetically favorable for diborides of transition metals from the group 6

and higher. The region of B s electrons partially overlaps with B p states what predicts their hybridization. In the case of diborides, sp^2 hybrid orbitals are formed thanks to which boron creates a stack of graphene like sheets.

Magnetization of CrB_2 and MnB_2 is caused by the exchange splitting of Cr and Mn d states and consequent formation of unpaired spin up peak below the Fermi level. A non-zero net magnetic moment was calculated for CrB_2 and MnB_2 with 1.11 $\mu_B/f.u.$ and 1.79 $\mu_B/f.u.$ respectively. Transition metals solely contribute to the magnetization in both cases. All studied diborides have non-zero DOS at the Fermi level what agrees with good electric conductivity of these materials. Conductive electrons are mostly TM d but some B p states are present at E_F as well.

The bond analysis was performed for all diborides of groups 4 to 7 using the LOBSTER package that outputs DOS, COHP, COOP, DOE and electron population analysis. For selected pair of atoms, COHP recognises stabilizing and destabilizing interactions based on their contribution to the band energy. COHP integrated up to E_F (ICOHP) is a parameter that reflects the strength of a bonds, the more negative ICOHP the stronger the bond should be. Since different systems have different band energies we cannot directly compare ICOHP values of different diborides. However, we can compare contribution of bonds to the total ICOHP summed over all interactions defined in the calculation. The bond analysis in this thesis was performed for interac-

Table 3.2: ICOHP percentage contribution of five shortest bonds to the total ICOHP summed over all interactions between atoms with separation lower than 5 Å and corresponding bond lengths, all calculated for the α structure.

Group		nearest neighbours			second nearest neighbours	
		B-B	TM-B	TM-TM	B-B	TM-TM
4	TiB_2	53.1 (1.75 Å)	39.8 (2.38 Å)	2.5 (3.03 Å)	1.7 (3.03 Å)	0.5 (3.23 Å)
	ZrB_2	46.1 (1.83 Å)	46.5 (2.55 Å)	4.8 (3.17 Å)	0.7 (3.17 Å)	0.6 (3.56 Å)
	HfB_2	40.0 (1.82 Å)	50.7 (2.52 Å)	5.8 (3.14 Å)	0.6 (3.14 Å)	0.6 (3.49 Å)
5	VB_2	51.9 (1.73 Å)	41.5 (2.30 Å)	2.0 (3.00 Å)	1.9 (3.00 Å)	0.6 (3.03 Å)
	NbB_2	43.6 (1.80 Å)	48.2 (2.45 Å)	4.0 (3.11 Å)	0.9 (3.11 Å)	0.7 (3.32 Å)
	TaB_2	39.0 (1.79 Å)	51.8 (2.44 Å)	5.0 (3.10 Å)	0.8 (3.10 Å)	0.7 (3.33 Å)
6	CrB_2	53.7 (1.71 Å)	38.7 (2.29 Å)	1.6 (2.96 Å)	1.3 (2.96 Å)	0.2 (3.03 Å)
	MoB_2	47.0 (1.75 Å)	44.2 (2.42 Å)	3.7 (3.03 Å)	1.4 (3.03 Å)	0.4 (3.34 Å)
	WB_2	45.3 (1.74 Å)	44.9 (2.43 Å)	4.5 (3.02 Å)	1.4 (3.02 Å)	0.4 (3.38 Å)
7	MnB_2	55.9 (1.71 Å)	36.0 (2.25 Å)	0.4 (2.92 Å)	2.3 (2.92 Å)	0.9 (2.97 Å)
	TcB_2	52.5 (1.71 Å)	40.2 (2.41 Å)	3.6 (2.96 Å)	2.1 (2.96 Å)	0.5 (3.40 Å)
	ReB_2	49.3 (1.70 Å)	40.4 (2.44 Å)	4.5 (2.95 Å)	2.0 (2.95 Å)	0.2 (3.49 Å)

tions between two nearest neighbors of both boron and transition metal, in the case of Table 3.2 for three nearest neighbors.

In Table 3.2 contribution of five shortest bonds to the total bonding are compared between all studied diborides in the α structure. Two strongest interactions are the in plane B-B bond and TM-B bonds that holds boron and metal planes together (see Figure 3.4b). The largest contribution of B-B bond is typical for the fourth period transition metals peaking with 55.9% in MnB_2. The general trend is that within each group the strength (energy lowering contribution) of B-B bond decreases with increasing principal quantum number of valence electrons. This is also supported by increasing boron-boron inter-atomic distance. The decrease in strength of nearest B-B bonds is accompanied by the strengthening of TM-B and TM-TM bonds. On the other hand, with an exception of group 5, the B-B contribution increases within periods as we move to higher group TMs what is in contradiction with predicted decreasing capability of electron donation to boron atoms. The energy lowering contribution of TM-B bond is the highest in HfB_2 and TaB_2 what is in agreement with conclusions made in previous section.

The bonding in diborides is closely related to the charge transfer between metal and boron atoms. In Table 3.3 are summarized calculated orbital occupations and related charge transfer from transition metals to boron. Electrons from *s* orbital of TM are transferred both to TM *d* orbital as well as to B *p* orbital. Except from the sixth group TMDs, electron donation to boron decreases within groups. The donor capability of TMs in period does not obey such a simple rule. The electron transfer in period 4 and 5 (Ti - Mn and Zr - Tc) decreases with increasing atomic number. An exception to this trend are group 7 TMDs where the charge transfer grows mainly due to donation of TM *d* electrons, which contradicts the idea of stable half filled *d* shell. In period 6 (Hf - Re) electron transfer increases with higher atomic number of TM which is exactly opposite behavior of expected. In comparison to Table 3.2 the strength of B-B bond is proportional to the charge transfer from TM. As the charge transfer drops, B-B bonds weaken probably due to weaker B-B π bond. The opposite can be said about TM-TM bond which becomes stronger thanks to higher amount of charge on metal atoms. The decrease of importance of B-B interaction between period 4 and 6 diborides is smaller in TMDs of higher groups. Also charge transfer difference between period 4 and 6 diborides decreases in higher groups. More significant loss of the charge transfer to boron layer within groups 4 and 5 weakens B-B interaction and simultaneously the TM-B bond becomes overall stronger. Even though the sum over all TM-B bonds becomes more stabilizing than B-B contribution, single in-plane boron bond is always the strongest one. The DOS plots in Figure 3.5 show emergence of new peaks within period 5 and 6 transition metal diborides where B *p* and TM *d* orbitals are aligned which reflects new inter-layer bonds that are responsible for increased importance of TM-B bonds. We can conclude that B-B interaction is the most stabilizing when there

Table 3.3: Mulliken and Löwdin population analysis and the electron transfer from transition metals to boron in group 4 - 7 transition metal diborides.

		Mulliken		Löwdin		Charge transfer	
		TM	B	TM	B	Mulliken	Löwdin
4	TiB_2	$4s^{0.17}3d^{2.58}$	$2s^{0.91}2p^{2.71}$	$4s^{0.29}3d^{2.70}$	$2s^{0.74}2p^{2.77}$	-1.25	-1.01
	ZrB_2	$5s^{0.15}4d^{2.72}$	$2s^{0.97}2p^{2.60}$	$5s^{0.28}4d^{2.90}$	$2s^{0.76}2p^{2.65}$	-1.13	-0.82
	HfB_2	$6s^{0.62}5d^{2.56}$	$2s^{0.88}2p^{2.54}$	$6s^{0.45}5d^{2.79}$	$2s^{0.73}2p^{2.65}$	-0.82	-0.76
5	VB_2	$4s^{0.20}3d^{3.63}$	$2s^{0.88}2p^{2.70}$	$4s^{0.29}3d^{3.74}$	$2s^{0.73}2p^{2.76}$	-1.17	-0.97
	NbB_2	$5s^{0.19}4d^{3.92}$	$2s^{0.86}2p^{2.58}$	$5s^{0.28}4d^{4.07}$	$2s^{0.69}2p^{2.63}$	-0.89	-0.65
	TaB_2	$6s^{0.55}5d^{3.55}$	$2s^{0.83}2p^{2.60}$	$6s^{0.43}5d^{3.73}$	$2s^{0.70}2p^{2.71}$	-0.86	-0.83
6	CrB_2	$4s^{0.13}3d^{4.88}$	$2s^{0.84}2p^{2.65}$	$4s^{0.26}3d^{4.98}$	$2s^{0.69}2p^{2.69}$	-0.99	-0.76
	MoB_2	$5s^{0.19}4d^{4.92}$	$2s^{0.84}2p^{2.61}$	$5s^{0.29}4d^{4.82}$	$2s^{0.69}2p^{2.65}$	-0.89	-0.69
	WB_2	$6s^{0.33}5d^{4.54}$	$2s^{0.83}2p^{2.73}$	$6s^{0.35}5d^{4.68}$	$2s^{0.70}2p^{2.78}$	-1.13	-0.97
7	MnB_2	$4s^{0.07}3d^{5.61}$	$2s^{0.88}2p^{2.78}$	$4s^{0.26}3d^{5.68}$	$2s^{0.73}2p^{2.80}$	-1.32	-1.06
	TcB_2	$5s^{0.18}4d^{5.73}$	$2s^{0.86}2d^{2.68}$	$5s^{0.30}4d^{5.82}$	$2s^{0.71}2p^{2.73}$	-1.09	-0.88
	ReB_2	$6s^{0.36}5d^{5.55}$	$2s^{0.82}2p^{2.72}$	$6s^{0.39}5d^{5.66}$	$2s^{0.70}2p^{2.78}$	-1.09	-0.96

is large charge transfer to boron and TM-B interaction strengthens with lower charge transfer.

The charge transfer from TM atoms suggests that the largest ionic contribution to the bonding should be characteristic for MnB_2 with the largest charge transfer and not for HfB_2 as electronegativities predict. The ionicity of TM-B bond was calculated for some diborides in ref. [134] and it should decrease in the order of Mn, Cr, Zr, Hf, Nb, Ta, V and Ti diborides from the highest to the lowest ionic contribution. This order does not fully correspond to our calculated charge transfer if we assume that the larger charge transfer the more ionic TM-B bond.

3.3.1. ELF and charge density analysis

To get an insight into the electronic structure and electron transfer between metal and boron we have plotted the electron localization function (ELF) and charge density difference between TiB_2 and HfB_2 as well as between TiB_2 and ReB_2. Using these two examples we can study the differences in the charge distribution within diborides of TM from both the same group and from the higher group. ELF and charge density maps are plotted in Figure 3.6 and 3.7, in all cases we subtracted electron distribution from the one of TiB_2. That means that in red regions there is an excess of ELF or charge density in TiB_2 and in blue regions there is an excess in HfB_2 or ReB_2. The ELF uses

the conditional pair density to determine regions with high density of localized electrons and therefore comprises, among others, information about the covalent bonding.

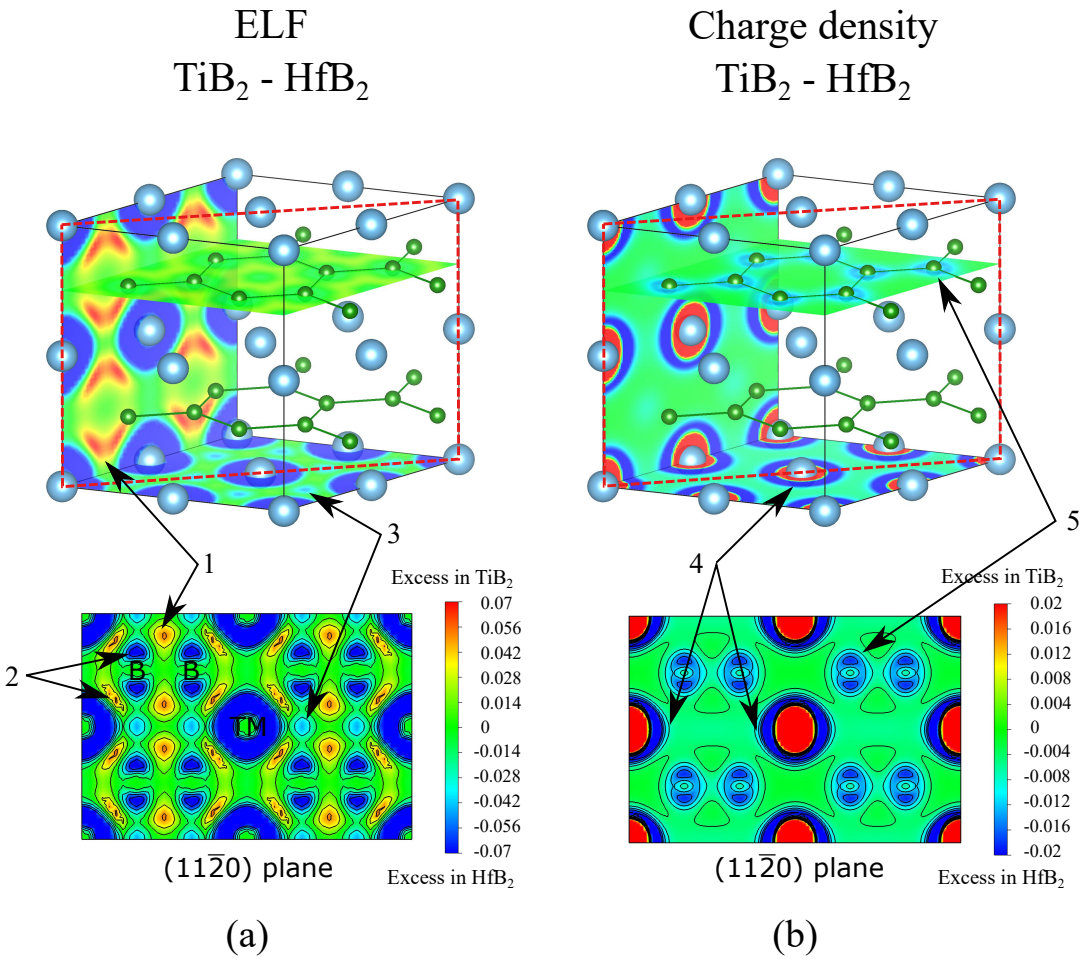

Figure 3.6: ELF and charge density difference maps, comparison of TiB_2 and HfB_2. Red dashed rectangle represents the (11$\bar{2}$0) plane cut, regions pointed at by arrows are discussed in the text with corresponding number.

Figure 3.6 depicts the ELF difference between diborides of Ti and Hf. It is apparent that the π bond between boron atoms is weaker in HfB_2 (arrow 1). Electrons in TiB_2 are more localized in between boron atoms above and below the σ bond what is visible also in (11$\bar{2}$0) plane cut. This is a consequence of a smaller electron transfer from Hf to B which is supported by lower B-B bond strength in HfB_2. In HfB_2 electrons are more localized on boron atoms and their localization in between TM and B is surprisingly lower than in TiB_2 (arrow 2). This should mean less covalent Hf-B bond, however, as indicated in Table 3.2, Hf-B interaction is more stabilizing hence stronger than Ti-B. The regions with more localized electrons in between Hf atoms (arrow 3) correspond to boron positions and the localization of electrons above and below B atoms. This hints towards a stronger inter-layer interaction of B p_z orbitals, however such long interaction between boron atoms is not probable. Possible is interaction with some of the metal's

in-plane *d* orbitals (xy and [x^2-y^2]). Overlay of exactly these orbitals can be found in LDOS and projected DOS of HfB_2 shown in Appendix A. Formation of this bond could be responsible for TM-B bond strengthening. The charge density difference map between TiB_2 and HfB_2 in Figure 3.6b indicates uniform metallic distribution of charge in metallic planes parallel to the boron layers in both diborides (arrow 4) with somewhat higher density in HfB_2 thanks to lower charge transfer. In the boron layer charge is slightly more localized on and between boron atoms in the case of HfB_2 (arrow 5) which is the same behavior that we can see in the ELF difference map.

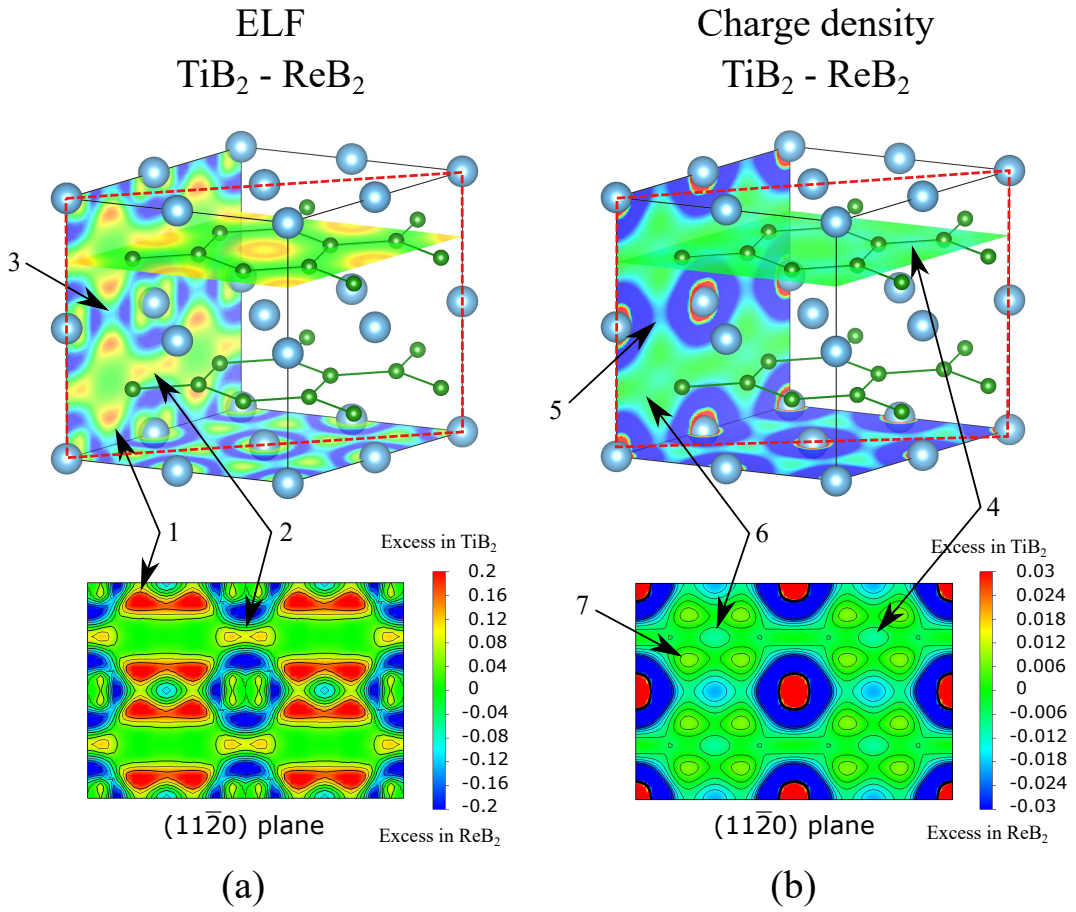

Figure 3.7: ELF and charge density difference maps, comparison of TiB_2 and ReB_2. Red dashed rectangle represents the (11$\bar{2}$0) plane cut, arrows with corresponding number are explained in the text.

Similar trends can can be recognized when we compare TiB_2 and ReB_2. The ELF difference between TiB_2 and ReB_2 is plotted in Figure 3.7a. Electron localization in ReB_2 is lower in π bonds of boron (arrow 1) as predicted from comparison of LDOS of early and middle TM diborides. This fact indicates weaker B-B bond in ReB_2. Localization between Re atoms across the boron layer (arrow 2) is also lower which is probably related to boron excess of charge in TiB_2 rather than to TM-TM interaction, even though the second nearest neighbors Re-Re bond is slightly weaker than Ti-Ti

(see Table 3.2 for relative bond strengths). On the other hand, Re-Re shortest in-plane bond becomes stronger and is partially of covalent nature as there is localization of electrons between Re-Re atoms (arrow 3). ELF difference in the basal plane suggests more directional character of Re-Re bonds and higher electron localization in region between Ti atoms in TiB_2. The charge density difference map in Figure 3.7b shows higher density of electrons between boron atoms (arrows 4) and somewhat lower density in out of plane π boron orbitals in ReB_2. Charge density distribution around Re atoms is elongated in the direction of nearest neighbors with notable density in between Re atoms (arrow 5). Higher electron density is located between Re atoms and the middle of the B-B short bond (arrow 6) on the contrary, the charge density directly between Re and B is lower in ReB_2 than it is in TiB_2 (arrow 7).

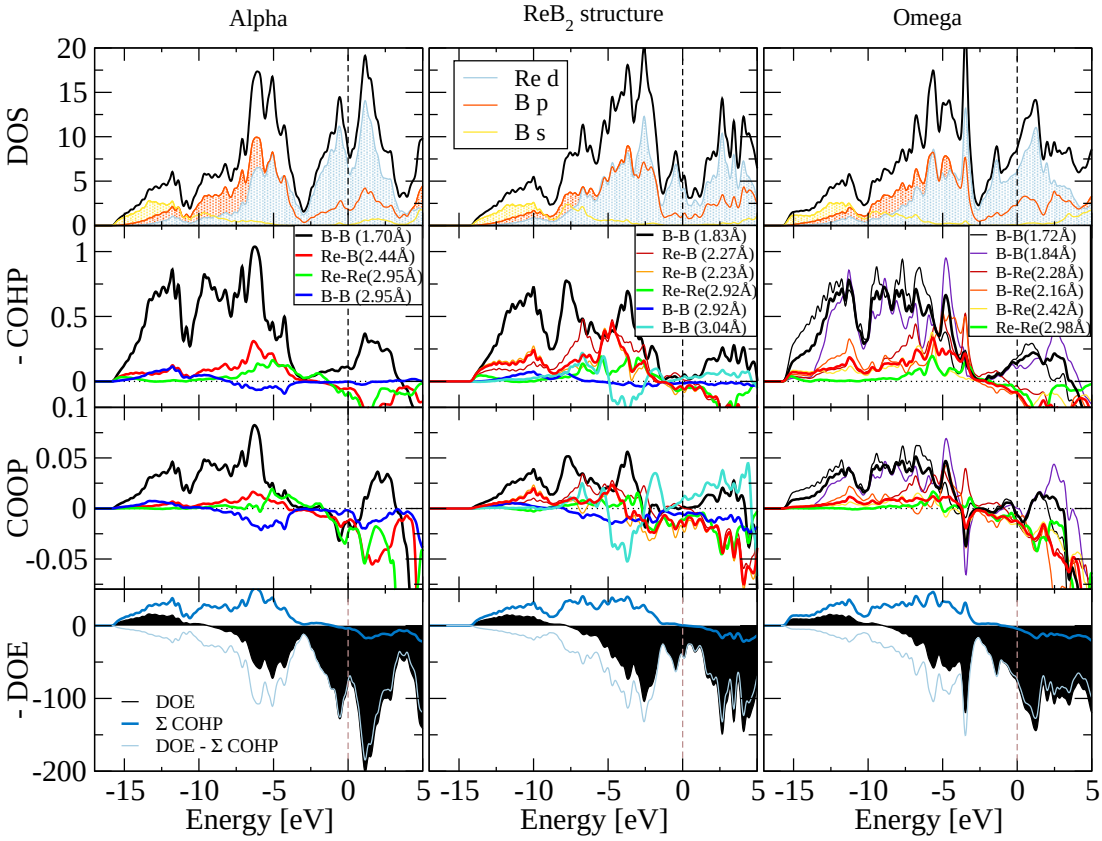

Figure 3.8: Comparison of DOS, negative COHP, COOP and negative DOE calculated for three different crystal structures typical for transition metal diborides. Thick line curves within COHP and COOP represent proportionally averaged interactions of identical type. DOE is compared with the COHP summed over all interactions shorter than 5 Å plotted as thick color line and with the on-site interaction contributions, obtained by subtracting summed COHP from DOE. COHP and COOP curves are are plotted in units per bond.

3.3.2. Bonding analysis and shear deformation

Bonding in materials plays an important role in the stability of structures. As an example, we have calculated ReB_2 within three typical crystal structures of diborides. Calculations have shown that the most stable is the ReB_2 structure in which all boron layers are puckered (Figure 2.2b), the total energy of the ω structure (Figure 2.2c) is higher by 0.32 eV/atom and the total energy of the α structure (Figure 2.2a) is higher by 0.64 eV/atom. From results summarized in Figure 3.8, DOS supports the stability of the ReB_2 structure since the number of states on E_F is the lowest among these three structures. In LDOS of the stable structure we can see the overlap of almost identical B p and Re d orbitals indicating stronger hybridization than in the other two structures, which creates new states with lower energy filled by electrons that in remaining two structures would occupy states around E_F. The stronger interaction corresponds to greater Re-B COHP peak (red curve) around -5 eV in the stable structure. This bond is also shortest in the stable structure. The strengthening of Re-B bond occurs at expense of B-B strength what is manifested by the COHP minimum opening in B-B interaction at the same energy region. There aren't any pronounced antibonding interactions near E_F in neither of compared structures, however, the sum of -COHP over all calculated interactions (thick blue line in the DOE plot) is not positive at E_F (not destabilizing) only in the case of the stable structure. Since DOE comprises contributions from both off-site (between electrons on different atoms) and on-site interactions (between electrons on the same atom), its positive values within the plotted range are caused by the destabilizing on-site interactions. Nevertheless, the integral of DOE up to E_F (i.e. bthe band energy, not shown in Figure 3.8) is negative for all structures thanks to strong stabilizing effect of core electrons. Bonds for which COHP and COOP were calculated are shown in Figure 3.4b.

The total energy as a function of deformation of diborides with the α structure is plotted in Figure 3.9. Both shear deformation (Figure 3.9a) as well as tensile deformation (Figure 3.9b) were calculated using constant volume for all deformation values. The steepness of these lines indicates the energy demandingness of the corresponding deformation and therefore structure's resistance to this deformation mode. In the case of the shear deformation, the deformation value characterized by the x axis in Figure 3.9a changes from the undeformed alpha structure at 0% to 50% shear where atoms in every third metal layer are shifted by a half of the basal lattice vector along the $[2\bar{1}\bar{1}0]$ direction (direction of the lattice vector a). We can see that diborides of group 4 and 5 transition metals (Ti - Hf and V - Ta) are energetically the most difficult to shear and and should be the most resilient to this deformation mode. We can deduce from Figure 3.9a that the most difficult to shear is TiB_2 whereas the easiest to shear is the α structure ReB_2. The stable ReB_2 structure of rhenium diboride responds to shear with more resistance, this is expressed by the dark violet line with empty triangle symbols. If we assume that shear resistance is mostly related to inter-layer TM-B bonds, we

can deduce that this bond is strongest in group 4 TMDs and decreases within higher groups. This trend agrees with lower charge transfer to boron atoms from higher group transition metals.

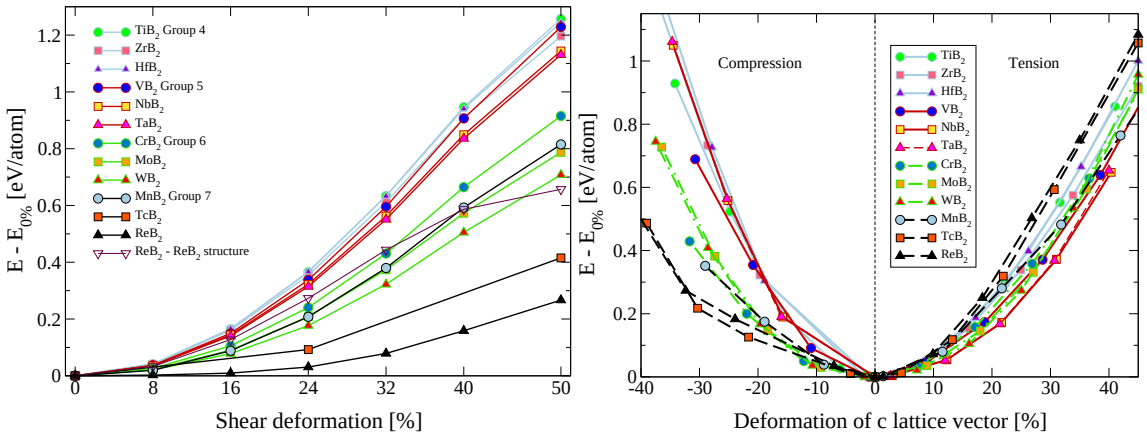

(a) (b)

Figure 3.9: Total energy as a function of a) shear deformation and b) deformation along the c lattice vector.

The response to the compression and elongation along the c lattice vector calculated with a constant volume for all deformation steps is plotted in Figure 3.9b. Here the x axis represents in percents the deformation of the c lattice vector compared to the undeformed structure. In compression TM-B bonds are squeezed and B-B or shortest TM-TM bonds are elongated, in tension the other way around. In the case of compression, the most resistant are group 4 and 5 TMDs followed by diborides of group 6 and 7 transition metals. The most resistant is HfB_2 and the least resistant is TcB_2 in the α structure. The elongation is energetically most difficult for group 7 TMDs (ReB_2 and TcB_2). On the other hand the least difficult to deform in tension are group 5 TMDs. Experimentally, ReB_2 is known as one of the most incompressible materials [92], this however is not supported by the energy dependence of the compression deformation. A probable cause of this inconsistency is the metastable α structure used in calculations.

The effect of the shear deformation on the bond stabilizing contribution to the band energy of the three shortest bonds is plotted in Figure 3.10. Each diboride is represented by three columns that from left to right indicate 0%, 24% and 50% shear deformation (deformation notation is explained in previous paragraphs). The fraction of B-B contribution decreases within each group, the largest difference is present between HfB_2 and TiB_2. Surprisingly, the portion of B-B bond increases for higher group TMDs. The first observation agrees with decreased charge transfer to boron atoms, the second does not. However, besides possible B-B bond strengthening that is not probable due to lower electron transfer from TM, increased B-B contribution of higher group TMDs might be caused by TM-B bond weakening. In general the strength of B-B bond decreases as result of the shear along the a lattice vector. On the other hand TM-B

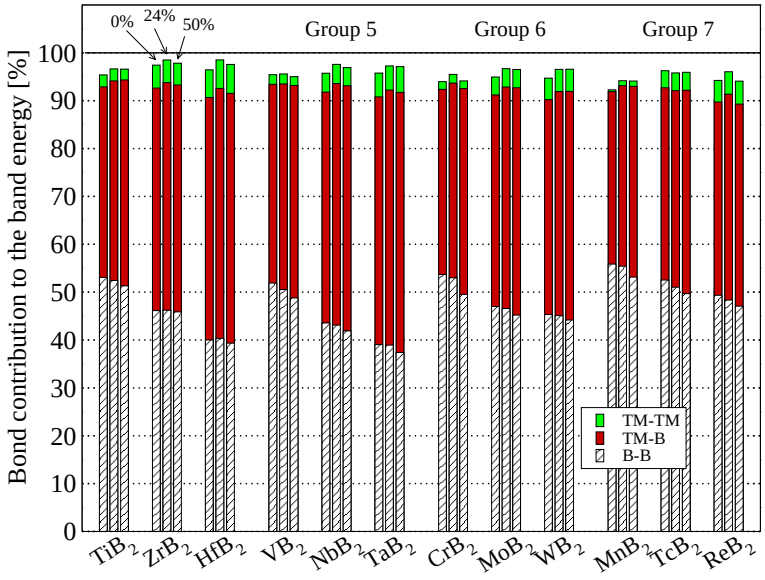

Figure 3.10: Contribution of the three most important bonds to the total ICOHP summed over all interactions shorter than 5 Å in group 4 - 7 transition metal diborides. First column for each diboride represent undeformed structure, second column 24% and third 50% shear deformation.

and in some cases TM-TM bonds get stronger due to the shear deformation. Decreased strength of B-B bonds as result of shear deformation is in correlation with lower charge transfer from TM in sheared structures. The charge transfer according to Mulliken and Löwdin as a function of shear is summarized in Figure 3.11. Electron transfer is in all diborides is lowered due to shear deformation.

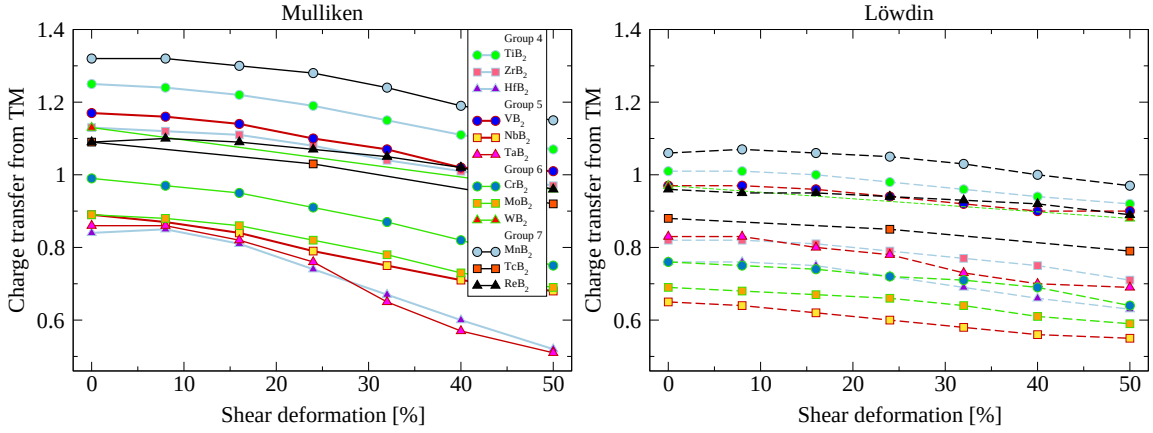

(a) (b)

Figure 3.11: Charge transfer from TM to boron as a function of shear deformation calculated using a) Mulliken population analysis and b) Löwdin population analysis. Unit cell was sheared along the $\boldsymbol{a}$ lattice vector that is [100] or $[2\bar{1}\bar{1}0]$.

As mentioned before, the ICOHP values cannot be directly compared for different structures, however, COOP integrated up to E_F (ICOOP) can be compared between diborides since COOP integrates to the number of electrons participating on interaction. This quantity therefore reflects amount of shared electrons between atoms forming a bond and we can assume that the higher the ICOOP the more covalent the interaction is. ICOOP dependence on the shear is plotted in Figure 3.12a for B-B interaction and in Figure 3.12b for TM-B interaction. As expected, B-B interaction is the most covalent in period 4 transition metal diborides (Ti - Mn) for which the charge transition to boron is the most pronounced. ICOOP decreases with deformation in all TMBs, what is consistent with ICOHP in Figure 3.10. In the case of TM-B the largest covalent fraction can be assigned to NbB_2 and ZrB_2. The lowest covalency of this bond was obtained for MnB_2 where the charge transfer to boron is the largest and the ionic contribution should be the most important among studied TMDs. The second largest charge transfer from TM atoms was calculated for TiB_2, however, this diboride shares more electrons in TM-B bond than few other diborides with lower charge transfer. This means that lower charge transfer does not weaken TM-B and B-B bonds evenly in all TMDs. Except from CrB_2 and MoB_2, TM-B orbital overlap decreases at higher deformation.

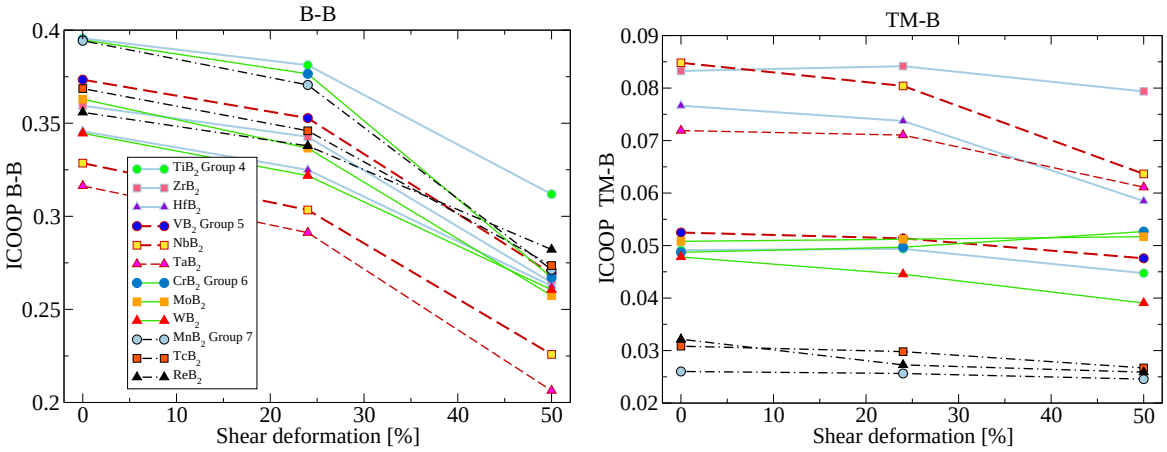

(a) (b)

Figure 3.12: Integrated COOP of a) B-B and b) TM-B bonds as a function of shear deformation.

To analyze the effect of the shear deformation on the bonding in diborides, we compared TiB_2 and ReB_2 whose transition metals are the furthest away from each other in the periodic table. We compare DOS, COHP, COOP and DOE for both undeformed structure and sheared along the a lattice vector. In Figure 3.13 are presented results for TiB_2. Bonds analyzed in undeformed structure are highlighted in the unit cell in Figure 3.4b. The DOS of the undeformed structure is separated into orbital projected DOS

(PDOS) to distinguish different spatially oriented p and d orbitals. The boron s orbital hybridizes with degenerate in-plane p_x and p_y to form strong stabilizing sp^2 orbital. The sum of p_x and p_y orbitals have more or less featureless character around -5 eV and these orbitals are responsible for further B-B interactions. The p_z orbital perpendicular to the boron layer seems to be responsible for TM-B interaction and contributes little to B-B bonding. This is supported by COHP of the B-B interaction that is prominent in energy range where B s and B $p_{x/y}$ are present and the B p_z peak at -3 eV is not reflected in B-B curve but can be clearly distinguished in TM-B COHP. The crystal field in the case of TM splits d orbitals into degenerate in-plane $(xy + [x^2 - y^2])$ and perpendicular $(xz + yz)$ as well as nondegenerate z^2 orbital that is perpendicular to the boron layer as well. We can see that the non zero DOS at E_F is mainly due to $(xy + [x^2 - y^2])$ and $(xz + yz)$ d orbitals what suggests conductivity in both directions parallel and perpendicular to boron layers. The strong localization of the d_{z^2} orbital above E_F was explained as a consequence of avoided band crossing of B π and TM d_{z^2} bands [135]. The distinct DOS peak at -3 eV results mainly from the interaction of B p_z and $d_{(xz+yz)}$ orbitals. The broad character of in-plane $d_{(xy+[x^2-y^2])}$ between -4 eV and E_F indicates a self interaction between Ti atoms presumably of the metallic character.

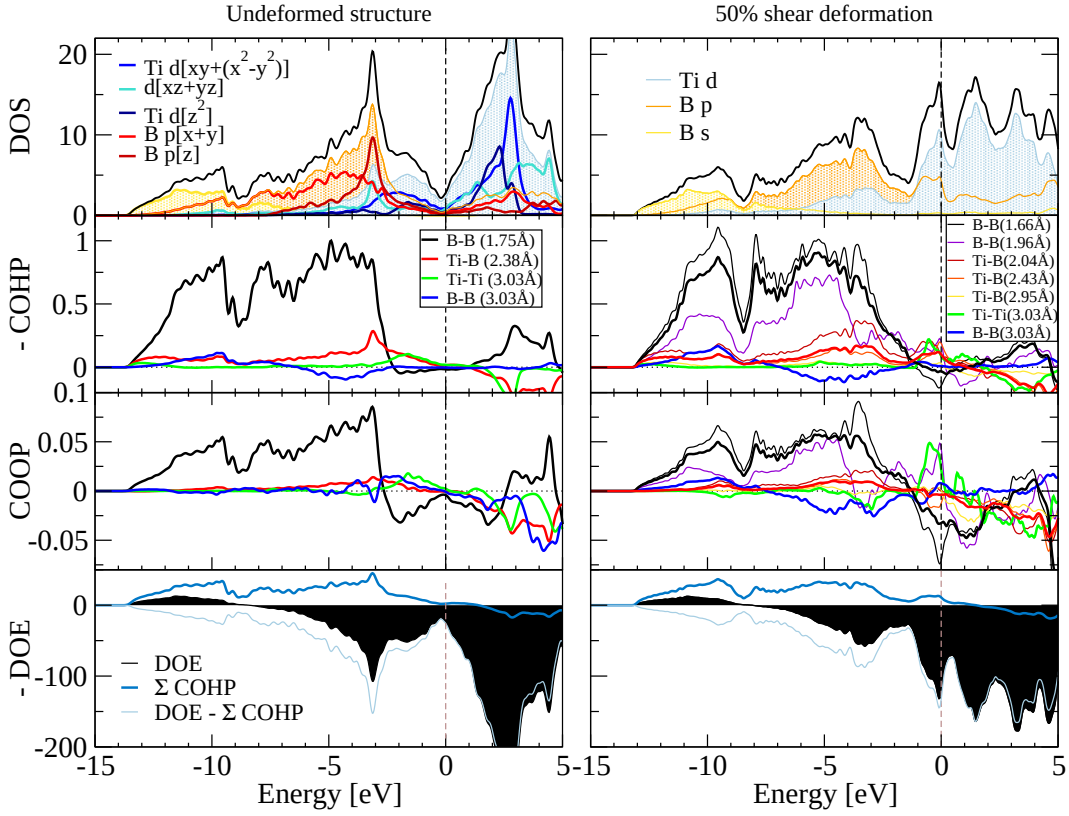

Figure 3.13: Bond analysis of the α structure TiB_2 in undeformed and sheared lattice. The average COHP and COOP of B-B and Ti-B in deformed structure are plotted with thick line.

The same but in smaller scale can be said about d_{z^2} orbitals that mediate interactions of metal atoms across the boron layer. These interactions were assumed to contribute to destabilization of the α structure in higher group transition metal diborides.

The shear deformation breaks degeneracy of TM d orbitals therefore for clarity only LDOS is plotted. New states emerge on E_F in Figure 3.13 due to the deformation which is the sign of structure destabilization. Even though the peak at -3 eV is not as distinct as in the undeformed structure, the over all TM-B interaction becomes stronger what might be associated with new interaction directly at E_F, what can be seen from the DOS and COHP plots. The shear deformation splits B-B bond into shorter and longer bonds compared to the undeformed lattice in 1:2 ratio in favor of the shorter bond. In the case of Ti-B there are three bonds of different lengths that are represented equally in the deformed state. These branches are represented by thin lines in Figure 3.13 and 3.14, thick lines are their proportional averages. COOP and COHP show strong covalent TM-TM interaction at E_F is the sheared lattice. The main difference can be seen, besides DOS, in the DOE plot. The average COHP is more negative in the deformed state, however, the on-site interactions (thin color line in DOE plots) are much more destabilizing in the deformed state.

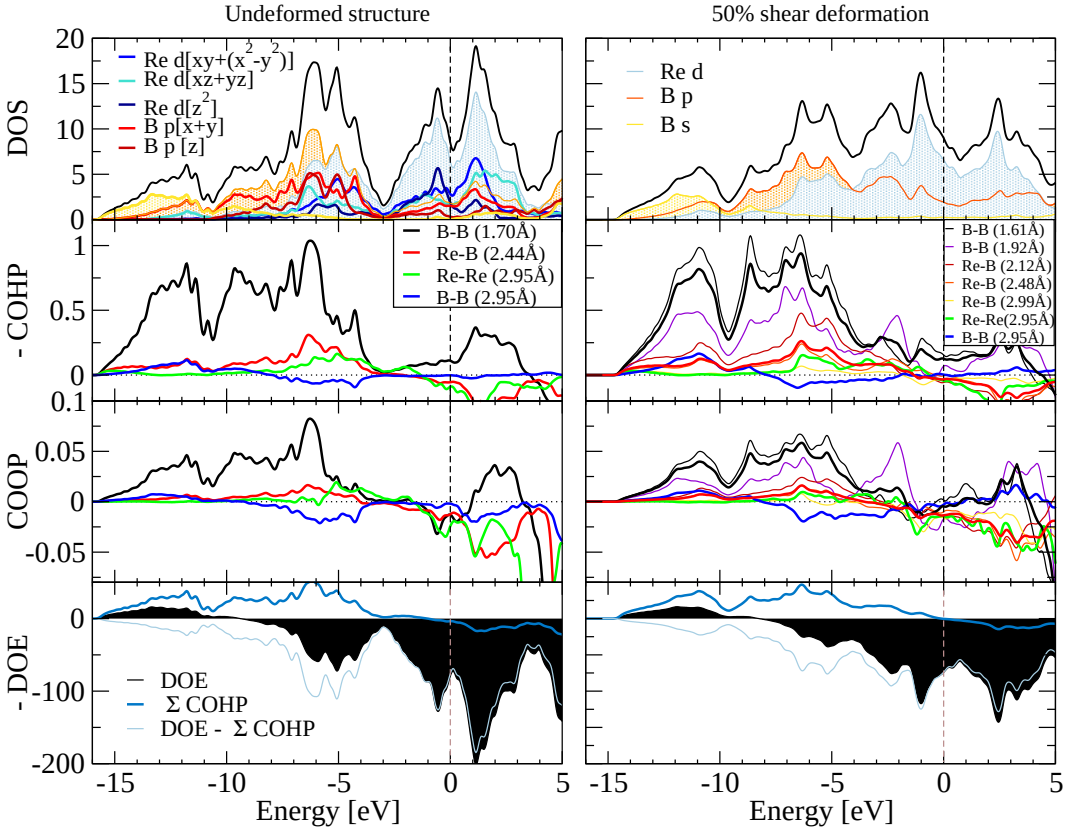

Figure 3.14: Bond analysis of ReB_2 with the α structure, comparison of undeformed state (0%) and lattice sheared along basal unit cell vector (50%).

The influence of shear deformation on bonding in ReB_2 is compared with the undeformed structure in Figure 3.14 in the same way as in the case of TiB_2. The increased number of electrons results in the shift of E_F to higher DOS on the right side of the pseudogap. The projected DOS indicates more complex interactions between B p and Re d than in TiB_2. Here the B p_z orbital interacts not only with $(xz + yz)$ but also with $(xy + [x^2 - y^2])$ d orbitals that lie in the metal plane. The COHP shows higher values (more stabilizing) for TM-TM bond and its spread smooth shape indicates metallic character, however in COOP we can see peaks around -5 eV so this bond has some covalent contribution as well. Filling of states above the pseudogap results in antibonding TM-TM and TM-B interactions above -2 eV. The shear deformation of already not stable ReB_2 unit cell doesn't lead to emergence of significant destabilization features in DOS COHP or DOE what is reflected in low energy requirements for deformation Figure 3.9a. Throughout this chapter we use deformation up to 50% that is far beyond experimentally reachable values. However only exaggeration of deformation allows us to observe changes in the electronic structure and bonding at noticeable scale. Bond analysis of all group 4-7 TMDs in the undeformed lattice can be found in Appendix A.

3.4. Ni_2MnGa

In the case of Ni_2MnGa we study energetics of bonds and the effect of corrective Hubbard U parameter on inter-atomic interactions and structural stability of austenite and NM martensite. As already mentioned, here we go beyond the usual approach when U is applied on Mn atoms solely and in addition we elaborate cases with U on Ni as well as on both Ni and Mn at the same time. In all three cases we used U = 1, 3 and 5 eV. When used on Ni and Mn together the U value was the same on both elements. Results of structural and magnetic properties are listed in Table 3.4 compared with experimental data.

Standard GGA calculation without U corrections predicts slightly smaller lattice parameter of the cubic phase than the experiment what is consistent with previous works. Our relaxed structure and magnetic moments reproduce published computed results very well [136]. With U on Ni the lattice parameter first slightly decreases and then for U (Ni) = 5 increases to value larger that obtained by standard GGA. This change in trend is probably caused by the competition of different structure and magnetic variants whose energy approach each other at higher U. The net magnetization increases as U grows in both austenite and martensite within all three types of U implementation. In the case of U applied to Mn atoms the lattice parameter and the local magnetization of Mn both increase with U. Lattice parameters are somewhat

Table 3.4: Calculated lattice parameters of cubic austenite a_A, tetragonality c/a, total and local magnetic moments μ in austenite and martensite with different U values compared with experiment [102], [112]. Experimental value of martensite tetragonality refers to 10M variant.

Method				AUSTENITE			MARTENSITE		
	a_A [Å]	$c/a > 1$ [-]	$c/a \leq 1$ [-]	μ_{tot} [μ_B/f.u.]	μ_{Mn}	μ_{Ni}	μ_{tot} [μ_B/f.u.]	μ_{Mn}	μ_{Ni}
U (Ni) = 1	5.802	1.245	0.937; 1	4.18	3.40	0.41	4.21	3.32	0.49
U (Ni) = 3	5.791	1.193	0.936	4.55	3.47	0.57	4.42	3.35	0.60
U (Ni) = 5	5.824	1.111	0.981	4.95	3.47	0.81	4.74	3.42	0.76
U (Mn) = 1	5.828	1.203	1	4.31	3.66	0.34	4.46	3.64	0.43
U (Mn) = 3	5.875	1.130	1	4.60	4.06	0.28	4.79	4.07	0.37
U (Mn) = 5	5.917	-	1	4.76	4.32	0.22	-	-	-
U (NiMn) = 1	5.833	1.188	0.943; 1	4.45	3.69	0.40	4.61	3.68	0.49
U (NiMn) = 3	5.865	1.113	0.957	5.12	4.09	0.54	5.07	4.07	0.55
U (NiMn) = 5	5.927	1.046	1.023	5.89	4.33	0.83	5.48	4.32	0.66
GGA	5.804	1.261	1	4.11	3.41	0.36	4.10	3.32	0.42
Experiment	5.825	-	0.939	2.86			4.17		

smaller than 5.93 Å with U (Mn) = 3.93 eV reported in [128]. The growth of the local magnetic moment of Mn is accompanied by the decrease of Ni contribution as if Ni electrons became more delocalized in attempt to mediate stronger interaction of Mn atoms with more localized d electrons. When U is applied on both Ni and Mn we can see an increase of the unit cell volume as well as of the net magnetization which results from combination of magnified local magnetic moments of Ni and Mn. The best agreement with experimental lattice parameter is obtained with U (Ni) = 5 eV, U (Mn) = 1 eV and U (NiMn) = 1 eV.

In order to study effect of the U correction on the stability of NM tetragonal martensite we calculated energy of Ni_2MnGa as a function of tetragonality. Resulting curves for the three types of U implementation considered in this work are summarized in Figure 3.15, in Table 3.4 are listed corresponding c/a ratios of present energy minima. Curves plotted in Figure 3.15 were calculated using the constant volume of the austenite unit cell for every c/a, Figs. a), b), c) are plotted relative to the energy of cubic structure.

Figure 3.15a and 3.15b represent energy and total magnetic moment along the tetragonal deformation path when U was applied to Ni atoms. The well known shape of the GGA energy curve with a metastable minimum at $c/a = 1$ and a stable minimum at $c/a \approx 1.25$ is partially disturbed already at U (Ni) = 1 eV when two distinct minima are present one with c/a above and other below the cubic ratio. There is also a very shallow minimum at $c/a = 1$. As we increase U (Ni) to 3, the austenite minimum disappears completely and we are left with a metastable structure with tetragonality lower than 1 and the stable NM martensite with $c/a > 1$. Energy difference between these two structures and the austenite increases and the tetragonality of the NM martensite gets lower compared to U (Ni) = 1 eV. Interesting is the appearance of the second minimum with $c/a < 1$ since experimentally observed structures have tetragonality lower than one, however their stability is provided by modulations of crystallographic planes. Previously smooth $E \sim c/a$ dependence is separated into two minima with a much sharper crossing what is visible also at the magnetization. For U (Ni) = 5 eV the situation changes what is probably related also to a sudden increase of the lattice parameter (see Table 3.4). We can notice two completely separated minima, the metastable minimum is positioned at c/a slightly lower than 1. The effect of U on Ni atoms resides in destabilization of austenite, in lowering of c/a ratio of the stable NM martensite and in the emergence of new meta-stable structure with $c/a < 1$ as well as in the increase of the net magnetic moment.

The effect of U correction applied to Mn electrons on structural stability of Ni_2MnGa is plotted in Figure 3.15c and 3.15d. On the contrary to U on Ni, the trend of changes is the same for all values of U. NM martensite becomes energetically meta-stable for U (Mn) = 3 eV and for U (Mn) = 5 eV the only present minimum is the austenite. This is consistent with previously calculated tetragonal deformation energy curve [110]. The total magnetization increases with U as Mn d electrons become more localized,

however, the shape of magnetization vs. tetragonality curve is the same for all tested values of U. This is different behavior from U on Ni (Figure 3.15b)) and supports the idea that even though Mn is a strong source of magnetic moment in the system, the magnetic structure is mediated by Ni and Ga. The application of U on Mn results in stabilization of the cubic structure and the increase of the net magnetic moment thanks to increasing Mn local magnetic moment.

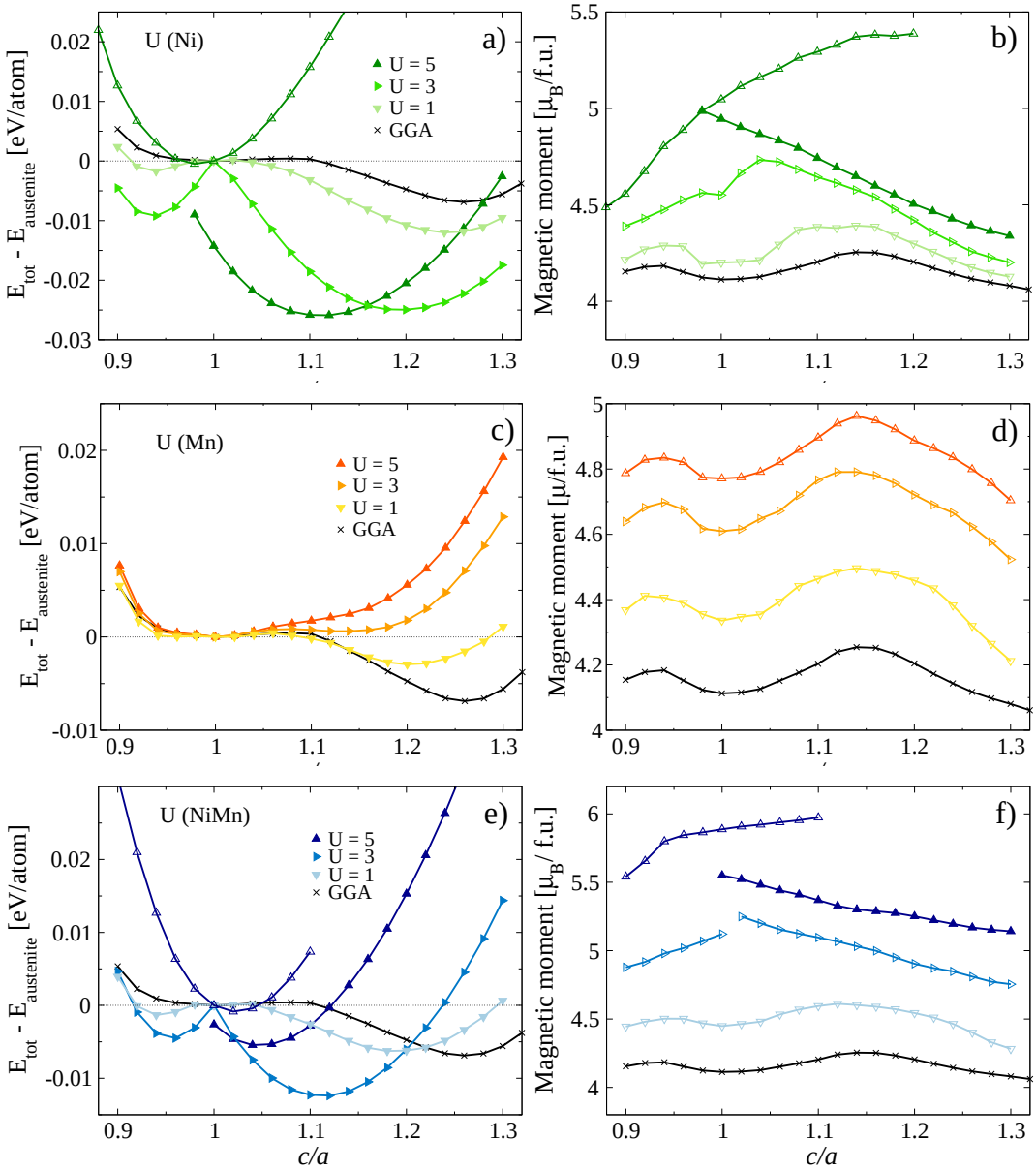

Figure 3.15: Energy and total magnetic moment as a function of c/a compared between different applications of U parameter.

Figure 3.15e and 3.15f show results of calculations with U on both Ni and Mn, as expected the effect of this correction is a combination of U on Ni and U on Mn. We can see destabilization of austenite and emergence of energy minimum with tetragonality

lower than one. Energy curves along the tetragonal deformation resemble the situation in Figure 3.15a where U correction is assumed on Ni atoms. The effect caused by U on Mn is lower energy difference between austenite and martensite. Compared to U on Ni, in the case of U (NiMn) = 5 eV the energy of NM martensite is closer to the energy of austenite than in lower U curves. When we apply U (NiMn) = 5 eV the energy curve splits into two distinct minima, the metastable structure with a higher magnetic moment what is in Figure 3.15f represented by distinct net magnetization curve above the one of the stable structure. The tetragonal deformation curve calculated with U (NiMn) = 1 eV still keeps a very shallow minimum at $c/a = 1$. The total magnetization in the case of U (NiMn) reaches the highest values as both local magnetic moment contributors Mn and Ni increase their magnetic moments due to enhanced localization of electrons which is summarized in Table 3.4 as well. From Figure 3.15 we can deduce that the effect of U on Ni is stronger than the effect of U on Mn which is apparent in the case of U (NiMn). If we compare DFT+ U results with GGA calculation, we obtained much higher total magnetization and decrease of tetragonality of the NM martensite with the corrected functional. The best agreement of the metastable structure with experimental 10M c/a ratio was calculated with U (Ni) = 1 eV, U (Ni) = 3 eV and U (NiMn) = 1 eV.

Figure 3.16 covers DOS plots calculated using the LOBSTER package, GGA results are compared with results corrected by U = 3 eV in all three cases. Lower stability of austenite compared to NM martensite is usually reasoned by the presence of the peak on E_F in the spin down DOS channel. Tetragonal deformation shifts the Fermi level into the region of pseudogap created thanks to the Janh-Teller effect. Consequent lower DOS at E_F is related to a greater stability of distorted structure. The ferromagnetism is caused by uneven distribution of occupied electron states in up and down spin branches which is more apparent in the case of Mn electrons that are responsible for the large net magnetic moment. If we consider GGA results, LDOS spin up branches of Mn and Ni in austenite overlay very well around -1 eV and their shapes are even more alike around -3.5 eV which suggests strong interaction of these orbitals. The situation in martensite is somewhat more complex due to further d orbital splitting in the tetragonal crystal field however shape and peak distribution of both LDOS remain similar. Overall shape of DOS and presence of the pseudogap hint towards some degree of covalent bonding in this alloy.

The use of U on Ni atoms results in wider pseudogap in spin down DOS channel what is in austenite accompanied by shift of the Ni peak directly on the Fermi level causing instability of the cubic phase. Also in NM martensite ($c/a = 1.19$) the psedogap is wider compared to GGA what agrees with pronounced stability of the martensite phase. The spin up branch of Ni LDOS is affected only slightly, peaks situated above -4 eV in GGA are slightly shifted towards lower energies. Mn states are mostly unaffected only peaks around -1.5 eV possess somewhat higher DOS.

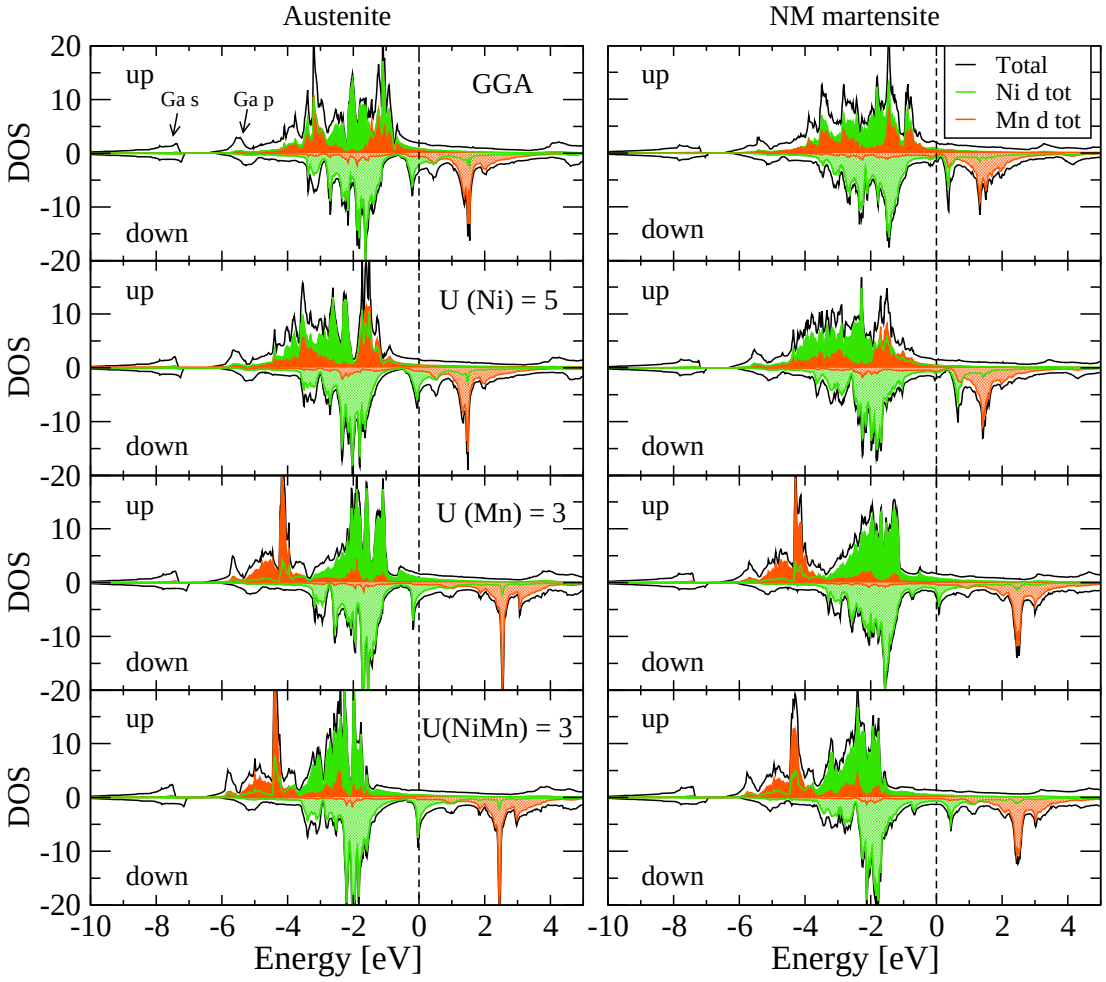

Figure 3.16: Effect of U correction on DOS and LDOS when applied to different atoms. In all cases U = 3 eV apart from GGA where U = 0 eV. Martensite in all cases has $c/a > 1$. LDOS of Ga is left out because of its low contribution in selected energy range.

In the case of correction on Mn *d* electrons, strong exchange splitting of Mn states is apparent since the energy difference between two main peaks in up and down branches increases to around 6.5 eV. This and lower LDOS in the spin down branch cause increase of local magnetic moment of Mn atoms calculated using this setup. Ni states are changed in smaller extend, we can see redistribution of their spin up peaks towards higher energies which creates an energy gap at -3.5 eV in both austenite and martensite. Resulting DOS consists of almost two separate energy levels of Mn and Ni. This distinct localization of Mn electrons probably weakens the Mn-Ni interaction. The tetragonal distortion doesn't sufficiently shift the Ni spin down peak above E_F. This is related with predicted of metastable NM martensite for U (Mn) = 3 eV.

The third implementation of U uses the correction on both Mn and Ni. We can see a joint effect of separate correction use, apparent is localization of both Ni and Mn LDOS, the exchange splitting of Mn states is even a little bit stronger that in the case

of U on Mn. The spin down Ni peak is completely shifted above E_F thanks to the tetragonal distortion which results in stable NM martensite.

3.4.1. Bond analysis

The shortest inter-atomic distances in Ni_2MnGa are between Ni and either one of Mn or Ga. Nickel atoms can be considered as being positioned within a tetrahedral interstitial position of Mn and Ga sublattices. The length of these two bonds in austenite is 2.51 Å compared to the lattice vector a = 5.80 Å (both GGA). Second shortest neighbours are Mn-Ga and Ni-Ni atoms distanced 2.90 Å (GGA). Formation of Ni_2MnGa causes the charge redistribution between sublattices, Ga becomes an anion with charge equal to -1.44 per atom that is donated by Mn (+0.62/atom) and Ni (+0.41/atom). This is caused by tendency of Ga to half-fill its $4p$ orbitals with $4s$ electrons donated mostly from other two constituents. These circumstances suggest some degree of hybridization of Ga s and p orbitals that are involved in bonding and partially ionic interaction with other two components. Calculated Mulliken and Löwdin charges are almost equal therefore we don't distinguish them in this case.

Overlap of crystal orbitals is qualified by the COOP function in Figure 3.17, calculated with GGA (without U). In the case of magnetically ordered materials the DOS is no longer degenerate for both electron spins and we have to distinguish between up and down channels. Due to this also COOP or COHP split into up and down contributions. Figure 3.17 shows large antibonding overlap in both spin channels of all four shortest interactions. The shape of DOS and COOP curves indicates partially covalent character of these bonds. We can see strong antibonding regions in all four bonds which lowers the ICOOP close to zero or even to negative values in some cases. The spin down DOS peak at E_F that destabilizes austenite corresponds to antibonding Ni-Ni interaction of e_g orbitals arising from the octahedral crystal field. This orbital consists of degenerate $d_{x^2-y^2}$ and d_{z^2}. As mentioned before, the tetragonal distortion shifts this peak above E_F what lowers the amount of antibonding interactions in the material that is a sign of higher stability.

Four shortest bonds were analyzed using COHP similarly to the section on transition metal diborides. Results obtained with different U application are summarized in Figure 3.18 - 3.21. COHP curves calculated without the U correction are summarized alongside DOS and DOE in Figure 3.18. The most stabilizing hence the strongest interaction is formed between Ni and Ga atoms (see Figure 3.22). The broad metallic like COHP stabilizing interaction in Ni-Ga between -7 and -10 eV is composed mainly of Ga s interacting with Ni s and a small portion of Ni d electrons. Second bonding peak present in both spin channels at -5.5 eV consists mainly of Ga p interacting with Ni s and d orbitals. Interactions below -3.5 eV are bonding in COOP as well, on the other hand for higher energies COOP predicts antibonding interactions in both spins. This is not the case in COHP at least in the spin up channel where these states are

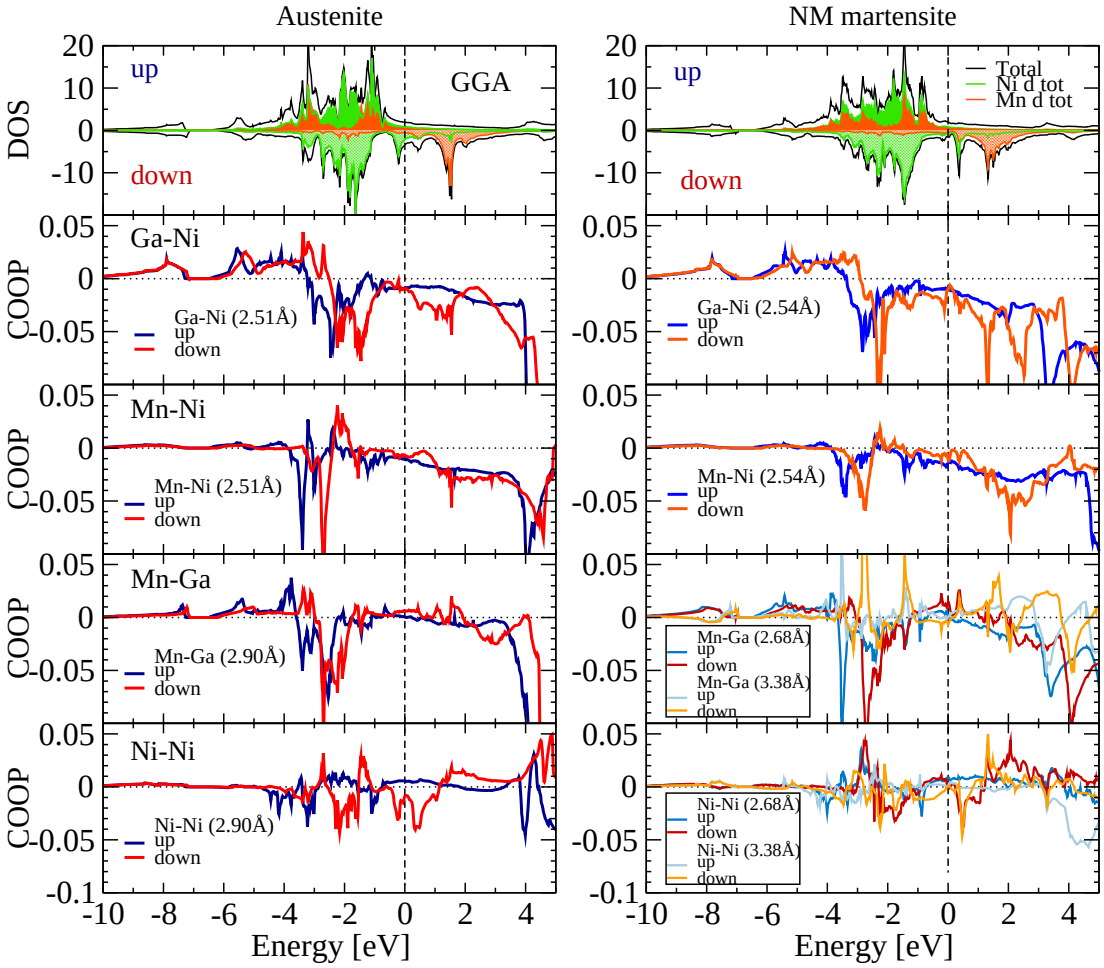

Figure 3.17: COOP curves of four shortest interactions in Ni_2MnGa. Calculated without U correction.

mostly non-bonding i.e. their interaction does not contribute to the band energy and has no effect on stability of the structure. Physically wave functions of these electrons have antibonding overlap but they do not interact strongly. In the spin down channel there are destabilizing contributions above -3 eV that are identical to the DOS region around the pseudogap. Formation of the pseudogap seems to be closely related to Ga-Ni interaction. In martensite destabilizing portion of COHP in Ga-Ni bond is decreased. The antibonding peak, positioned at E_F in austenite, also contains significant Ni-Ni destabilizing contribution. The tetragonal deformation shifts this peak over the Fermi level what lowers the number of occupied destabilizing states. In austenite, all three interactions that contain Ni have destabilizing contributions below E_F. This might also be the reason why increasing concentration of Ni in off-stoichiometric alloys results in higher martensite transformation temperature due to further destabilization of austenite. On the other hand, lower concentration of Ni should result in lower amount of destabilizing interactions which stabilize the cubic phase [101].

Stabilizing interactions identified by COPH in Mn-Ni and Mn-Ga bonds are partially antibonding according to COOP. In the Mn-Ga interaction there is stabilizing interaction on E_F that is mainly in NM martensite a very distinct bonding peak just above the Fermi level. This interaction is formed between Mn and Ga atoms that are brought closet to each other after the deformation. It is probable that small increase of Mn and Ga concentration (more Mn since its contribution to this peak is stronger) should cause the transformation temperature to grow. Indeed the offstoichiometric alloy with excess of Mn has higher T_M and replacement of Ni with Ga also affects T_M in a positive way [101]. Mn-Ni bond seems to be the most metallic one according to COHP function shape.

Figure 3.19 shows the situation when U = 3 eV was applied to Ni electrons. As already mentioned, U on Ni widens the pseudogap in the spin down channel what is said to be related to a stronger covalency. The COHP curves are mostly similar to the GGA

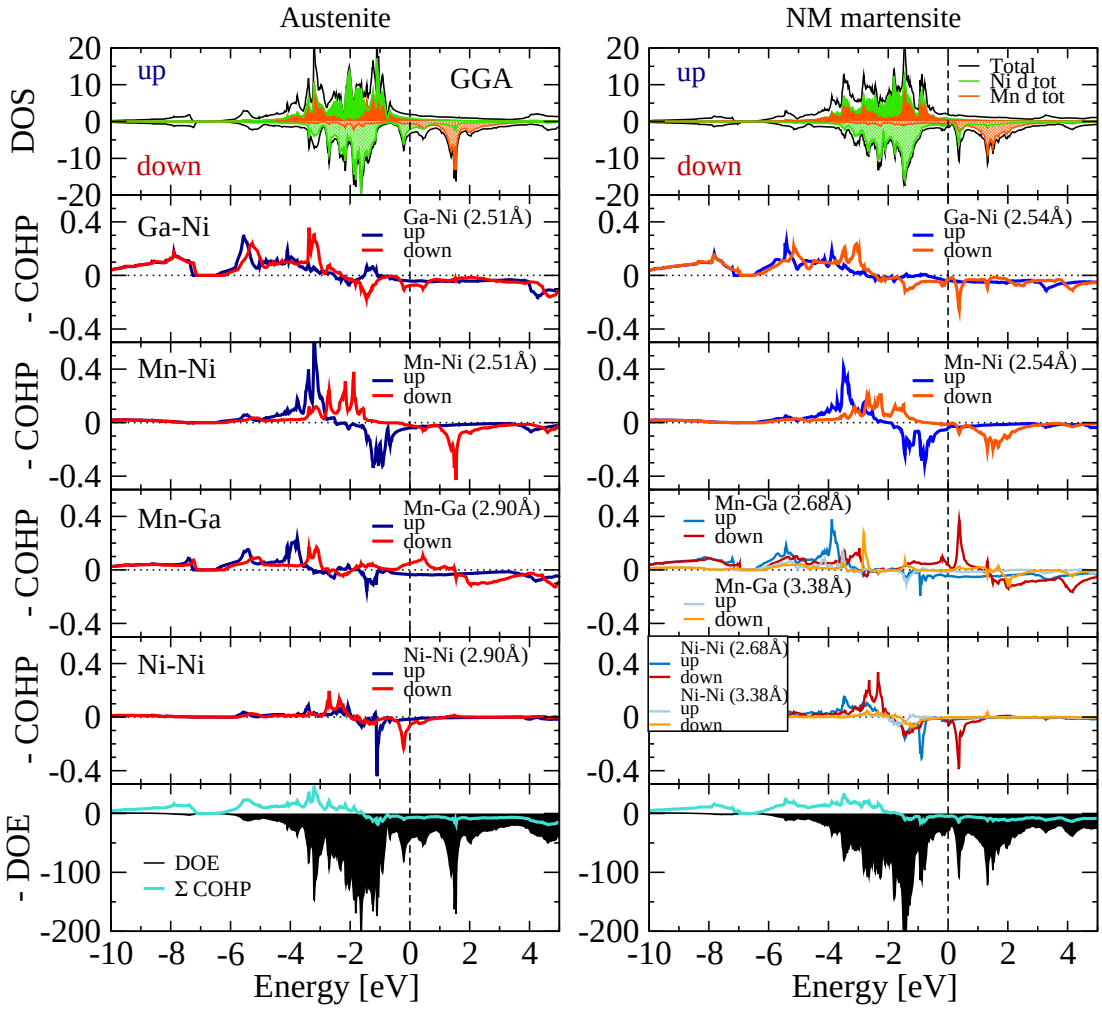

Figure 3.18: DOS, DOE and COHP of four shortest interactions in austenite and NM martensite using GGA. DOE and summed COHP are sums of spin up and spin down contributions. Summed COHP is multiplied by the factor of 2.

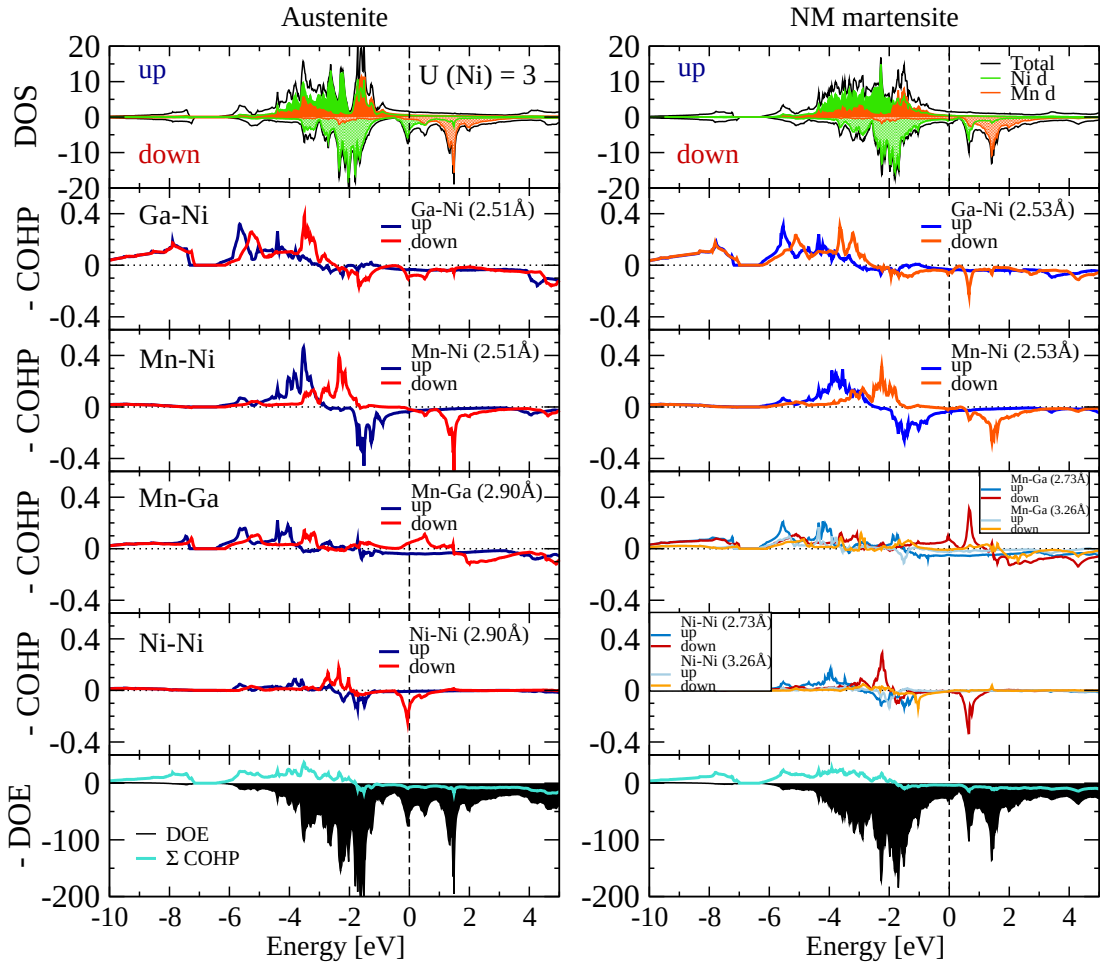

Figure 3.19: COHP curves of four shortest bonds calculated with U = 3 eV on Ni, compared with DOS and DOE functions. NM martensite corresponds to a stable minimum at $c/a = 1.19$. Summed COHP is multiplied by the factor of 2.

case. The antibonding region around the pseudogap (spin down) in austenite within Ga-Ni interaction is slightly less destabilizing than in GGA. Also Mn-Ga interaction have less destabilizing effect in the spin up channel around -1.5 eV. The same can be said about Ni-Ni destabilizing interactions around -2 eV. The only clue hinting towards destabilization of austenite is the antibonding peak in Ni-Ni interaction that is present precisely of E_F. In martensite all interactions have less destabilizing character compared to simple GGA.

Situation in Figure 3.20 represents calculation with correction U = 3 eV on *d* electrons of Mn. The gap is formed in spin up channel of Ga-Ni interaction between bonding states at -4 eV what is exactly where the big Mn peak in DOS is positioned. At the same energy a large peak is present in Mn-Ni bond. Ni electrons that were in GGA employed in Ga-Ni bond are redistributed and interact almost solely with Mn orbitals in this energy range. This preferential interaction with Ni is caused by the strong exchange splitting that moves spin up LDOS of Mn to more negative energies which is accompa-

nied by the non-bonding region in Ga-Ni bond at this energy. As Figure 3.15c shows the stable structure in this case is cubic austenite and NM martensite is a metastable structure. The evidence of this behavior is the antibonding Ni-Ni peak directly at E_F in NM martensite.

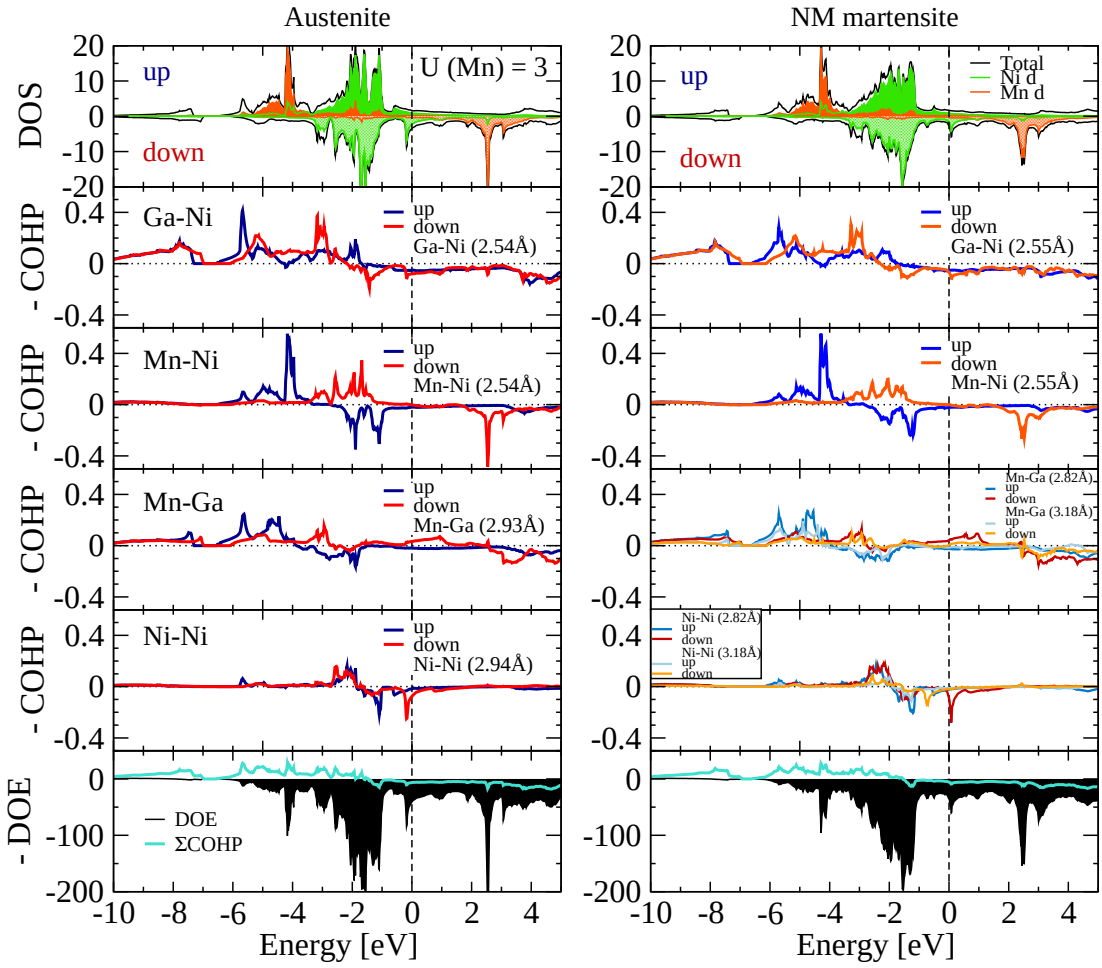

Figure 3.20: COHP curves of four shortest bonds calculated with U = 3 eV on Mn, compared with DOS and DOE. NM martensite at this value of U is metastable. Summed COHP is multiplied by the factor of 2.

Figure 3.21 shows results of the COHP analysis computed with the use of U = 3 eV on both Ni and Mn at the same time. As expected, U (Ni&Mn) produces results that are a combination of U (Ni) and U (Mn). In the case of Ga-Ni bond in austenite, the effect of U on Ni is smoothens the sharp destabilizing peak in spin down channel around -1.5 eV, U on Mn creates a gap between stabilizing states in the spin up channel around -4.5 eV. Mn-Ni interaction in austenite has localized stabilizing peak in the spin down channel thanks to U on Ni and large localized and stabilizing peak in the spin up channel just above -4.5 eV due to U on Mn. Destabilizing interaction is introduced

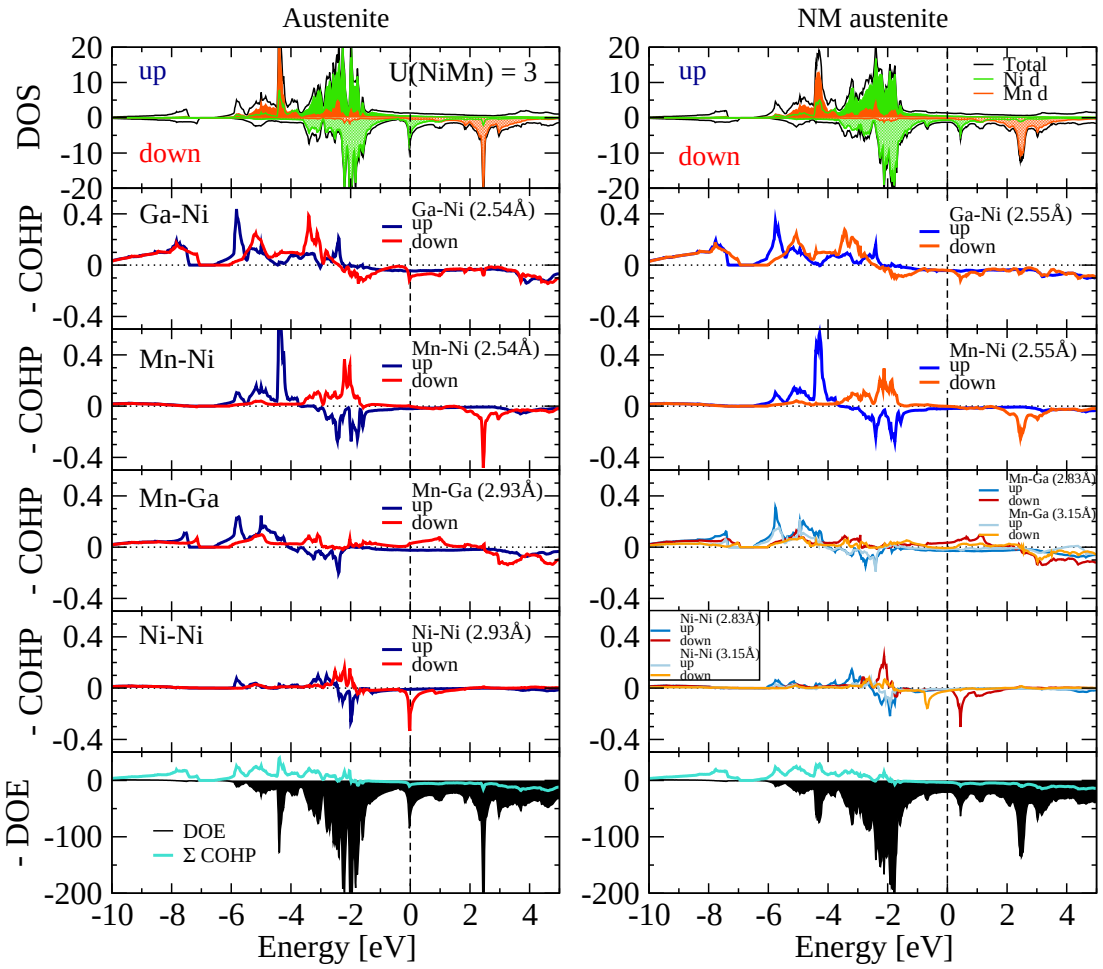

Figure 3.21: COHP curves of four shortest bonds calculated with U = 3 eV on Ni and Mn, compared with DOS and DOE functions. NM martensite corresponds to a stable minimum at $c/a = 1.11$. Summed COHP is multiplied by the factor of 2.

in the spin up channel of Mn-Ga interaction as an effect of U on Mn. The Ni-Ni interaction is affected almost solely by U on Ni, it moves the destabilizing spin up peak to lower energies as well as spin down destabilizing peak to higher energies (to E_F) which destabilizes austenite. In martensite we can distinguish more or less the same trends as in austenite. The stability of NM martensite according to the austenite is lower when using U (Ni&Mn) than in the case of U on Ni which can be seen in Figure 3.15a and 3.15e. This is caused by the Ni-Ni antibonding peak in NM martensite close below the Fermi level (around -1 eV) when using U (Ni&Mn).

All four bonds calculated with different setup are compared within Appendix B. From the analysis above, we conclude that localization on either Ni or Mn mostly affects interactions in which corrected atom doesn't participate. In the case of U on Ni, Mn-Ni interaction becomes more metallic and Mn-Ga more covalent. When we used U on Mn, Ga-Ni became more covalent, Mn-Ni less metallic and Ni-Ni more metallic. In general, the martensitic transformation decreases destabilizing contributions in inter-

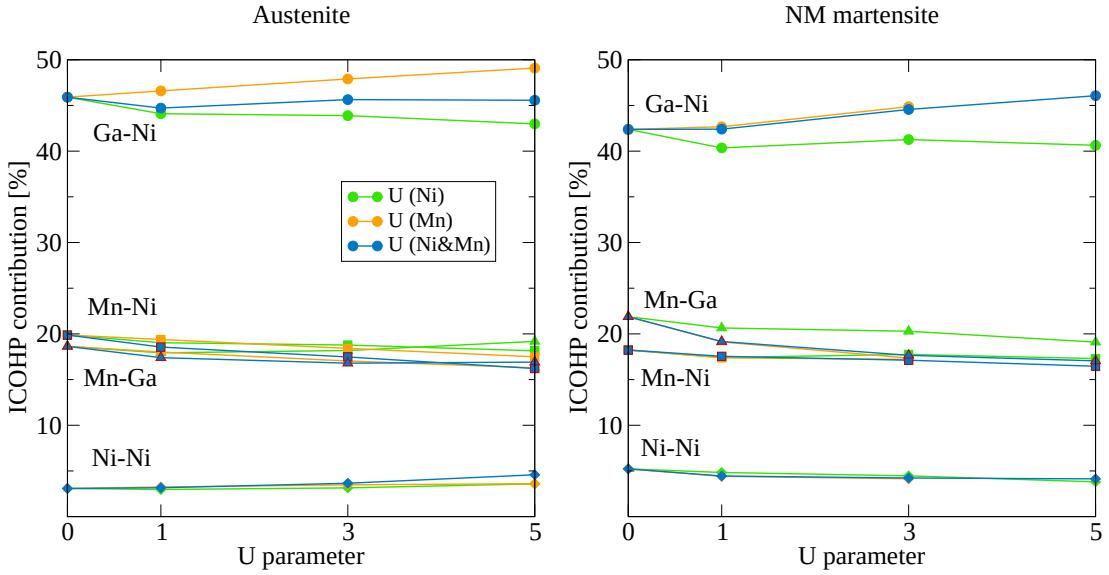

Figure 3.22: ICOHP as a function of U parameter. Martensite calculated with U (Mn) has only three points since it becomes unstable at U (Mn) = 5 eV.

actions and COHP curves become smoother what hints towards less covalent character in NM martensite.

According to ICOHP analysis, the strongest (the most energy stabilizing) is the shortest Ga-Ni bond in both cubic and tetragonal phase. Mn-Ni interaction follows as a little bit stronger than Mn-Ga and the weakest is the Ni-Ni bond (Figure 3.22). When U is used on Ni, the strongest Ga-Ni bond slightly weakens in austenite with increasing U which is to some extend balanced by Mn-Ga bond that for U (Ni) = 5 eV becomes stronger than Mn-Ni. In the case of U on Mn, the Ga-Ni bond gets stronger with increasing U at expense of Mn-Ni and Mn-Ga bonds that become weaker. Difference in martensite is that GGA predicts Mn-Ga interaction to be stronger than Mn-Ni, also Ni-Ni bond slightly weakens with increasing U in all cases.

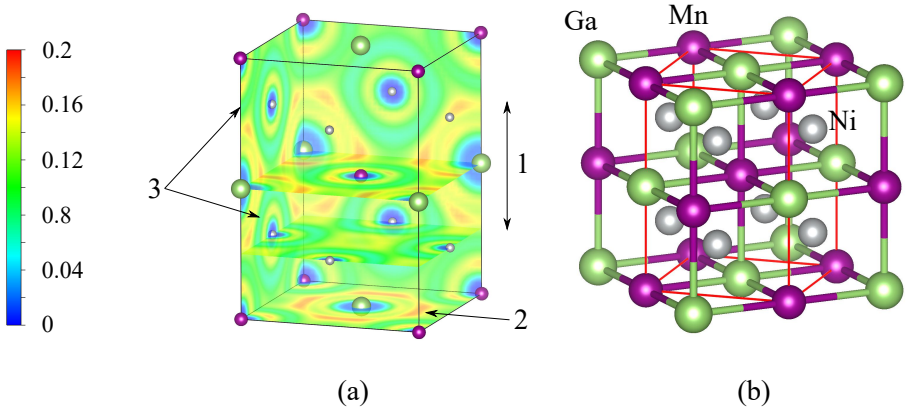

Figure 3.23: a) ELF map calculated using GGA functional, b) unit cell with computational tetragonal cell marked by red lines.

3.4.2. Electron localization analysis

In this section we compare ELF maps of Ni_2MnGa alloy obtained with GGA and Hubbard correction to the electronic structure. In Figure 3.23a is shown the ELF map in computational cell as calculated by uncorrected GGA. Relation of the tetragonal computational cell to the conventional unit cell is pointed out in Figure 3.23b. According to the ELF distribution the largest space with high electron localization is around Ga atoms (arrow 1). Around Mn atoms the higher localization is pointing towards next Ga atoms. This is caused partly by the size of Ga atoms (filled $3d$ shell) and partly by electrons transfer from Mn and Ni. The highest electron localization is also around Ga atoms, peaking in (001) plane towards Mn atoms (arrow 2). Electron localization around Ni and Mn atoms is almost spherical with region of low localization around them (arrow 3) that is mostly uniform in all directions.

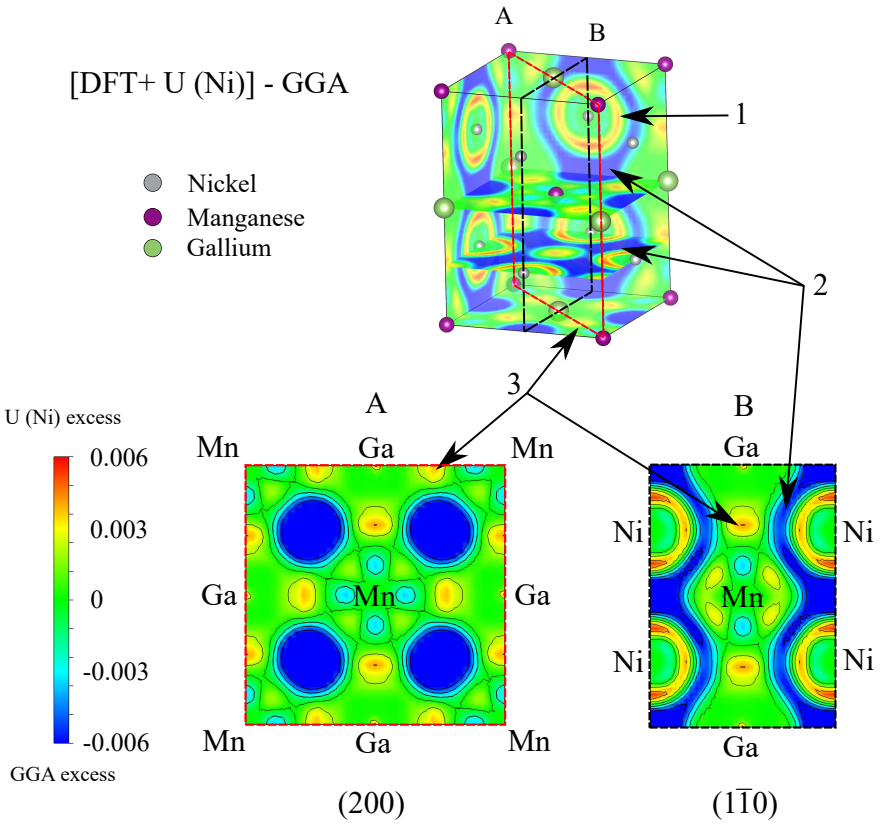

Figure 3.24: ELF difference map, ELF of GGA is subtracted from EFL of DFT+ U with correction U = 3 eV on Ni.

The difference between ELF calculated using U (Ni) = 3 eV and GGA is shown in Figure 3.24. Red regions describe higher electron localization in ELF calculated with U on Ni, on the contrary in blue regions the localization is stronger in GGA result. Higher localization around Ni atoms (arrow 1) can be expected from the nature of DFT+ U method. Localization between Ni atoms in all directions is lower in the corrected

calculation (arrow 2) that suggests less metallic interaction. Higher localization in corrected calculation is between Mn and Ga (arrow 3). Figure 3.22 presents bond strength changes due to Hubbard corrective approach. We can see that in the case of U on Ni interactions Ga-Ni and Mn-Ni become weaker, presumably due to localization of Ni *d* electrons. Contrarily, Mn-Ga interaction becomes more stabilizing and stronger. Charge difference maps can be found in Appendix C.

Figure 3.25 captures electron localization difference between U (Mn) = 3 eV and GGA calculation. In this case localization is higher around Mn atoms (arrow 1) that at the same time are separated from other atoms by the region of lower electron localization (arrow 2) what seems to have effect on Mn-Ga bond that weakens with increasing U on Mn. Localization is in the corrected case higher between Ga and Ni (arrow 3). Both strengthening of Ga-Ni bond and weakening of Mn-Ga bond are supported by Figure 3.22 ICOHP comparison. Both U (Mn) and U (Ni) correction seem to strengthen bonds in which participate atoms that are not corrected. An exception is Ni-Ni interaction strength of which is unaffected by the U parameter. Contrary to U (Ni), localization of Mn electrons has effect on charge distribution among atoms. In the case of U (Mn) = 3 eV, according to Mulliken population analysis, Ga accepts more electrons (with charge -1.51/atom) than what GGA predicts donated mainly by Mn (+0.78/atom) and partially by Ni (+0.36/atom).

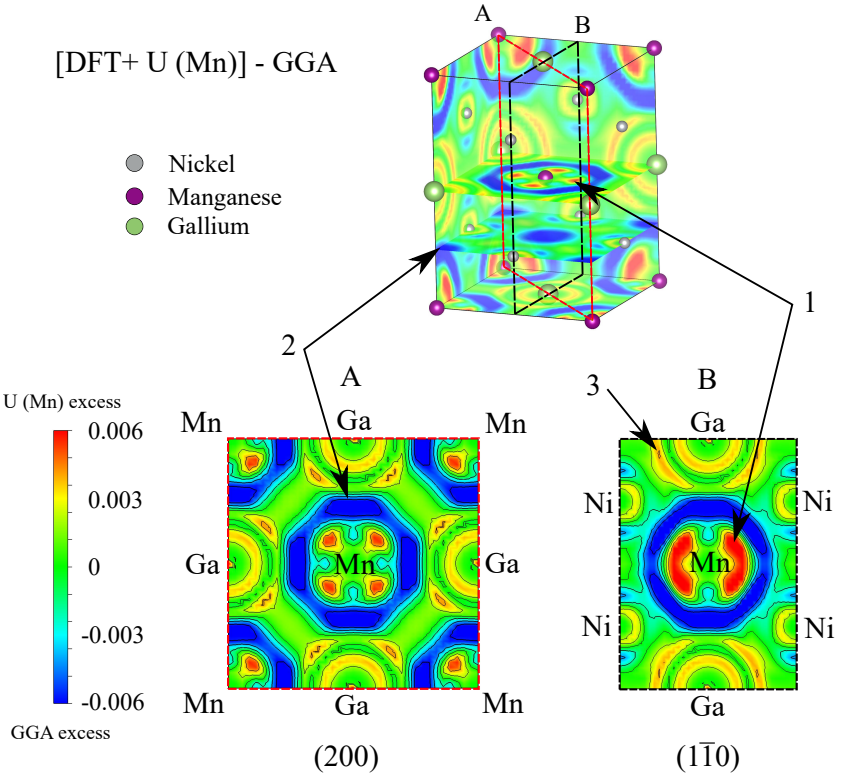

Figure 3.25: ELF difference map, ELF of GGA is subtracted from EFL of DFT+ U with correction U = 3 eV on Mn.

Conclusions

This master's thesis dealt with an analysis of inter-atomic interactions in selected progressive materials with wide application possibilities. All presented results were obtained using the planewave based VASP code utilizing the *ab initio* calculations approach. Interactions and bonds in studied structures were characterized and compared within the scope of COHP, COOP and DOS functions that are accessible through the application of the LOBSTER package, compatible with optimized electronic structure calculated by VASP. Described methodology was applied to diborides of transition metals from groups 4 - 7 and to Ni_2MnGa Heusler alloy.

In all diborides there are two main bonds responsible for cohesion - the strongest boron-boron covalent bond and metal-boron covalent bond with ionic contribution. The first bond mediates formation of hexagonal layer of boron and the second one keeps metal and boron layers together. The creation of a diboride is accompanied with a charge transfer from transition metal to boron that to a large extent affects atomic interactions. Large charge transfer to boron atoms supports strong B-B interaction due to additional π bonding, lower charge transfer strengthens metal-boron bond. Lower charge transfer from transition metal also makes metal-metal interaction stronger.

Reaction of diborides to shear deformation as well as to elongation and compression alond the c lattice vector was discussed according to energetic demandingness of these deformation modes. The most difficult to shear along the basal lattice vector is TiB_2 and other group 4 and group 5 transition metal diborides. Shear deformation does not distort B-B in plane bond and should hint towards TM-B bond strength. We can see that shear deformation weakens B-B interaction and at the same time supports stability of averaged TM-B interaction which is related to lowered electron transfer from metal atoms in sheared structures. In compression and tension we deform both bonds parallel and perpendicular to the direction of elongation or compression. Group 4 and 5 transition metal diborides are the most difficult to compress, that means shrinkage of TM-B and elongation of B-B bonds is difficult. On the other hand, the most difficult to deform in tension, that means elongation of TM-B and compression of B-B bonds, are ReB_2 and TcB_2.

Ni_2MnGa alloy was studied using DFT + U corrective approach with U on Ni and Mn. The Hubbard model was compared with uncorrected GGA to understand effects of electron localization on structure and bonding. The effect of U on Ni resides in destabilization of cubic austenite and stabilization of NM martensite. Correction of Ni d electrons results in the prediction of a new metastable structure with $c/a < 1$. On the other hand, application of U on Mn strongly destabilizes NM martensite. With U = 3 eV on Mn is austenite more sable than NM martensite. Hubbard correction applied on both Ni and Mn mostly resembles the case with U on Ni. U correction increases net magnetic moment in all examined combinations. We conclude that correction of Ni electrons affects structural stability and magnetic properties more than modification of

Mn electronic structure therefore we can say that the role of Ni in the alloy is more important than of Mn concerning some properties.

COHP analysis of inter-atomic interactions detected Ni-Ga as the most stabilizing hence the strongest bond within this alloy. The character of COHP and COOP functions calculated for four shortest interactions (Ga-Ni, Mn-Ni, Mn-Ga, Ni-Ni) suggests that Ga-Ni and Ni-Ni bonds are mostly covalent. The most metallic character has Mn-Ni interaction. The spin down peak near the Fermi level usually explained as a result of Jahn-Teller effect responsible for destabilization of austenite is composed of antibonding Ni-Ni and Ni-Ga interactions. Enhanced localization of Ni electrons moves this peak closer to E_F in austenite what causes its destabilization. Application of U on Ni promotes metallic character of Mn-Ni, U on Mn increases covalent charactrer of Mn-Ni interaction and metallic character of Ni-Ni interaction. Enhanced localization of Mn or Ni *d* electrons strengthens bonds in which corrected atoms do not participate.

Bibliography

[1] P. Hohenberg and W. Kohn, "Inhomogeneous electron gas", *Physical review*, vol. 136, no. 3B, B864, 1964.

[2] E. Schrödinger, "Quantisation as a problem of characteristic values", *E. Ann. Phys*, vol. 79, pp. 361–376, 1926.

[3] J. J. Sakurai and E. D. Commins, *Modern quantum mechanics, revised edition*. Addison-Wesley Publishing Company, 1995, ISBN: 0-201-53929-2.

[4] M. Born, "Das adiabatenprinzip in der quantenmechanik", *Zeitschrift für Physik*, vol. 40, no. 3-4, pp. 167–192, 1927.

[5] P. A. M. Dirac, *The principles of quantum mechanics*, 4th ed. Oxford university press, Oxford, 1981, ISBN: 0 19 852011 5.

[6] R. Martin, *Electronic Structure - Basic Theory and Practical Methods*. 2004, ISBN: 0 521 78285 6.

[7] K. A. Olive, "Review of particle physics", *Chinese physics C*, vol. 38, no. 9, pp. 090 001–090 001, 2014.

[8] M. Born and R. Oppenheimer, "Zur quantentheorie der molekeln", *Annalen der physik*, vol. 389, no. 20, pp. 457–484, 1927.

[9] C. J. Cramer, *Essentials of computational chemistry: theories and models*, 2nd ed. John Wiley & Sons, Chichester, 2013, ISBN: 0-470-09181-9.

[10] C. Kittel, *Introduction to Solid State Physics*, 8th ed. John Wiley & Sons, New York, 2005, ISBN: 0-471-68057-5.

[11] S. H. Simon, *The Oxford solid state basics*. Oxford University Press, Oxford, 2013, ISBN: 978-0-19-968076-4.

[12] I. N. Levine, D. H. Busch, and H. Shull, *Quantum chemistry*, 7th ed. Pearson Education, Upper Saddle River, NJ, 2014, ISBN: 0-321-80345-0.

[13] J. Katriel and R. Pauncz, "Theoretical interpretation of Hund's rule", in *Advances in quantum chemistry*, vol. 10, Elsevier, 1977, pp. 143–185.

[14] T. Oyamada, K. Hongo, Y. Kawazoe, and H. Yasuhara, "Unified interpretation of Hunds first and second rules for 2p and 3p atoms", *The Journal of chemical physics*, vol. 133, no. 16, p. 164 113, 2010.

[15] J. N. Lalena, D. A. Cleary, and O. B. H. Duparc, *Principles of inorganic materials design*. John Wiley & Sons, Hoboken, NJ, 2010, ISBN: 987-0-470-40403-4.

[16] D. R. Hartree, "The waves mechanics of an atom with non-coulombic central field", in *Proc. Cambridge Phil. Soc*, vol. 24, 1928, p. 111.

[17] A. Szabo and N. S. Ostlund, *Modern quantum chemistry: introduction to advanced electronic structure theory*. Dover Publications, Mineola, 1996, ISBN: 0-486-69186-1.

[18] N. D. Mermin, "Thermal properties of the inhomogeneous electron gas", *Physical Review*, vol. 137, no. 5A, A1441, 1965.

[19] W. Kohn and L. J. Sham, "Self-consistent equations including exchange and correlation effects", *Physical review*, vol. 140, no. 4A, A1133, 1965.

[20] F. J. Torres, L. Rincón, C. Zambrano, J. R. Mora, and M. Méndez, "A review on the information content of the pair density as a tool for the description of the electronic properties in molecular systems", *International Journal of Quantum Chemistry*, vol. 119, no. 2, e25763, 2019.

[21] T. M. Henderson, B. G. Janesko, and G. E. Scuseria, "Generalized gradient approximation model exchange holes for range-separated hybrids", *The Journal of chemical physics*, vol. 128, no. 19, p. 194 105, 2008.

[22] J. Toulouse, *Introduction to density-functional theory*, lecture notes, 2015.

[23] N. Harrison, "An introduction to density functional theory", *Nato Science Series Sub Series III Computer and Systems Sciences*, vol. 187, pp. 45–70, 2003.

[24] D. M. Ceperley and B. J. Alder, "Ground state of the electron gas by a stochastic method", *Physical Review Letters*, vol. 45, no. 7, p. 566, 1980.

[25] F. Herman, J. P. Van Dyke, and I. B. Ortenburger, "Improved statistical exchange approximation for inhomogeneous many-electron systems", *Physical Review Letters*, vol. 22, no. 16, p. 807, 1969.

[26] A. D. Becke, "Density-functional exchange-energy approximation with correct asymptotic behavior", *Physical review A*, vol. 38, no. 6, p. 3098, 1988.

[27] C. Lee, W. Yang, and R. Parr, "Density-functional exchange-energy approximation with correct asymptotic behaviour", *Phys. Rev. B*, vol. 37, pp. 785–789, 1988.

[28] K. Burke, J. P. Perdew, and Y. Wang, "Derivation of a generalized gradient approximation: The PW91 density functional", in *Electronic density functional theory*, Springer, 1998, pp. 81–111.

[29] J. P. Perdew, K. Burke, and M. Ernzerhof, "Generalized gradient approximation made simple", *Physical review letters*, vol. 77, no. 18, p. 3865, 1996.

[30] V. Anisimov and O. Gunnarsson, "Density-functional calculation of effective Coulomb interactions in metals", *Physical Review B*, vol. 43, no. 10, p. 7570, 1991.

[31] V. I. Anisimov, J. Zaanen, and O. K. Andersen, "Band theory and Mott insulators: Hubbard U instead of Stoner I", *Physical Review B*, vol. 44, no. 3, p. 943, 1991.

[32] I. Solovyev, P. Dederichs, and V. Anisimov, "Corrected atomic limit in the local-density approximation and the electronic structure of d impurities in Rb", *Physical Review B*, vol. 50, no. 23, p. 16 861, 1994.

[33] B. Himmetoglu, A. Floris, S. De Gironcoli, and M. Cococcioni, "Hubbard-corrected DFT energy functionals: The LDA+ U description of correlated systems", *International Journal of Quantum Chemistry*, vol. 114, no. 1, pp. 14–49, 2014.

[34] M. Cococcioni, "The LDA+ U approach: A simple Hubbard correction for correlated ground states", *Correlated Electrons: From Models to Materials Modeling and Simulation; Verlag des Forschungszentrum Jülich: Jülich, Germany*, 2012.

[35] S. A. Tolba, K. M. Gameel, B. A. Ali, H. A. Almossalami, and N. K. Allam, "The DFT+ U: Approaches, accuracy, and applications", *Density Functional Calculations: Recent Progresses of Theory and Application*, p. 1, 2018.

[36] A. Liechtenstein, V. I. Anisimov, and J. Zaanen, "Density-functional theory and strong interactions: Orbital ordering in Mott-Hubbard insulators", *Physical Review B*, vol. 52, no. 8, R5467, 1995.

[37] S. Dudarev, G. Botton, S. Savrasov, C. Humphreys, and A. Sutton, "Electron-energy-loss spectra and the structural stability of nickel oxide: An LSDA+ U study", *Physical Review B*, vol. 57, no. 3, p. 1505, 1998.

[38] M. Cococcioni and S. De Gironcoli, "Linear response approach to the calculation of the effective interaction parameters in the LDA+ U method", *Physical Review B*, vol. 71, no. 3, p. 035 105, 2005.

[39] E. Şaşıoğlu, C. Friedrich, and S. Blügel, "Effective Coulomb interaction in transition metals from constrained random-phase approximation", *Physical Review B*, vol. 83, no. 12, p. 121 101, 2011.

[40] *Pseudopotential*, https://upload.wikimedia.org/wikipedia/commons/f/fb/Sketch_Pseudopotentials.png, Accessed: 2020-10-22.

[41] P. E. Blöchl, J. Kästner, and C. J. Först, "Electronic structure methods: Augmented waves, pseudopotentials and the projector augmented wave method", in *Handbook of Materials Modeling*, Springer, 2005, pp. 93–119.

[42] E. J. Bylaska, "Plane-wave DFT Methods for Chemistry", in *Annual Reports in Computational Chemistry*, vol. 13, Elsevier, 2017, pp. 185–228.

[43] P. E. Blöchl, "Projector augmented-wave method", *Physical review B*, vol. 50, no. 24, p. 17 953, 1994.

[44] C. Rostgaard, *The projector augmented-wave method*, textbook, 2009.

[45] P. E. Blöchl, C. J. Först, and J. Schimpl, "Projector augmented wave method: Ab initio molecular dynamics with full wave functions", *Bulletin of Materials Science*, vol. 26, no. 1, pp. 33–41, 2003.

[46] C. C. J. Roothaan, "New developments in molecular orbital theory", *Reviews of modern physics*, vol. 23, no. 2, p. 69, 1951.

[47] R. Dronskowski, *Computational chemistry of solid state materials*, 1st ed. Wiley-VCH, Weinheim, 2005, ISBN: 3-527-31410-5.

[48] R. S. Mulliken, "Electronic structures of molecules X. Aldehydes, Ketones and Related Molecules", *The Journal of Chemical Physics*, vol. 3, no. 9, pp. 564–573, 1935.

[49] R. S. Mulliken, "Overlap populations, bond orders and covalent bond energies", *J. chem. Phys*, vol. 23, pp. 1841–1846, 1955.

[50] P.-O. Löwdin, "On the non-orthogonality problem connected with the use of atomic wave functions in the theory of molecules and crystals", *The Journal of Chemical Physics*, vol. 18, no. 3, pp. 365–375, 1950.

[51] P. O. Löwdin, "On the nonorthogonality problem", in *Advances in quantum chemistry*, vol. 5, Elsevier, 1970, pp. 185–199.

[52] J. K. Desmarais, A. Erba, and R. Dovesi, "Generalization of the periodic LCAO approach in the CRYSTAL code to g-type orbitals", *Theoretical Chemistry Accounts*, vol. 137, no. 2, p. 28, 2018.

[53] S. Steinberg and R. Dronskowski, "The crystal orbital Hamilton population (COHP) method as a tool to visualize and analyze chemical bonding in intermetallic compounds", *Crystals*, vol. 8, no. 5, p. 225, 2018.

[54] R. Dronskowski and P. E. Blöchl, "Crystal orbital hamilton populations (COHP): Energy-resolved visualization of chemical bonding in solids based on density-functional calculations", *The Journal of Physical Chemistry*, vol. 97, no. 33, pp. 8617–8624, 1993.

[55] M. Küpers, P. M. Konze, S. Maintz, *et al.*, "Unexpected GeGe contacts in the two-dimensional Ge4Se3Te phase and analysis of their chemical cause with the density of energy (DOE) function", *Angewandte Chemie International Edition*, vol. 56, no. 34, pp. 10 204–10 208, 2017.

[56] R. Nelson, P. M. Konze, and R. Dronskowski, "First-principles chemical bonding study of manganese carbodiimide, MnNCN, as compared to manganese oxide, MnO", *The Journal of Physical Chemistry A*, vol. 121, no. 40, pp. 7778–7786, 2017.

[57] S. Maintz, V. L. Deringer, A. L. Tchougréeff, and R. Dronskowski, "LOBSTER: A tool to extract chemical bonding from plane-wave based DFT", *Journal of computational chemistry*, vol. 37, no. 11, pp. 1030–1035, 2016.

[58] S. Maintz, V. L. Deringer, A. L. Tchougréeff, and R. Dronskowski, "Analytic projection from plane-wave and paw wavefunctions and application to chemical-bonding analysis in solids", *Journal of computational chemistry*, vol. 34, no. 29, pp. 2557–2567, 2013.

[59] V. L. Deringer, A. L. Tchougréeff, and R. Dronskowski, "Crystal orbital hamilton population (COHP) analysis as projected from plane-wave basis sets", *The journal of physical chemistry A*, vol. 115, no. 21, pp. 5461–5466, 2011.

[60] F. H. Pollard and P. Woodward, "The stability and chemical reactivity of titanium nitride and titanium carbide", *Transactions of the Faraday Society*, vol. 46, pp. 190–199, 1950.

[61] D. Fister, "Über den einfluss der unterkohlung der hartstoffphase auf die eigenschaften von TiC-VC (TaC, NbC)-Mo2C-Ni und über die beschichtung von hartmetallplatten mit titannitrid, Doctoral Thesis", *Technische Hochschule Wien*, 1970.

[62] S. Zhang and W. Zhu, "TiN coating of tool steels: A review", *Journal of Materials Processing Technology*, vol. 39, no. 1-2, pp. 165–177, 1993.

[63] S. PalDey and S. Deevi, "Single layer and multilayer wear resistant coatings of (Ti, Al) N: A review", *Materials Science and Engineering: A*, vol. 342, no. 1-2, pp. 58–79, 2003.

[64] H. Caliskan, P. Panjan, and C. Kurbanoglu, "Hard coatings on cutting tools and surface finish", 2017.

[65] O. Knotek, M. Böhmer, and T. Leyendecker, "On structure and properties of sputtered Ti and Al based hard compound films", *Journal of Vacuum Science & Technology A: Vacuum, Surfaces, and Films*, vol. 4, no. 6, pp. 2695–2700, 1986.

[66] A. Hörling, L. Hultman, M. Odén, J. Sjölén, and L. Karlsson, "Mechanical properties and machining performance of $Ti_{1-x}Al_xN$-coated cutting tools", *Surface and Coatings Technology*, vol. 191, no. 2-3, pp. 384–392, 2005.

[67] W. Kalss, A. Reiter, V. Derflinger, C. Gey, and J. Endrino, "Modern coatings in high performance cutting applications", *International Journal of Refractory Metals and Hard Materials*, vol. 24, no. 5, pp. 399–404, 2006.

[68] J. Musil and H. Hrubý, "Superhard nanocomposite $Ti_{1-x}Al_xN$ films prepared by magnetron sputtering", *Thin Solid Films*, vol. 365, no. 1, pp. 104–109, 2000.

[69] J. Nagamatsu, N. Nakagawa, T. Muranaka, Y. Zenitani, and J. Akimitsu, "Superconductivity at 39 K in magnesium diboride", *nature*, vol. 410, no. 6824, pp. 63–64, 2001.

[70] R. Telle, L. S Sigl, and K. Takagi, "Boride-based hard materials", *Handbook of ceramic hard materials*, pp. 802–945, 2000.

[71] T. Lundström, "Transition metal borides", in *Boron and refractory borides*, Springer, 1977, pp. 351–376.

[72] B. P. Fokwa, "Borides: Solid-State Chemistry", *Encyclopedia of Inorganic and Bioinorganic chemistry*, pp. 1–14, 2011.

[73] V. Moraes, H. Riedl, C. Fuger, *et al.*, "Ab initio inspired design of ternary boride thin films", *Scientific reports*, vol. 8, no. 1, pp. 1–9, 2018.

[74] G. V. Samsonov, I. F. Pryadko, and L. F. Pryadko, *A configurational model of matter*. Springer Science & Business Media, 1973.

[75] L. F. Pryadko and I. F. Pryadko, "Configuration model of matter and the problem of the valence factor in the theory of the construction of d-, f-electronic systems", *Powder metallurgy and metal ceramics*, vol. 37, no. 1-2, pp. 15–25, 1998.

[76] G. V. Samsonov, B. A. Kovenskaya, and T. I. Serebryakova, "Some physical characteristics of the diborides of transition metals of groups IV and V", *Soviet Physics Journal*, vol. 14, no. 1, pp. 11–14, 1971.

[77] G. V Samsonov, I. F Pryadko, V. V Ogorodnikov, L. F Pryadko, *et al.*, "Statistical weights of stable configurations of localized valence electrons in d transition metals", *Soviet Physics Journal*, vol. 13, no. 5, pp. 645–647, 1970.

[78] G. V Samsonov and B. A Kovenskaya, "The electronic structure of boron compounds", in *Boron and Refractory Borides*, Springer, 1977, pp. 5–18.

[79] W. Martienssen and H. Warlimont, *Springer handbook of condensed matter and materials data*. Springer Science & Business Media, 2006.

[80] P. Wang, R. Kumar, E. M. Sankaran, *et al.*, "Vanadium diboride (VB_2) synthesized at high pressure: Elastic, mechanical, electronic, and magnetic properties and thermal stability", *Inorganic chemistry*, vol. 57, no. 3, pp. 1096–1105, 2018.

[81] S. Otani, M. M. Korsukova, and T. Mitsuhashi, "Floating zone growth and high-temperature hardness of NbB_2 and TaB_2 single crystals", *Journal of crystal growth*, vol. 194, no. 3-4, pp. 430–433, 1998.

[82] J. J. Gilman, *Chemistry and physics of mechanical hardness*. Wiley Online Library, 2009, vol. 5.

[83] G. Kysla and P. Loboda, "Ceramic materials of the quasi-binary LaB_6-MoB_2 system", *Processing and Application of Ceramics*, vol. 1, no. 1-2, pp. 19–22, 2007.

[84] S. Yin, D. He, C. Xu, *et al.*, "Hardness and elastic moduli of high pressure synthesized MoB_2 and WB_2 compacts", *High Pressure Research*, vol. 33, no. 2, pp. 409–417, 2013.

[85] S. Okada, K. Kudou, and T. Lundström, "Preparations and some properties of W_2B, δ-WB and WB_2 crystals from high-temperature metal solutions", *Japanese journal of applied physics*, vol. 34, no. 1R, p. 226, 1995.

[86] A. H. Shaw, "Physical properties of various conductive diborides and their binaries", 2015.

[87] C. Wang, L. Song, and Y. Xie, "Mechanical and electrical characteristics of WB_2 synthesized at high pressure and high temperature", *Materials*, vol. 13, no. 5, p. 1212, 2020.

[88] L. Makarovskii, "Phase diagram of the Mn-B system", *Izv. Akad. Nauk SSSR. Neorg. Mat*, vol. 3, p. 2165, 1967.

[89] A. Cely, L.-E. Tergenius, and T. Lundstrom, "Microhardness measurements and phase analytical studies in the Mn-B system", *Journal of the Less Common Metals*, vol. 61, no. 2, pp. 193–198, 1978.

[90] S. Aydin and M. Simsek, "First-principles calculations of MnB_2, TcB_2, and ReB_2 within the ReB_2-type structure", *Physical Review B*, vol. 80, no. 13, p. 134 107, 2009.

[91] M. Kasaya and T. Hihara, "Magnetic structure of MnB_2", *Journal of the Physical Society of Japan*, vol. 29, no. 2, pp. 336–342, 1970.

[92] H.-Y. Chung, M. B. Weinberger, J. B. Levine, *et al.*, "Synthesis of ultra-incompressible superhard rhenium diboride at ambient pressure", *Science*, vol. 316, no. 5823, pp. 436–439, 2007.

[93] G. V Samsonov and B. A Kovenskaya, "The nature of the chemical bond in borides", in *Boron and Refractory Borides*, Springer, 1977, pp. 19–30.

[94] C. Fuger, V. Moraes, R. Hahn, *et al.*, "Influence of tantalum on phase stability and mechanical properties of WB_2", *MRS Communications*, vol. 9, no. 1, pp. 375–380, 2019.

[95] V. Moraes, C. Fuger, V. Paneta, *et al.*, "Substoichiometry and tantalum dependent thermal stability of α-structured W-Ta-B thin films", *Scripta Materialia*, vol. 155, pp. 5–10, 2018.

[96] H. Euchner, P. H Mayrhofer, H. Riedl, *et al.*, "Solid solution hardening of vacancy stabilized $Ti_xW_{1-x}B_2$", *Acta Materialia*, vol. 101, pp. 55–61, 2015.

[97] F. Heusler, "Über magnetische manganlegierungen", *Verhandlungen der Deutschen Physikalischen Gesellschaft*, vol. 5, p. 219, 1903.

[98] P. J. Webster, "Heusler alloys", *Contemporary Physics*, vol. 10, no. 6, pp. 559–577, 1969.

[99] R. W. Overholser, "Chemical ordering in Ni-Mn-Ga heusler alloys.", 1998.

[100] S. P Venkateswaran, N. T Nuhfer, and M. De Graef, "Anti-phase boundaries and magnetic domain structures in Ni_2MnGa-type Heusler alloys", *Acta Materialia*, vol. 55, no. 8, pp. 2621–2636, 2007.

[101] O. Heczko, N. Scheerbaum, and O. Gutfleisch, "Magnetic shape memory phenomena", in *Nanoscale magnetic materials and applications*, Springer, 2009, pp. 399–439.

[102] P. J Webster, K. R. A Ziebeck, S. L Town, and M. S Peak, "Magnetic order and phase transformation in Ni_2MnGa", *Philosophical Magazine B*, vol. 49, no. 3, pp. 295–310, 1984.

[103] P. J Brown, A. Y. Bargawi, J. Crangle, K.-U. Neumann, and K. R. A Ziebeck, "Direct observation of a band Jahn-Teller effect in the martensitic phase transition of Ni_2MnGa", *Journal of Physics: Condensed Matter*, vol. 11, no. 24, p. 4715, 1999.

[104] V. V Khovailo, V. Novosad, T. Takagi, D. A Filippov, R. Z Levitin, and A. N Vasilev, "Magnetic properties and magnetostructural phase transitions in $Ni_{2+x}Mn_{1-x}Ga$ shape memory alloys", *Physical Review B*, vol. 70, no. 17, p. 174 413, 2004.

[105] V. N Antonov, L. V Bekenov, S. Uba, A. Bonda, and L. Uba, "Electronic structure and X-ray magnetic circular dichroism in the Ni-Mn-Ga Heusler alloys", *Journal of Alloys and Compounds*, vol. 695, pp. 1826–1837, 2017.

[106] K. Ooiwa, K. Endo, and A. Shinogi, "A structural phase transition and magnetic properties in a Heusler alloy Ni_2MnGa", *Journal of Magnetism and Magnetic Materials*, vol. 104, pp. 2011–2012, 1992.

[107] W. H Wang, F. X Hu, J. L Chen, *et al.*, "Magnetic properties and structural phase transformations of NiMnGa alloys", *IEEE transactions on magnetics*, vol. 37, no. 4, pp. 2715–2717, 2001.

[108] J. Enkovaara, O. Heczko, A. Ayuela, and R. M. Nieminen, "Coexistence of ferromagnetic and antiferromagnetic order in Mn-doped Ni_2MnGa", *Physical Review B*, vol. 67, no. 21, p. 212 405, 2003.

[109] J. Kübler, A. R William, and C. B Sommers, "Formation and coupling of magnetic moments in Heusler alloys", *Physical Review B*, vol. 28, no. 4, p. 1745, 1983.

[110] B. Himmetoglu, V. M. Katukuri, and M. Cococcioni, "Origin of magnetic interactions and their influence on the structural properties of Ni_2MnGa and related compounds", *Journal of Physics: Condensed Matter*, vol. 24, no. 18, p. 185 501, 2012.

[111] M. Zelený, L. Straka, A. Sozinov, and O. Heczko, "Ab initio prediction of stable nanotwin double layers and 4O structure in Ni_2MnGa", *Physical Review B*, vol. 94, no. 22, p. 224 108, 2016.

[112] V. V Martynov and V. V Kokorin, "The crystal structure of thermally-and stress-induced martensites in Ni_2MnGa single crystals", *Journal de Physique III*, vol. 2, no. 5, pp. 739–749, 1992.

[113] J. Pons, V. A Chernenko, R. Santamarta, and E. Cesari, "Crystal structure of martensitic phases in Ni–Mn–Ga shape memory alloys", *Acta Materialia*, vol. 48, no. 12, pp. 3027–3038, 2000.

[114] S. Singh, J. Bednarcik, S. R Barman, C. Felser, and D. Pandey, "Premartensite to martensite transition and its implications for the origin of modulation in Ni_2MnGa ferromagnetic shape-memory alloy", *Physical Review B*, vol. 92, no. 5, p. 054 112, 2015.

[115] S. Fujii, S. Ishida, and S. Asano, "Electronic structure and lattice transformation in Ni_2MnGa and Co_2NbSn", *Journal of the Physical Society of Japan*, vol. 58, no. 10, pp. 3657–3665, 1989.

[116] L. Manosa, A. Planes, J Zarestky, T Lograsso, D. L. Schlagel, and C Stassis, "Phonon softening in Ni-Mn-Ga alloys", *Physical Review B*, vol. 64, no. 2, p. 024 305, 2001.

[117] C. Bungaro, K. Rabe, and A. Dal Corso, "First-principles study of lattice instabilities in ferromagnetic Ni_2MnGa", *Physical Review B*, vol. 68, no. 13, p. 134 104, 2003.

[118] A. Zheludev, S. M Shapiro, P. Wochner, A. Schwartz, M. Wall, and L. E Tanner, "Phonon anomaly, central peak, and microstructures in Ni_2MnGa", *Physical Review B*, vol. 51, no. 17, p. 11 310, 1995.

[119] T. D Haynes, R. J Watts, J. Laverock, *et al.*, "Positron annihilation study of the Fermi surface of Ni_2MnGa", *New Journal of Physics*, vol. 14, no. 3, p. 035 020, 2012.

[120] M. Siewert, M. E Gruner, A. Dannenberg, *et al.*, "Electronic structure and lattice dynamics of the magnetic shape-memory alloy Co_2NiGa", *Physical Review B*, vol. 82, no. 6, p. 064 420, 2010.

[121] K. Ullakko, "Magnetically controlled shape memory alloys: A new class of actuator materials", *Journal of materials Engineering and Performance*, vol. 5, no. 3, pp. 405–409, 1996.

[122] S. J. Murray, M. Marioni, S. M Allen, R. C Ohandley, and T. A. Lograsso, "6% magnetic-field-induced strain by twin-boundary motion in ferromagnetic Ni–Mn–Ga", *Applied Physics Letters*, vol. 77, no. 6, pp. 886–888, 2000.

[123] A. Sozinov, A. A Likhachev, N. Lanska, and K. Ullakko, "Giant magnetic-field-induced strain in NiMnGa seven-layered martensitic phase", *Applied Physics Letters*, vol. 80, no. 10, pp. 1746–1748, 2002.

[124] A. Dannenberg, "Ab initio and Monte Carlo investigations of structural, electronic and magnetic properties of new ferromagnetic Heusler alloys with high Curie temperatures", *University of Duisburg-Essen*, 2011.

[125] J. Liu, T. Gottschall, K. P. Skokov, J. D. Moore, and O. Gutfleisch, "Giant magnetocaloric effect driven by structural transitions", *Nature materials*, vol. 11, no. 7, pp. 620–626, 2012.

[126] A. Sozinov, N. Lanska, A. Soroka, and W. Zou, "12% magnetic field-induced strain in Ni-Mn-Ga-based non-modulated martensite", *Applied Physics Letters*, vol. 102, no. 2, p. 021 902, 2013.

[127] T. Kanomata, K. Endo, N. Kudo, *et al.*, "Magnetic moment of Cu-modified Ni_2MnGa magnetic shape memory alloys", *Metals*, vol. 3, no. 1, pp. 114–122, 2013.

[128] T. Koubský, P Sedlák, H Seiner, *et al.*, "Ab initio study of martensitic transition in Ni_2MnGa", *Acta Phys. Pol. A*, vol. 134, no. 804, p. 2019, 2018.

[129] L. Bodnárová, M. Zelený, P. Sedlák, *et al.*, "Switching the soft shearing mode orientation in Ni–Mn–Ga non-modulated martensite by Co and Cu doping", *Smart Materials and Structures*, vol. 29, no. 4, p. 045 022, 2020.

[130] M. Zelený, L. Straka, M. Rameš, A. Sozinov, and O. Heczko, "Origin of magnetocrystalline anisotropy in Ni-Mn-Ga-Co-Cu tetragonal martensite", *Journal of Magnetism and Magnetic Materials*, vol. 503, p. 166 522, 2020.

[131] G. Kresse and J. Furthmüller, "Efficiency of ab-initio total energy calculations for metals and semiconductors using a plane-wave basis set", *Computational materials science*, vol. 6, no. 1, pp. 15–50, 1996.

[132] G. Kresse and D. Joubert, "From ultrasoft pseudopotentials to the projector augmented-wave method", *Physical review b*, vol. 59, no. 3, p. 1758, 1999.

[133] X. Zhang, X. Luo, J. Han, J. Li, and W. Han, "Electronic structure, elasticity and hardness of diborides of zirconium and hafnium: First principles calculations", *Computational materials science*, vol. 44, no. 2, pp. 411–421, 2008.

[134] X. L Chen, Q. Y Tu, M. He, L. Dai, and L. Wu, "The bond ionicity of MB_2 (M= Mg, Ti, V, Cr, Mn, Zr, Hf, Ta, Al and Y)", *Journal of Physics: Condensed Matter*, vol. 13, no. 29, p. L723, 2001.

[135] E. Canadell, M.-L. Doublet, and I. Christophe, *Orbital Approach to the Electronic Structure of Solids*. Jan. 2012, ISBN: 9780199534937.

[136] A. Ayuela, J. Enkovaara, K. Ullakko, and R. M Nieminen, "Structural properties of magnetic Heusler alloys", *Journal of Physics: Condensed Matter*, vol. 11, no. 8, p. 2017, 1999.

List of abbreviations

DFT	Density functional theory
TMD	Transition metal diboride
TM	Transition metal
DOS	Density of states
COHP	Crystal Orbital Hamiltonian Population
COOP	Crystal Orbital Overlap Population
LOBSTER	Local-Orbital Basis Suite Towards Electronic-Structure Reconstruction
MFIS	Magnetic field-induced strain
MSM	Magnetic shape memory
LDA	Local density approximation
GGA	Generalized gradient approximation
$\hbar$	Reduced Planck's constant
$\hat{H}$	Hamiltonian
$\Psi(\boldsymbol{x},t)$	Time-dependent wave function
$\psi(\boldsymbol{x})$	Time-independent wave function
m_e	Electron mass
M_I	Nucleus mass
∇^2	Laplace operator
e	Elemental charge
ε_0	Dielectric constant of vacuum
B-O	Born-Oppenheimer approximation
LCAO	Linear combination of atomic orbitals
HF	Hartree-Fock method
ρ, $n(\boldsymbol{r})$	Electron density
KS	Kohn-Sham ansatz
LDA	Local density approximation
GGA	Generalized-gradient approximation
DFT+ U	Hubbard correction to density functional theory
PAW	Projector augmented wave
DOE	Density of energy

DFT	Density functional theory
HV	Vickers hardness
FCC	Face-centered cubic lattice
CVD	Chemical vapor deposition
PVD	Physical vapor deposition
T_c	Critical temperature for superconductors
T_m	Melting temperature
SWASC	Statistical weight of atom with stable configuration
T_C	Curie temperature
RKKY	Ruderman-Kittel-Kasuya-Yosida theory
T_M	Temperature of martensitic transformation
NM	Non-modulated tetragonal martensite
c/a	Tetragonality
10M, 5M	Five-layered modulated martensite
14M, 7M	Seven-layered modulated martensite
4O	Orthorombic four-layered modulated martensite
T_PM	Temperature of premartensitic transformation
3M	Three-layered modulated Premartensite
VASP	Vienna Ab-initio Simulation Package
ε_f, E_F	Fermi level
LDOS	Local density of states
PDOS	Projected density of states

Appendices

Appendix A

DOS, COHP, COOP and DOE analysis of all studied transition metal diborides. Integrated DOE up to the Fermi level (band energy) is compared with integrated COHP (contribution of inter-atomic interactions shorter than 5 Å to the band energy).

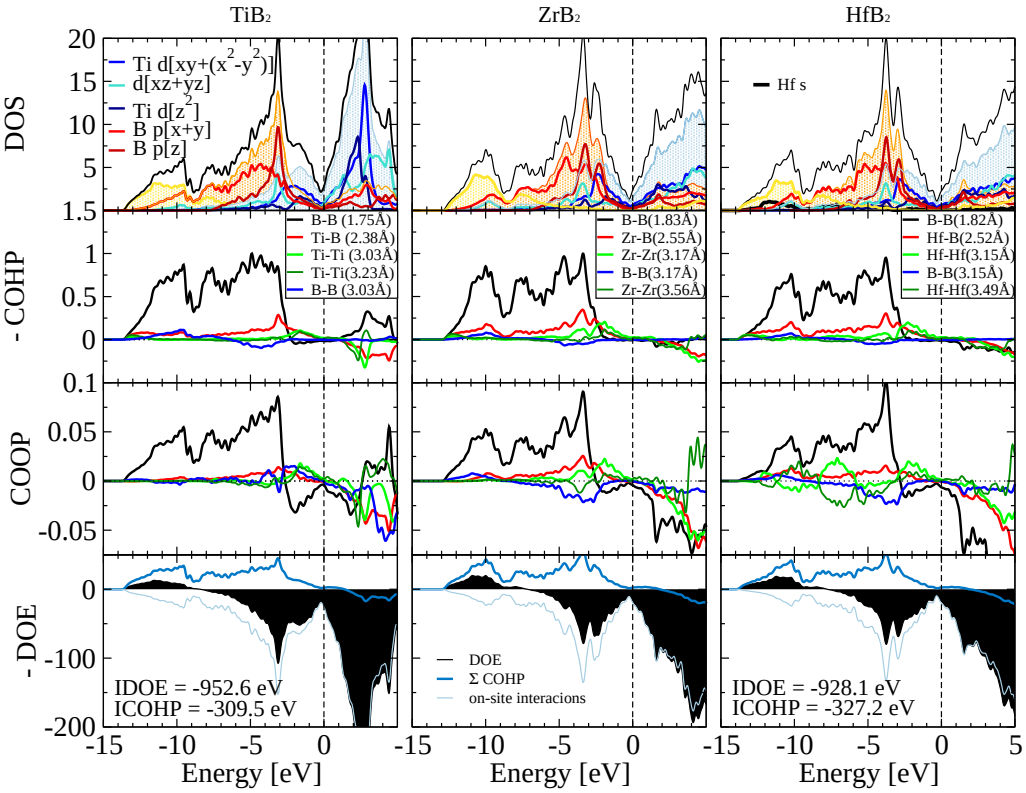

Figure 26: Group 4 transition metal diborides. ZrB_2 was calculated without semi-core Zr *p* electrons therefore IDOE and ICOHP are not stated (COHP and DOE is basis dependent).

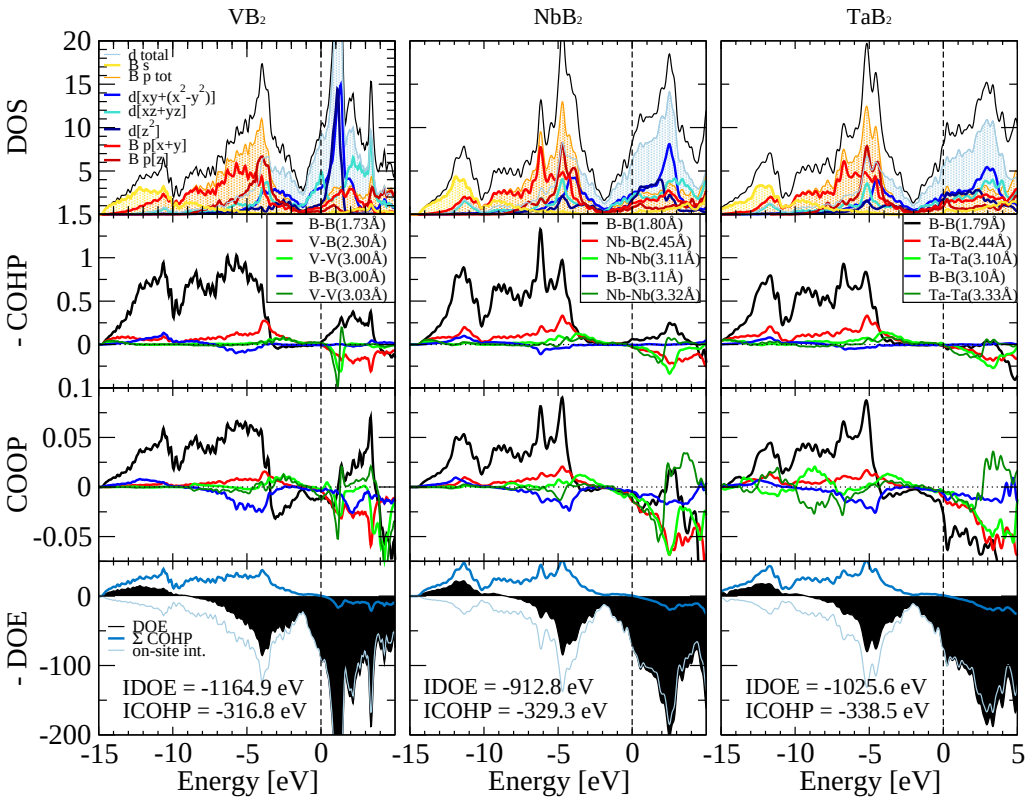

Figure 27: Group 5 transition metal diborides.

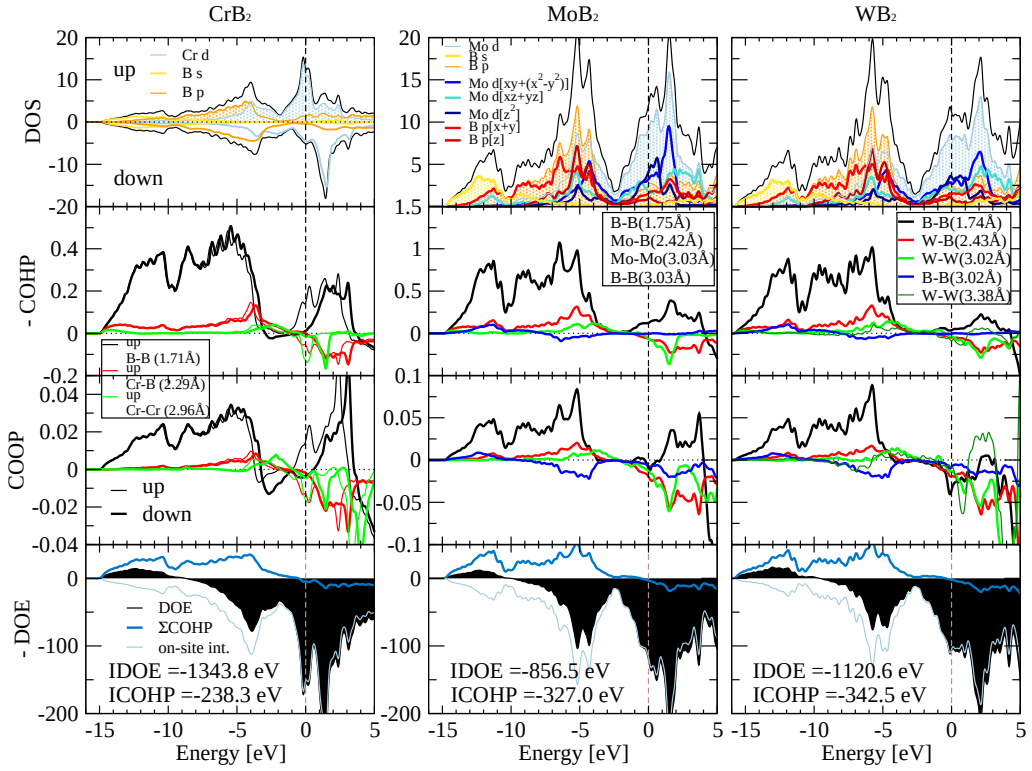

Figure 28: Group 6 transition metal diborides.

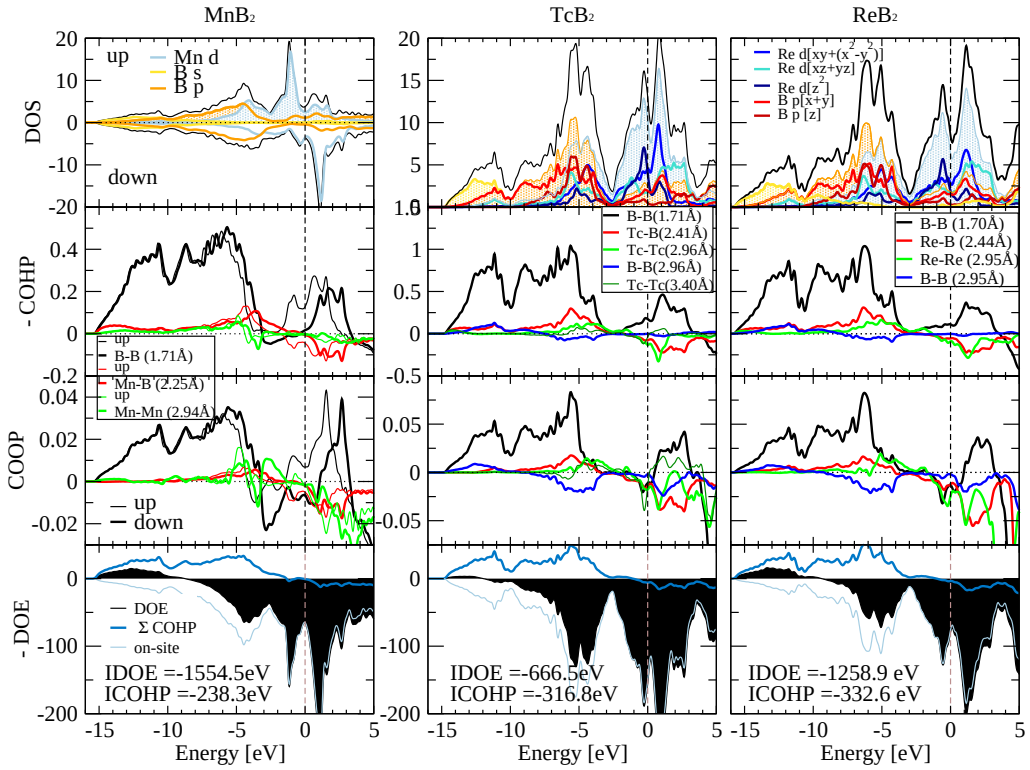

Figure 29: Group 7 transition metal diborides.

Appendix B

COHP comparison of four shortest bonds in Ni_2MnGa, calculated with GGA and DFT+ U with U = 3 eV on different atoms.

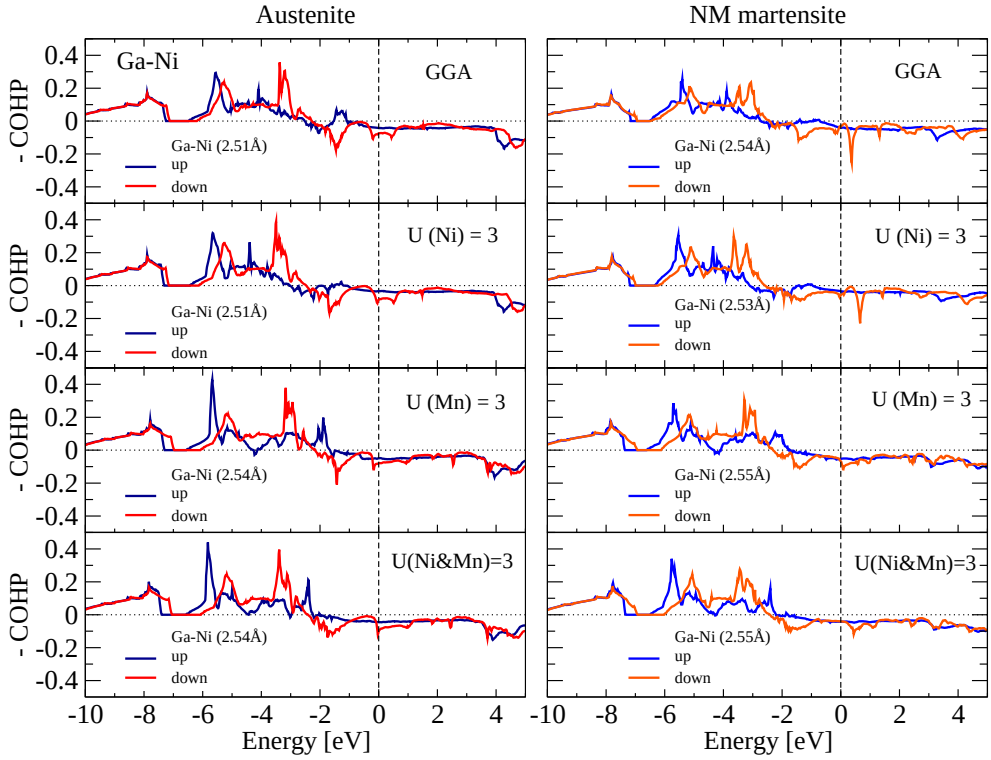

Figure 30: COHP analysis of Ga-Ni interaction, comparison of different U applications.

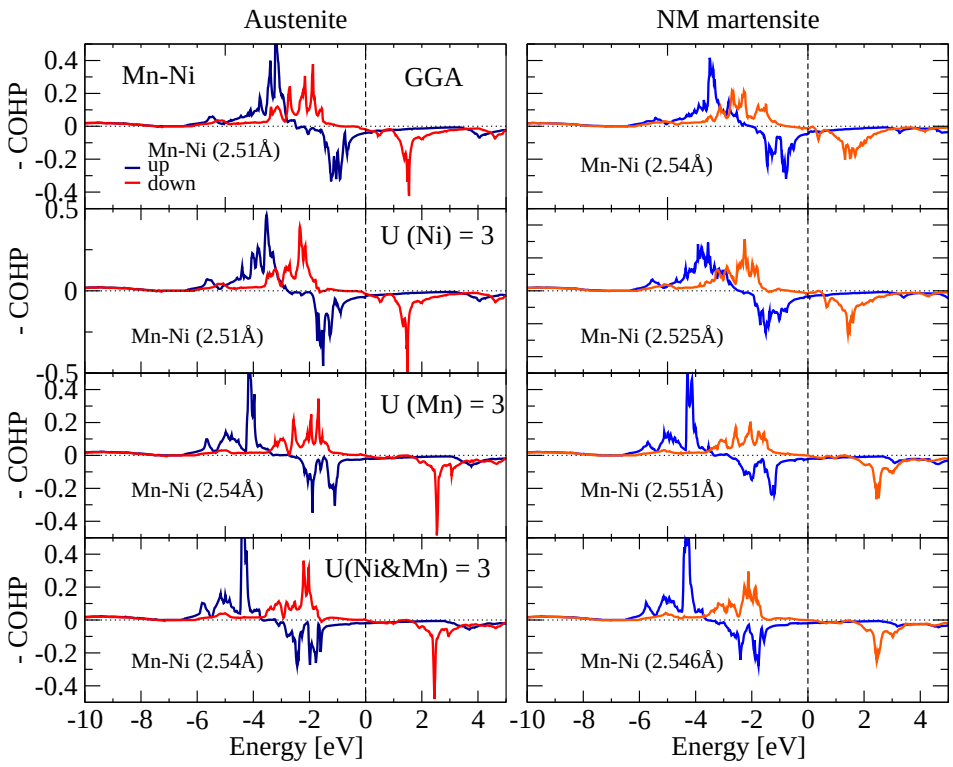

Figure 31: COHP analysis of Mn-Ni interaction, comparison of different U applications.

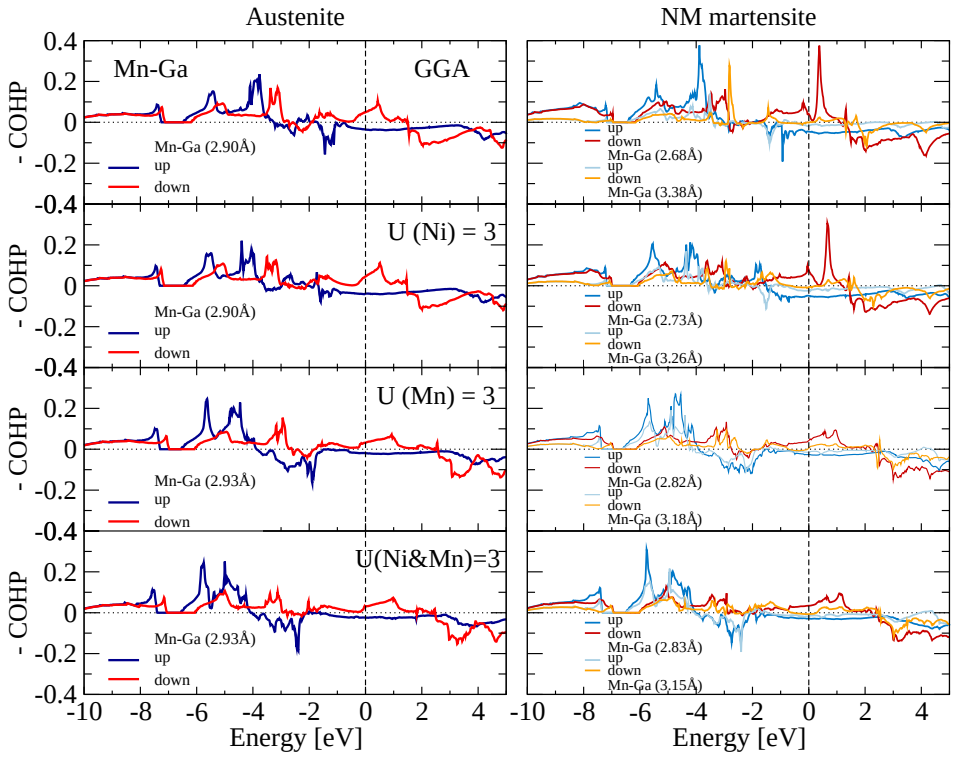

Figure 32: COHP analysis of Mn-Ga interaction, comparison of different U applications.

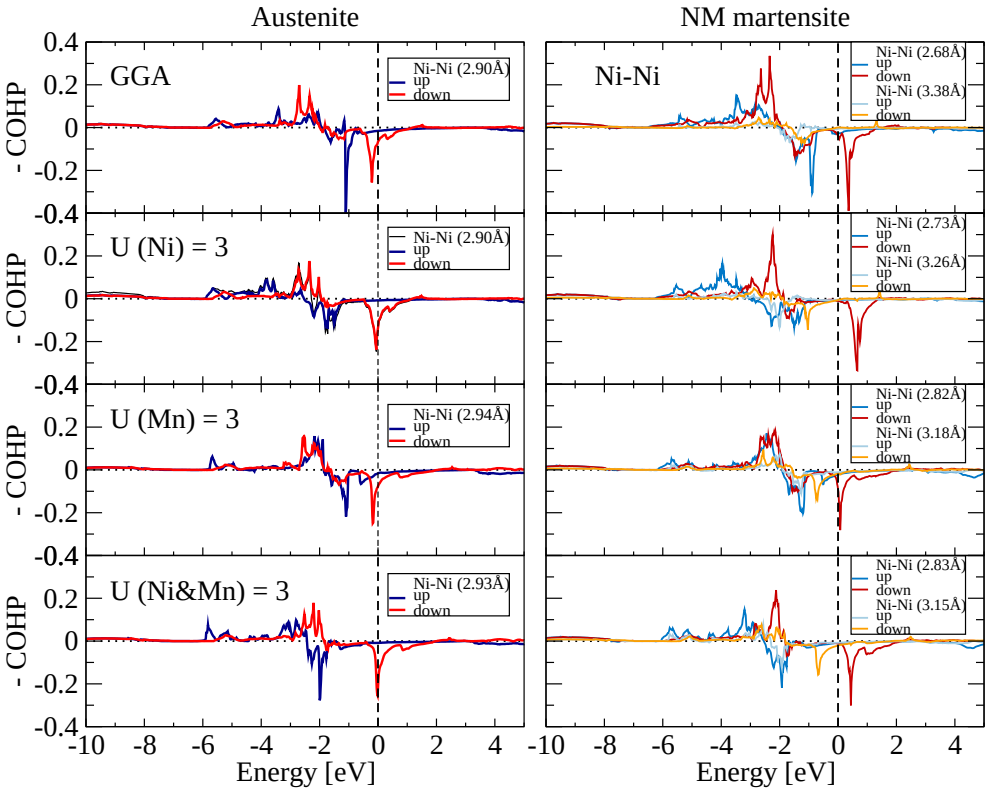

Figure 33: COHP analysis of Ni-Ni interaction, comparison of different U applications.

Appendix C

Charge density difference map, comparison between GGA and DFT+ U with U = 3 eV on Ni and Mn.

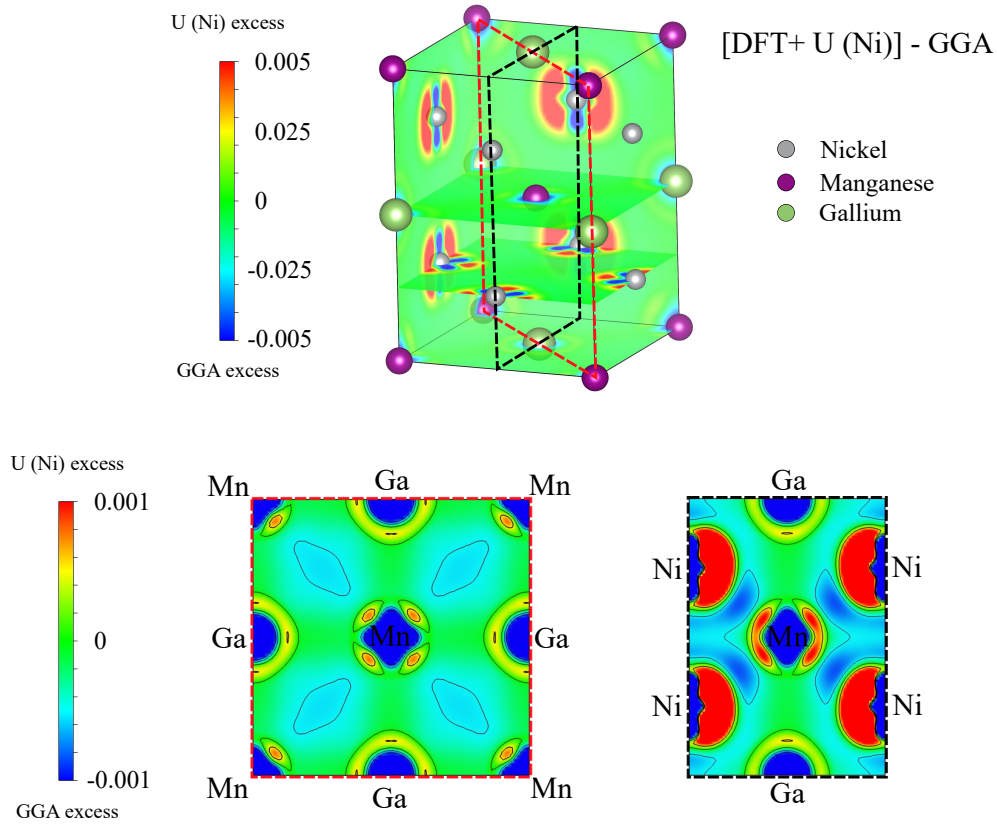

Figure 34: Charge difference between GGA and DFT+ U with U = 3 eV on Ni.

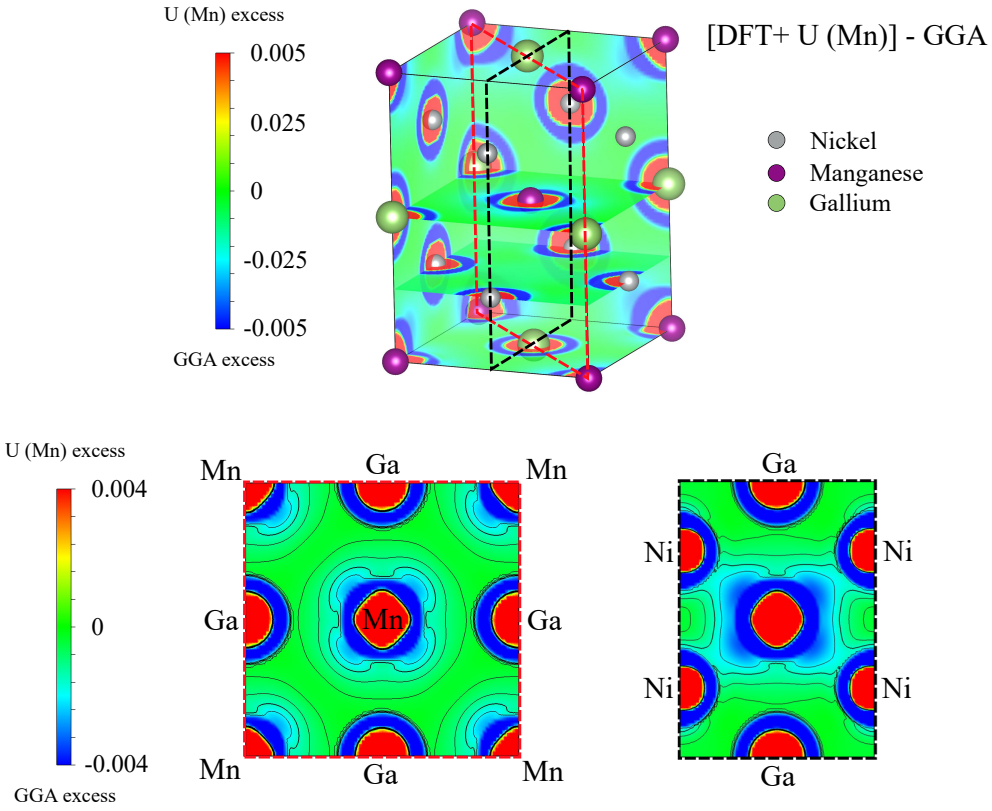

Figure 35: Charge difference between GGA and DFT+ U with U = 3 eV on Mn.